Sensitivity of the Lambert-Amery Glacial System to ice sheet model boundary conditions

Doreen Melari Warjri

BSc, MSc

Submitted in fulfilment of the requirements
for the Degree of Doctor of Philosophy

Geography and Spatial Sciences
Institute for Marine and Antarctic Studies
University of Tasmania

May, 2021

UNIVERSITY of TASMANIA

IMAS
INSTITUTE FOR MARINE
& ANTARCTIC STUDIES

I declare that this thesis contains no material which has been accepted for a degree or diploma by the University or any other institution, except by way of background information and duly acknowledged in the thesis, and that, to the best of my knowledge and belief, this thesis contains no material previously published or written by another person, except where due acknowledgement is made in the text of the thesis, nor does the thesis contain any material that infringes copyright.

Signed: ______________________________

Doreen Melari Warjri

Date: 23 December 2020

Signed: ______________________________

Doreen Melari Warjri

Date: 23 December 2020

Abstract

The Lambert-Amery Glacial System (LAGS) is a major drainage basin in East Antarctica, and is one of the largest glacial systems on Earth with a total area of $\sim$ 60,000 km^2. The three largest glaciers within the system, the Lambert, Mellor and Fisher Glaciers, feed the Amery Ice Shelf (AIS). The AIS provides stability to the LAGS and contains some of the deepest ice in contact with the ocean in Antarctica at $\sim$ 2500 m below sea level. The LAGS drains ice from far inland East Antarctica, and hence incremental changes in either ice shelf geometry or ocean temperature can impact significantly on the whole system. The dynamic response of the AIS to present day boundary perturbations or physical processes is not fully understood due to limited data availability for this difficult to access region. Exploration of the factors that control the dynamics of the AIS, in particular those that are captured by ice sheet models as boundary conditions, is therefore required to progress understanding of the probable future contribution of the LAGS to sea-level rise.

The LAGS is a stable system over multi-decadal timescales, and therefore provides an opportunity for modelling studies, compared with observations, for the investigation of ice sheet model boundary conditions. In this thesis, model-based studies are undertaken to examine the impact of the choice of different bathymetries, ice shelf retreat scenarios, and basal melt models on the simulated ice dynamics of the AIS. The Parallel Ice Sheet Model (PISM, Version 0.7.3) was used for these numerical experiments: a three dimensional, thermomechanically-coupled hybrid model that superposes the shallow ice approximation and the shallow shelf approximation. Model resolution and workflows were chosen to carry out the aforementioned studies within the limitations of available computing resources.

The geometry of the bedrock beneath a glacier system and its outlet ice shelf is understood to have a significant control on the evolution of that system. However, the depth of the bedrock in most locations under the AIS is not well-known. Tests of the sensitivity to bedrock geometry were carried out using PISM. The model was run using four bathymetry test cases, including one case with the addition of pinning points at the ice front that have previously been inferred from remote sensing data. It was found that the choice of bathymetry substantially impacts the modelled ice velocity across the grounding line, the ice velocity of the ice shelf, and the calving front position. The dynamic response to changes in the geometry of the bathymetry and pinning points that interact with the ice shelf base, even of small-scale, demonstrates the importance of high accuracy bathymetry data. A consequence of these findings is that under-

sampled bathymetry can lead to undue emphasis on poorly constrained modelling parameters to reproduce the ice shelf extent. These findings also highlight the complex feedback between ice dynamics and AIS bathymetry, and hence the importance of bathymetry in future modelling of the LAGS.

The AIS provides stability to the LAGS due to the effect of buttressing. If the calving front were to retreat from its present day geometry, the reduction in buttressing could cause acceleration of the calving front, and potentially impact ice dynamics at the deep grounding line. To quantify how a retreated ice shelf geometry impacts the stability of the AIS, different scenarios of retreat, including extreme retreat geometries, were imposed. Each scenario was set by following a threshold value in the along-flow strain rate, removing progressively more ice from the ice shelf front. Previously hypothesised criteria for ice shelf stability were explored for each retreat scenario based on the 2$^{\text{nd}}$ principal strain rate (the "compressive arch" hypothesis), and the angle between the 1$^{\text{st}}$ principal stress direction and the ice flow direction. Further experiments that explored calving laws were also carried out. The results of these individual investigations differed in detail, highlighting shortcomings in the current understanding of the dynamics of ice shelves, and indicating that additional exploration of stability criteria and calving laws is needed when identifying tipping points in ice shelf retreat. Taken together, the model results suggest that the AIS is stable until it retreats approximately up to 85 km upstream of the current calving front. Some sections of the ice shelf did not cause a speed-up of the ice flow at the calving front when further ice was removed. This area of passive ice on the AIS is larger than in previous studies, and this may be due to the inclusion of small-scale pinning points near the calving front which were included in the the above bathymetry study, but previously neglected. At some retreat positions, the models of the AIS show significant increase in velocity, which can propagate to the deep grounding line in the case of a calving front in the south of the AIS where the ice shelf embayment narrows.

The basal melt rate of an ice sheet is influenced by ocean temperature, salinity and pressure, and since the deepest parts of the LAGS grounding line are up to $\sim$ 2500 m below sea level, intrusion of Circumpolar Deep Water along with hydrostatic pressure generates large basal melt rates in the southern AIS grounding zone. An increase in melt rates for the AIS, potentially caused by an increase in ocean temperature, could drive retreat of the deep grounded ice and global sea level contribution from the LAGS. To understand the effect of different basal melt rate estimates on the evolution of the AIS, a range of ice-ocean interface model parameter inputs were investigated. The model of the AIS responded differently to these ice-ocean input parameter choices, and from a simple experiment it was clear that the internal basal melt models (PISM V. 0.7.3) could not reproduce the observed spatial pattern of melting and refreezing. Improvement, however, can be made by supplying PISM with a three-dimensional regional ocean model that incorporates spatial variation including the influence on ocean temperature of frazil ice precipitation and refreezing. This resulted in a realistic level of basal melt at the deep grounding line in the southern part of the AIS, and replicated the observed pattern of basal refreezing on the western side of the ice shelf. Basal melt at the grounding line and the pattern of refreezing influence ice dynamics, and cause the calving front to advance significantly compared to other ice-ocean interface model inputs. This result implies that studies that do not incorporate the needed boundary conditions from ocean models could over-estimate the future sea level contribution from the AIS as refreezing supports buttressing and provides stability to the calving front.

The experiments carried out throughout this thesis show the importance to ice sheet modelling of comparing multiple input data sets that provide boundary conditions, and also assessment criteria and model choices to identify the possible causes of discrepancies between modelled results and observations. In summary, the findings demonstrate model sensitivity to small-scale bedrock features, and ice-ocean input data, for modelling ice dynamics. In further research involving modelling of the AIS, the LAGS, and other systems over long time-scales, the bathymetry study indicates that a change in ice shelf cavity shape would impact the ice sheet evolution, and therefore points to the need for coupled ice-ocean modelling. Our findings also point to the influence of small-scale bedrock features on the likely calving response of the ice shelf under different retreat scenarios. As a result of the research described in this thesis, it is recommended that efforts continue to improve bathymetry datasets, particularly in the regions upstream of present day calving fronts, and that ocean models are considered as input to studies using PISM, rather than relying on internal parameter selections. Incorporating these improvements should enable future modelling studies to better predict the response of ice sheet systems such as the LAGS to external forcings, and thus improve estimates of future ice mass loss and consequent contributions to sea-level rise.

Acknowledgements

My thanks are due to many people: Matt King for posing challenging questions and his support as supervisor throughout, Sue Cook for being an amazing co-supervisor especially with regard to advice on modelling and interpretation discussions, Rupert Gladstone for modelling discussions, Anya Reading for assistance with scientific writing, Steven Phipps and Ben Galton-Fenzi for their input to early and later stages of the work, and Arko Lucieer for his guidance as Graduate Research Coordinator. Special thanks to John Miezitis for key assistance with high performance computing.

For Anya Reading, Rupert Gladstone and Sue Cook:

"It is the supreme art of the teacher to awaken joy in creative expression and knowledge" - Albert Einstein.

Many thanks also to the many fellow students, postdocs and the IMAS Ice Sheet group for their support during the PhD, and other areas of UTAS for additional seminars and social gatherings.

This research was supported under Australian Research Council's Special Research Initiative for Antarctic Gateway Partnership (Project ID SR140300001). This work was also benefited from the Australian Government's Cooperative Research Centres Program through the Antarctic Climate and Ecosystems Cooperative Research Centre (ACE CRC).

I'd also like to thank my home team: Martin Gal for sharing the journey and filling the evening nights with conversations of physics and philosophy; finally, yet importantly, to Athena the cat for showing me that every day is filled with new adventures.

Contents

List of Figures

List of Tables

Chapter 1

Introduction

This introduction chapter is divided into three parts. The first part summarises the motivation for the research described in this thesis, and outlines the thesis structure. In the second part, a review of literature on the dynamics of the Lambert-Amery Glacial System (LAGS) is presented. The final part of this chapter provides a background to numerical ice sheet modelling, and how it is used to address research questions concerning the physical processes that influence the glacial system.

1.1 Thesis Overview

1.1.1 Motivation for research

Ice sheets are important in the study of climate change as small perturbations in climatic conditions may bring significant changes to ice shelf, glacier and ice sheet stability. Understanding mass loss of glacial ice due to modern climate conditions is crucial for future projections of sea-level rise. The Lambert-Amery Glacial System (LAGS) is composed of glaciers that terminate in the Amery Ice Shelf (AIS) together forming a drainage system which is the largest in East Antarctica (Zwally et al., 2012). From 1968-1999, the AIS experienced no net change in velocity (King et al., 2007) and the rate of elevation change from 1968-2007 was near zero (King et al., 2009). This suggests the LAGS has existed in a relatively stable state for multiple decades (Yu et al., 2010; King et al., 2012) when compared with other ice shelves of Antarctica (Paolo et al., 2015; Gardner et al., 2018, Figure 1.1), which, in turn, makes the AIS and LAGS a good subject for numerical modelling studies.

The aim of this thesis is to investigate the response of the LAGS to geometry, physical processes, and modelling choices using a numerical modelling approach. The outcomes of the research described in this thesis aim to contribute to improving bathymetry constraints for the LAGS, understanding the response of the AIS to potential future calving scenarios, and the role of

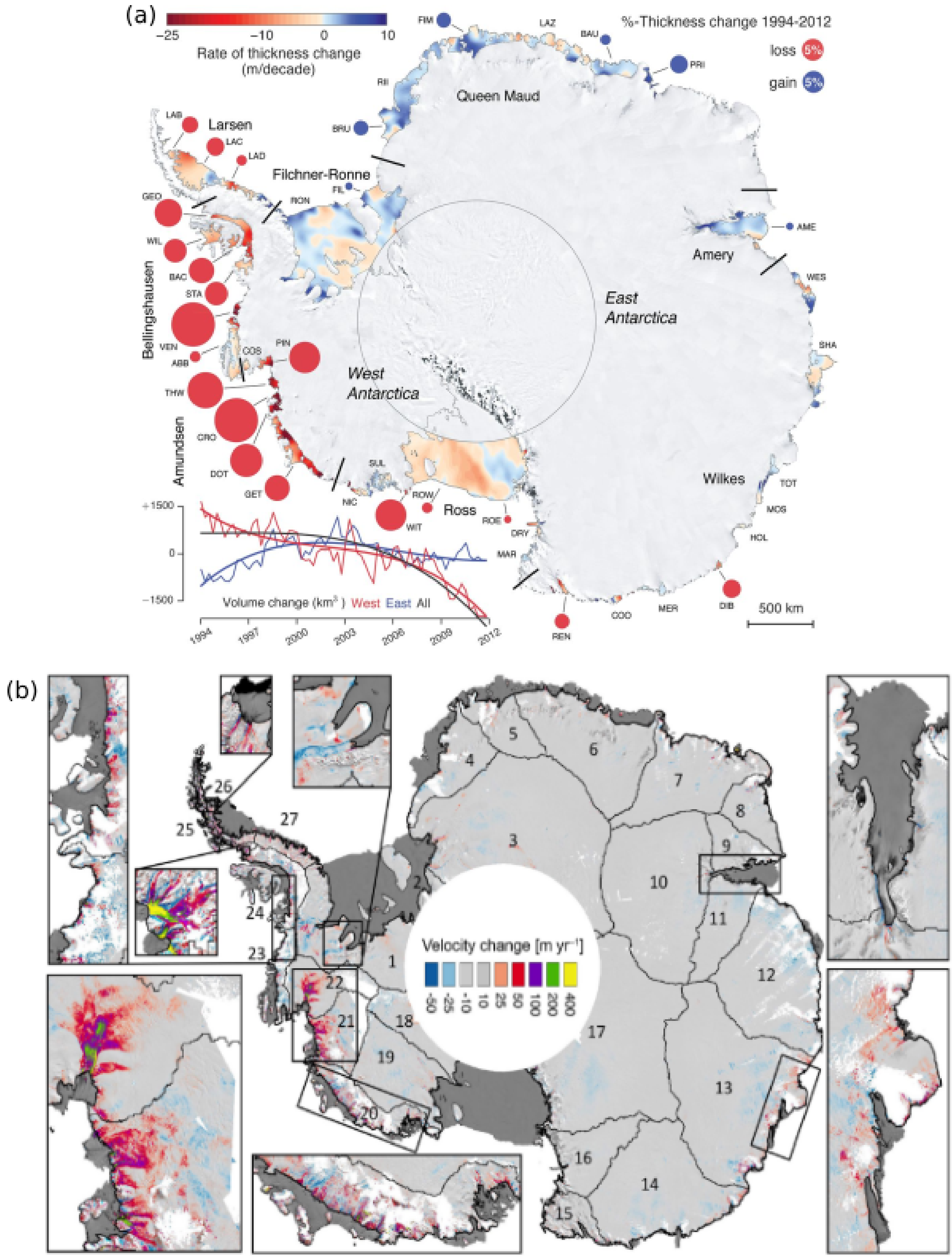

Figure 1.1: (a) Rate of ice thickness change (m per decade) is colour-coded from –25 (thinning) to +10 (thickening), averaged over the period from 1994 to 2012 (figure reproduced from Paolo et al., 2015). (b) Change in surface velocities between date of pan-Antarctic SAR mapping (Rignot et al., 2011) and new 2015 velocity mapping (Gardner et al., 2018).

basal mass flux in the response of the numerical model.

1.1.2 Structure of thesis

The thesis comprises five chapters, including three core chapters focused on glaciological research questions. Core chapters are formatted in the manner of a journal paper (i.e. with some repetition of background material, and use of the first person plural). The core chapters are framed by this introduction and literature review, and a final synthesis of research findings.

Chapter 1 – Introduction

This chapter describes the research motivation and thesis structure and presents a review of background material on the LAGS, and numerical ice sheet modelling approaches. As noted above, the layout of this chapter is in three parts. Following this statement of research motivation and thesis overview, the second part provides an overview of the study area, and the nature and significance of the LAGS. The focus is on its unique yet poorly known geometry, and glacial processes. In the third part of this chapter, the focus is directed towards numerical ice sheet modelling: tools used by the glaciologist to work with the mathematical equations that describe the physics of ice sheet, glaciers and ice shelf, and hence predict its dynamics under given conditions. The models, to be run using the Parallel Ice Sheet Model 'PISM' will approximate the real system, providing a means of investigating the significance of possible controlling parameters. A method is outlined that will be used to obtain a steady state configuration for the model, which deviates as little as possible from the LAGS present day configuration, constrained by observations such as grounding line position, ice shelf extent, ice thickness, and velocity of ice flow. This is a prerequisite state that is used as an initial state for computational experiments described in the three core chapters.

Chapter 2 - Influence of the Bathymetry and Pinning Points on the Lambert-Amery Glacial System Ice Flow

Objective: To explore the impact of different bathymetry geometries and pinning points on modern AIS ice flow towards improved future modelling of the LAGS.

The geometry beneath the AIS is sparsely sampled due to its remote location and the limitations of available surveys, especially in the southern part of the ice shelf. The AIS is the third largest ice shelf in Antarctica and LAGS drains a volume of ice greater than the entire West Antarctic Ice Sheet. This provides motivation to use modelling methods to understand the impact of aspects of the geometry of the bathymetry (subglacial topography) including the presence of pinning points. Here, the modelling framework is used to test the response of the AIS given available Antarctic topography data, and to compare these with modelling given a synthetic topography data set. Model outputs are evaluated against the present day AIS grounding line, ice shelf extent, ice thickness and velocity. This bathymetry study is important for determining boundary conditions that impact the modelled ice shelf dynamics, as a step to better understanding the potential contribution of the LAGS to sea-level rise.

Chapter 3 - Stability of the Amery Ice Shelf to Retreat by Calving

Objective: To investigate the extent of passive ice within the modern Amery Ice Shelf and the calving response of the AIS under different scenarios of retreat.

In this chapter, the calving responses for different retreated ice front positions of the AIS are explored. If the calving front of an ice shelf retreats, there is a potential impact on the support of grounded ice. Reduction of this buttressing potentially causes an increase of outward ice flux of grounded ice to the ocean, a factor that leads to sea-level rise, and impacts on the stability of the remnant ice shelf. Simulated retreated calving fronts derived from the along-flow strain rate are applied in a numerical model to infer the extent of passive ice within the AIS (i.e. ice that does not induce an increased flux of ice towards the ocean if it is removed), and compute how the successive retreat scenarios could affect principal strain rate, strain-flow angles, and calving rates. The probable impacts of these investigations on the shelf stability for the different retreat scenarios is discussed.

Chapter 4 - The Impact of Basal Melt and Refreezing on the Modelling of the Amery Ice Shelf

Objective : To investigate the effect of different ice-ocean interface parameterisations on the computed basal melt and refreezing under the Amery Ice Shelf, and in turn, the effect on ice shelf dynamics.

The basal meltwater production of the AIS is comparable to the much larger ice shelves of West Antarctica, the Ross and the Filchner-Ronne. With its exceptionally deep grounding line, the basal meltwater of the AIS is generated due to ocean temperature and hydrostatic pressure on this deep ice, which impact the mass balance of the LAGS, a crucial factor in understanding the net basal ice loss. Previous studies have been inconsistent in their estimates of basal melt under the AIS. In this chapter a comparison is made between two different ice-ocean interface parameterisations and two further input models for the ice-ocean interface provided by a three-dimensional ocean model. The study investigates the impact of these input model choices on the pattern of basal melt and refreezing, and the resulting modelled grounding line position, ice front position, ice thickness and velocity.

Chapter 5 - Discussion and Conclusions

In this chapter, the main findings of the research are discussed, together with their implications for the contribution of the LAGS to sea-level rise, and recommendations arising from the research. Future directions for research arising from the studies presented herein are noted, and the thesis ends with a summary section that outlines the main conclusions arising from the research.

1.2 Background to Study Area

1.2.1 East Antarctic Ice Sheet

It has long been considered that East Antarctic Ice Sheet (EAIS) is more stable than the West Antarctic Ice Sheet (WAIS) since much of the EAIS area is grounded above sea level. This has led to the concept that the ice loss of the EAIS is mainly due to the rise of air temperature, because it is well protected from ocean heat flux and marine ice sheet instability (MISI) (Weertman, 1974; Thomas and Bentley, 1978; Schoof, 2007). The MISI hypothesis states that any ice sheet with a grounding line that rests on a backsloping bed (i.e. an upward slope towards the ocean) is unstable as increased flux (due to reduced buttressing) leads to the movement of the grounding line into deeper water where the ice is thicker (Pattyn, 2018). Retreat of the grounding line will keep progressing until the grounded ice reaches a bed configuration where it can be stable if conditions do not vary further. More recent improvements in knowledge of the extent of EAIS grounded ice below sea level, and the presence of backsloping beds in the vicinity of the grounding lines of major outlet glaciers, raises an urgent need to investigate the likely response of components of the EAIS. The EAIS could potentially contribute 19 m of global sea-level rise, by the end of the twenty-first century (Church et al., 2013), which is five times more than the marine-based ice sheet of WAIS (Fretwell et al., 2013; Silvano et al., 2016). The melting of ice can occur at the inland or ocean boundary of the ice sheet, with flow of ice through drainage basins in the form of ice streams leading to outlet glaciers, ice shelves, and finally the ocean. The LAGS drains a large region of East Antarctica, with the three largest glaciers within the glacial system being the Lambert, Mellor and Fisher Glaciers.

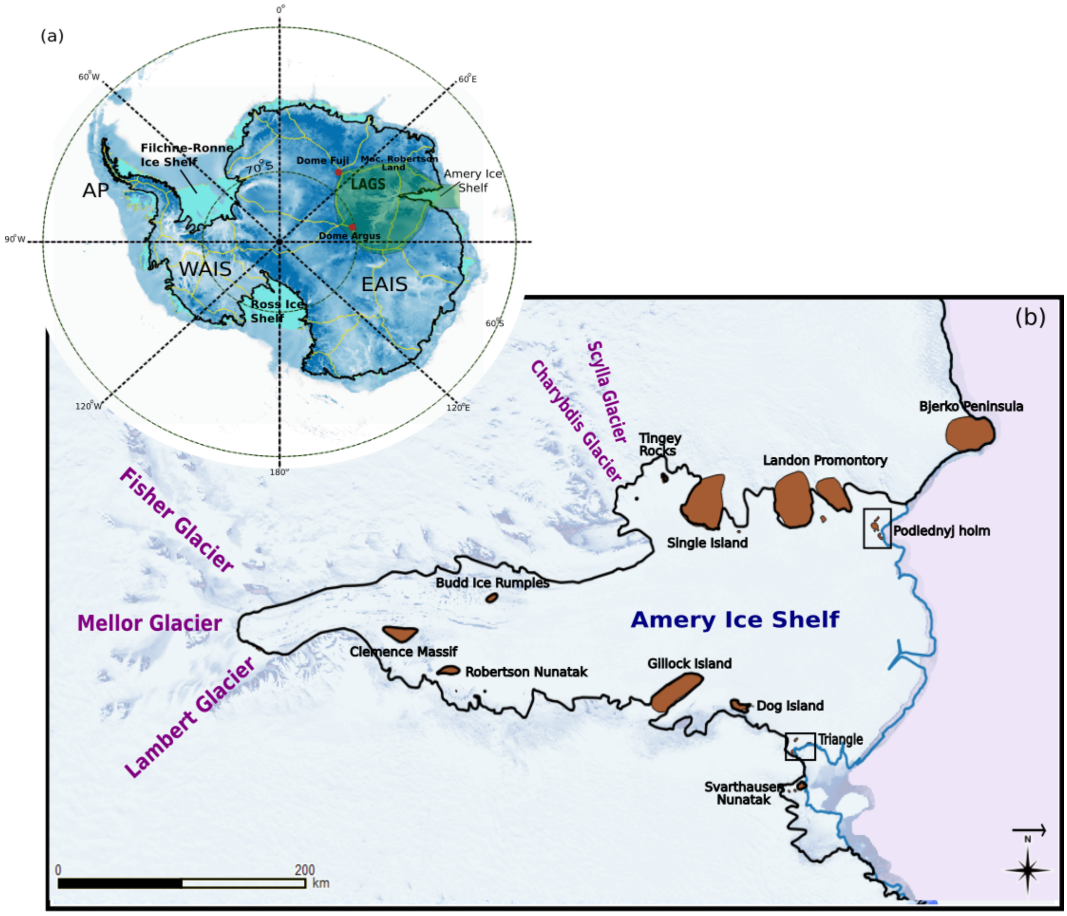

Figure 1.2: (a) Antarctic continent showing East Antarctica Ice Sheet (EAIS), West Antarctica Ice Sheet (WAIS), and Antarctic Peninsula (AP). The Lambert-Amery Glacial System (LAGS; shaded region) feeds the Amery Ice Shelf (AIS). The black solid line is the grounding line and yellow lines show the drainage basin boundaries. (b) The three major glaciers, Lambert, Mellor and Fisher Glaciers, of the LAGS, and its topographic rises (including both ice rises and pinning points) (shaded in brown Matsuoka et al., 2015).

1.2.2 Overview of the LAGS

The LAGS extends ~1500 km from the Antarctic interior to the coast (Figure 1.2). Ice streams bring ice from as far inland as Dome Argus and Dome Fuji and they converge at the southern AIS grounding line, draining a volume of ice greater than the entire WAIS. Significant glaciers such as the Charybdis also supply the AIS. The AIS is 550 km long and 60,000 km^2 in area, the third largest ice shelf in Antarctica and the largest in East Antarctica. The glacial trough eroded by the LAGS extends 1000 km into the continental interior and reaches up to 2560 m below sea level (Fricker et al., 2002b; Galton-Fenzi et al., 2008).

An ice shelf, such as the AIS, along the ice sheet margin provides stability to the ice further inland due to a buttressing effect, a restraining action acting in the opposite direction of the ice flow (Gudmundsson, 2013; Paolo et al., 2015; Fürst et al., 2016; Reese et al., 2018b). Changes to an ice shelf do not contribute to sea-level rise directly but, under the impact of a dynamic thinning mechanism (Pritchard et al., 2009), the ice shelf can disintegrate and lead to instability of the ice sheet. On the other hand, ice streams flowing out of the continent are of concern since they contribute to sea-level rise directly. Given that the LAGS has significant regions of ice grounded below sea level (Fricker et al., 2002b; Damm, 2007; Rignot et al., 2011; Fretwell et al., 2013), the LAGS is a region of great significance for dynamic changes due to environmental variations.

1.2.3 Controls on the LAGS

Bathymetry

The shape of the AIS is very different to other big ice shelves, affecting its ice flow pattern and velocity. Occupying only 2% of the East Antarctic coastline, the AIS has a mass flux of 56.0 ± 0.5 Gt year^{-1} at its grounding line (Rignot et al., 2013). At 90 km downstream from the grounding line the ice velocity is slowed down by the narrow width (∼50 km) of the ice shelf embayment. The shape of the bathymetry (Rignot et al., 2011; Galton-Fenzi et al., 2012) and a number of topographic rises (including both ice rises and ice rumples/pinning points) where the ice shelf re-grounds, cause the ice to deviate in its flow and limit the velocity. These topographic rises project into the floating ice shelf from beneath and are known as ice rises where ice shelf flow diverts around the feature, and ice rumples or pinning points where ice flows over the top of the feature (Matsuoka et al., 2015; Favier et al., 2016). As part of the ice shelf geometry, they have the potential to influence the ice sheet dynamics.

Additional notable characteristics of the AIS are its low elevation and gradient, and its concave ice profile (White et al., 2011). The profile is attributed to enhanced flow in ice streams (Rignot et al., 2011) – a combination of basal slip and internal deformation of the ice where membrane stresses dominate. Perturbations, due to forcing, travel faster along these enhanced flow regions, for example in fast moving ice streams or ice shelves (Golledge et al., 2012).

Considering that the LAGS has grounded ice below sea level, changes in ocean climatic conditions could have a significant effect that leads to an unstable ice sheet. Ocean temperatures are, of course, not the only factors affecting the grounded marine ice by increasing basal melt rates. Topography, and cavity geometry, along with the surface characteristics of the underside of the ice shelf impact the melting rate. Basal melting is more rapid at deeper grounding lines (Silvano et al., 2016) where the volume lost by basal melt is caused by the melting of ice at the base of the ice shelf due to warm ocean temperatures and increased pressure (Jacobs et al., 1992; Bassis et al., 2008; Depoorter et al., 2013; Walker et al., 2013).

Pinning points impacting the AIS, as noted above, are visible in satellite imagery, either directly or through altered crevasse patterns or velocities (Rignot et al., 2011) but are often missing sufficient information to analyse their location, height, and extent (Matsuoka et al., 2015, pers. comm. Galton-Fenzi, 2019). Their importance for ice sheet modelling was recently investigated by Fürst et al. (2015), and observed by (Berger et al., 2016), revealing that pinning points affect ice dynamics due to ice deformation at local-scale which impacts surface velocities (Favier et al., 2016). Further study by Favier et al. (2016) shows that pinning points can decrease ice discharge by enhancing the buttressing effect of ice shelves, leading to errors in model output if they are not assimilated into the model. Inaccurate sea-level rise projections could result if pinning points and similar features are not represented well in model runs.

These recent studies suggest the need for better bathymetry knowledge around Antarctica as a whole, and imply that the bathymetric boundary conditions of the LAGS should be tested with regard to their impact on modelled ice sheet response. The bathymetry beneath ice shelves, the shape of sub-ice-shelf cavities, and presence of pinning points likely influence the impact of climate forcings on modern and past LAGS change. Well known bathymetry also provides for better projection of the migration of the grounding line and the transition zone between ice sheet and ice shelf, playing an important role in controlling marine ice sheet dynamics as it determines the rate at which ice flows out of the grounded part of the ice sheet. The grounding line location can be a variable which determines ice flux (Schoof, 2007), and together with accumulation, this location has an important control on the mass balance of the grounded ice sheet.

Calving

Calving is a process that produces icebergs in the form of large slabs of ice that break away from an ice shelf due to rifts or fractures that progressively form with the deformation and flow of the ice. Ice shelves along the ice sheet margin of Antarctica provide stability to the ice sheet through the buttressing effect noted previously (Wearing et al., 2015; Fürst et al., 2016). Calving, or thinning, of an ice shelf can therefore reduce the buttressing effect and increase the ice flux both at the ice shelf front and the grounding line. If the shelf is in a steady state then the grounding line flux is approximately equal to the sum of mass lost through calving and basal melt.

Studies of calving such as Fricker et al. (2002b) and Jansen et al. (2015) show that calving events follow an advance-calve-advance cycle. Departures from regular calving patterns are an indication of external forcings, of interest to both the cryosphere community and the general public. Many Antarctic ice shelves including the largest two, the Ross and the Filchner-Ronne, have an ice front that is wide relative to the length of the shelf, whereas the AIS is contained for much of its length in the trough-like structure of the Lambert Graben and upstream portion of Prydz Bay (Rignot et al., 2013). The smaller, Larsen C Ice Shelf in the Antarctic Peninsula, has a wide-fronted physiography and has been the subject of studies that investigate controls on rift propagation, and hence, ice shelf stability (Kulessa et al., 2014; Borstad et al., 2017). Suture zones between the rifts act as stitches to neighbouring glacier flows that inhibit the fast propagation of the rifts between the streams. Suture zones are regions of longitudinal flowbands having a heterogeneous mixture of marine ice, sea ice, meteoric ice, and mélange. These composite features make such zones malleable with no fixed orientation and therefore rift propagation is arrested in these regions unlike in meteoric ice (Jansen et al., 2013; Kulessa et al., 2014; McGrath et al., 2014; Jansen et al., 2015; Borstad et al., 2017).

Mass loss from the AIS is dominantly by calving (50 ± 6 Gt year^{-1}, Depoorter et al., 2013), and by basal melting (39 ± 21 Gt year^{-1}, Depoorter et al., 2013). Increased calving of the ice front from the AIS could therefore lead to a significant draining of ice from the EAIS, resulting in ice sheet instability. Observations of the AIS calving events may be obtained from satellite imagery, which documents an AIS calving cycle approximately every 60-70 years. The AIS ice front is heavily crevassed. Images from RADARSAT AMM-II from 2000 (Fricker et al., 2002b) show the formation of three rifts. On the western side is the famous LT rift, having a dimension of a tabular iceberg of 25km $\times$ 25km in size, while on the eastern side is a "zigzag" shape rift. This rift is causing crevasses of 40-50km long, affecting the ice flow downstream from Gillock Island, and was identified as a potential calving front for a future major calving event.

The first observed major iceberg-calving event of the AIS occurred in 1963-64, when a total area of nearly 10 000 km^2 broke from the ice front. Since then the ice shelf front has re-advanced, and now contains two longitudinal (parallel-to-flow) rifts, referred to as the east and west rifts, which are roughly parallel to the direction of the ice flow. A transverse rift (perpendicular-to-flow) starting from the base of the western rift of the feature called the Loose Tooth (LT) has propagated and widened with time, as a precursor of calving event (Zhao et al., 2013). The existence of prominent active rifts across the ice front (Walker et al., 2013), and the calving of iceberg D28 on 26th September 2019, before the ice front reached the same extent into Prydz Bay as in 1963, motivate further investigation into the criteria for calving, and its effect on the stability of the AIS if further retreat from its present day configuration occurs. Calving is interesting both to the ice sheet community and the general public as it is a phenomenon that indicates the changeable, perhaps precarious, state of the ice sheet.

Basal Melt

Since the AIS produces a large amount of basal meltwater, comparable to Ross Ice Shelf or Filchner-Ronne Ice Shelf (Galton-Fenzi et al., 2012), the dynamic interface between ice and ocean is particularly significant. This is highlighted by the LAGS having some of the deepest ice ($\sim$ 2500 m below sea-level rise) in the Antarctic continent (Fricker et al., 2001, 2002a; Craven et al., 2009a; Galton-Fenzi et al., 2012; Fretwell et al., 2013). After calving, basal melt is the secondary contributor to negative mass balance of the LAGS (Rignot et al., 2013), and its spatial distribution impacts ice thickness, velocity, and migration of grounding line on the AIS. The presence of the sub-ice cavity at the southernmost part of the grounding line where deep ice is located impacts both the ocean current path underneath the ice shelf, and the basal melt locally (Galton-Fenzi et al., 2008, 2012; Rignot et al., 2013).

The process of meltwater production is due to changing temperature and hydrostatic pressure. The in situ freezing point temperature of seawater decreases with depth due to increased pressure in the water column and due to intrusion of saline Circumpolar Deep Water. This temperature difference is associated with the spatial distribution of basal melt and refreezing at the base of the cold-cavity AIS (Dinniman et al., 2016; Reese et al., 2018a). High salinity shelf water mixed with Circumpolar Deep Water is the main water mass that drives melting in the cavity under the AIS (Galton-Fenzi et al., 2012).

The existence of circulation of meltwater and formation of marine ice underneath the AIS (Fricker et al., 2001; Treverrow et al., 2010; Galton-Fenzi et al., 2012) is consistent between studies. However, there are discrepancies between estimates of net basal melt ice loss for the AIS (and hence mass balance estimates). As noted above, basal melting has been calculated at (39 $\pm$ 21 Gt year^{-1}, Depoorter et al., 2013). Other studies arrive at figures of 51.5 $\pm$ 9.6 Gt year^{-1} and 46.4 $\pm$ 6.9 Gt year^{-1} (Wen et al., 2010), 35.5 $\pm$ 23 Gt year^{-1} (Rignot et al., 2013), and 27 $\pm$ 7 Gt year^{-1} (Yu et al., 2010). An independent numerical ocean model study simulates ice flux due to basal melting with estimation at 45.6 Gt year^{-1} (Galton-Fenzi et al., 2012). The wide ranging results above suggest that better direct observations leading to estimates of basal melt, and an improvement in numerical models to translate the observations into physical understanding, are needed. These would enable progress towards a consolidated fit between observations and modelled results.

1.3 Previous modelling studies of AIS and LAGS

There are a limited number of modelling studies that have investigated ice dynamics of the AIS, with most studies based on field data (including the application of the Global Positioning System) or satellite imagery. Nevertheless, there have been two studies investigating the sensitivity of AIS models to input parameters. Pittard (2016) explored the sensitivity of the AIS to geothermal heat flux and found that slow-moving regions of ice were most sensitive to increases in heat flux. Sun et al. (2014) used the BISCICLES model to look at the impact of random small-amplitude height fluctuations that were added to the bedrock topography of Bedmap2 (Fretwell et al., 2013), with results showing that the model of AIS was less sensitive to bedrock uncertainty than other regions of Antarctica. Two further modelling studies have looked at potential future climate forcing of the AIS. Gong et al. (2014) and Pittard et al. (2017) both investigated the response of the AIS to future scenarios of increased air temperature over the next few hundred years (200 and 500 years respectively). Both find that the AIS is stable under future climate warming, with increased basal melt offset by increased surface accumulation.

Basal melt is a significant source of mass loss for the AIS. Basal melt and refreezing under the AIS has been numerically investigated by Jacobs et al. (1992), Williams et al. (2001), and Hellmer (2004). Reese et al. (2018b) and Richter et al. (2020) also produced ocean models for the whole of Antarctica including the AIS. However, none of the studies agrees well on basal melt flux or spatial pattern of basal melt and refreezing underneath the AIS. A new bed geometry underneath the AIS was produced by Galton-Fenzi et al. (2008), who found that the shape of the sub-ice shelf cavity under the AIS extends further south and deeper than suggested by BEDMAP2 (Fretwell et al., 2013). The shape of the cavity influences the modelled rates of melting and freezing under the AIS. The only study that has adopted the improved bathymetry underneath the AIS is Galton-Fenzi et al. (2012), and this model gives the best fit to observed melt rates Rignot et al. (2013).

One shortcoming of most previous studies of the Lambert-Amery Glacial System, is that they used outdated bathymetry data which may have affected results such as ice thickness and velocity. No previous studies investigating the stability of the AIS have examined the performance of calving models. Lastly, most ice sheet modelling studies till present have used a simplified parameterisation to represent ice-ocean interaction, which may affect estimates of how the ice shelf will evolve with time. These shortcomings are addressed in this thesis.

1.4 Ice Sheet Modelling

1.4.1 Overview

Ice sheet models are computer-based frameworks for analysis, where the mathematical formulae which represent the behaviour of ice are written in computer code, and whereby the resulting equations are solved numerically. Ice sheet models are used by researchers who study ice or climate to investigate the nature of ice at present and/or to quantify predictions of further ice sheet evolution.

Numerical ice sheet models must be supplied with input data to set boundary conditions and model parameter values. Boundary conditions are typically environment variables such as air temperature and precipitation rate. Model parameters may either take a constant value, such as ice density or acceleration due to gravity, or they may be parameters that need to be tuned. The latter parameters are those that do not have a universal constant value in the model, but need to be varied systematically within the range allowed by a mathematical equation that represents this varying parameter. The tuning process for ice sheet modelling is typically a major undertaking. Systematic searches of the variable parameters, especially those known to have greatest impact, are carried out. Model runs are typically deemed successful when the output is a close match to observations of the given ice sheet.

There are different types of ice sheet model depending on the approximation of the nine principal stress components that describe the flow of ice. The equation set that describes the fluid dynamics of ice by predicting fluid velocity and pressure at any given point is known as the Full Stokes Equation (FSE), a linearisation of the Navier-Stokes (NS) equations. The FSE in the Cartesian system (x,y,z) is given as:

$$\frac{\partial}{\partial x}(2\mu\frac{\partial v_x}{\partial x}) + \frac{\partial}{\partial y}(\mu\frac{\partial v_x}{\partial y} + \mu\frac{\partial v_y}{\partial x}) + \frac{\partial}{\partial z}(\mu\frac{\partial v_x}{\partial x} + \mu\frac{\partial v_z}{\partial z}) - \frac{\partial p}{\partial x} = 0 \tag{1.1}$$

$$\frac{\partial}{\partial x}(\mu\frac{\partial v_x}{\partial y} + \mu\frac{\partial v_y}{\partial x}) + \frac{\partial}{\partial y}(2\mu\frac{\partial v_y}{\partial y}) + \frac{\partial}{\partial z}(\mu\frac{\partial v_y}{\partial z} + \mu\frac{\partial v_z}{\partial y}) - \frac{\partial p}{\partial y} = 0 \tag{1.2}$$

$$\frac{\partial}{\partial x}(\mu\frac{\partial v_x}{\partial z} + \mu\frac{\partial v_z}{\partial x}) + \frac{\partial}{\partial y}(\mu\frac{\partial v_y}{\partial z} + \mu\frac{\partial v_z}{\partial y}) + \frac{\partial}{\partial z}(2\mu\frac{\partial v_z}{\partial z}) - \frac{\partial p}{\partial z} - \rho g = 0 \tag{1.3}$$

and the mass continuity equation for incompressible flow is:

$$\frac{\partial v_x}{\partial x} + \frac{\partial v_y}{\partial y} + \frac{\partial v_z}{\partial z} = 0 \tag{1.4}$$

where μ is the ice effective viscosity

v is the fluid velocity of ice in x, y (horizontal) and z directions

p is the pressure of ice

ρ is the density of ice, and

g is the acceleration due to gravity

Models that use the FSE such as ISSM and Elmer/Ice (Larour et al., 2012; Gagliardini et al., 2013) have been considered computationally expensive. There is, therefore, a hierarchy of models that employ various approximations to reduce the necessary computation time and hardware resources. The simplest approximation is the shallow ice approximation (SIA) model also known as a 'zero-order' model (Bueler et al., 2007). This approximation neglects both the longitudinal and transverse stresses, and the vertical stress gradient. The SIA assumes that the horizontal shear stress component of flow is small, and therefore the flow is dependent on the vertical shear stress gradients that oppose the gravitational driving force. The SIA makes the assumption that the gravity driving force is exclusively balanced by the shear within the ice, leading to the simplification of the FSE by neglecting the horizontal shear. Another widely used approximation is the Shallow Shelf Approximation (SSA). This was developed to compute ice flow in ice shelves where basal shear stress is zero and longitudinal stresses dominate Bueler and Brown (2009). The SSA is also a zero-order model but has a depth-averaged ice velocity.

Hybrid models may also be used. Here, the SIA and SSA are superposed which results in an integrated sliding law for a grounded ice sheet, combining the ice streams and ice shelves. Parallel Ice Sheet Model (PISM) is an example of a hybrid model, a model that makes use of approximations to compute efficiently the SIA and SSA stress balance. It is capable of carrying out simulations faster than FSE models, thus allowing exploration of multiple parameters and flexibility in the physical variables that control ice dynamics and configurations but the simplification of stress components in the ice can result in errors in tracking of the migration of the grounding line at low resolution (Feldmann et al., 2014).

1.4.2 Parallel Ice Sheet Model

Parallel Ice Sheet Model (PISM: User's Manual available at www.pism-docs.org) version 0.7.3 (Bueler et al., 2007; Bueler and Brown, 2009; Winkelmann et al., 2011; Martin et al., 2011) is a 3D, thermomechanically-coupled, hybrid model, i.e the shallow ice approximation (SIA) and shallow shelf approximation (SSA) are superposed. SIA dominates in grounded ice with a non-sliding base, while SSA dominates for ice shelves and ice streams on grounded ice. SIA and SSA horizontal velocities are computed in the whole continental domain, and transition from one to another is calculated by a weighting function for a continuous smooth transition from SIA across the grounding line to SSA (Bueler and Brown, 2009). Using only the non-sliding SIA stress-balance yields an ice sheet that becomes too thick and lacks the computational capability to evaluate the dynamics of outlet glaciers and ice shelves. Whereas, a stress-balance that has both SIA and SSA can capture fast narrow troughs like the AIS.

The flow law connects stress to velocity and is given by

$$\dot{\epsilon}_{ij} \equiv \frac{1}{2}\left(\frac{\partial v_i}{\partial x_j} + \frac{\partial v_j}{\partial x_i}\right) = EA(T^*)(\sqrt{(1/2)\tau_{ij}\tau_{ij})}^{n-1}\tau_{ij} \tag{1.5}$$

where $\dot{\epsilon}$ is the strain rate tensor

i and j are indices that denote the two horizontal components of vertically-integrated terms.

v is the horizontal velocity

E is the enhancement parameter

A(T*) is ice softness, and (T*) is ice temperature (Paterson and Budd, 1982), and

τ is the deviatoric stress tensor.

The inversion of the above flow law gives the effective viscosity depending on the effective strain rate and the temperature of the ice. The annual mean surface temperature (RACMO2.3/ANT27, years 1979-2014; Van Wessem et al., 2014) and geothermal heat flux (An et al., 2015) are provided as boundary conditions for the advection and vertical conduction of heat through the grounded ice layers, and the pressure melting temperature is used as the basal boundary condition in the case of ice shelves (Winkelmann et al., 2011). PISM calculates the ice temperature in these unequal horizontal layers. Another important parameter from the above equation is the enhancement parameter, which is set during the tuning procedure to adjust the ice softness in both the SSA and SIA equations to match observed velocities.

Depending on the nature of the experiment to be carried out from the initial steady state, the experiment will follow one of two types of modelling procedures: diagnostic modelling and prognostic (or predictive) modelling. Diagnostic modelling is a time-independent simulation, carried out to understand the physical processes that occur in an ice sheet or an ice shelf, and the way that they are likely to impact on ice dynamics. In a prognostic modelling experiment, by using a suitable time-variable input data set an investigation can explore the model response to the input under investigation from the the past to the future, or the present to the past. For example, a prediction of a contribution to sea-level rise can be made from data on past climate, or a past ice sheet can be reconstructed.

Boundary and forcing conditions

A pseudo-plastic sliding law is used to control the basal strength assuming that there is a layer of till underlying the grounded ice (Winkelmann et al., 2011; Bueler and Brown, 2009). The sliding law is given by:

$$\tau_b = -\tau_c \frac{\mathbf{u}}{u_{\text{threshold}}^q |\mathbf{u}|^{1-q}} \tag{1.6}$$

where τ_b is basal shear stress

$u_{\text{threshold}}^q$ is a threshold velocity whose default value is 100 m year^{-1}

τ_c is the yield stress, and

q is the exponent which can be tuned to adjust the sliding

(if $q = 0$, then the sliding law becomes a purely plastic sliding model).

The spatial location of ice streams is calculated from the yield stress, which is dependent on a subglacial hydrology model (Aschwanden et al., 2012, 2016), and the modelled till strength, which is a function of bed elevation (Martin et al., 2011; Winkelmann et al., 2011; Aschwanden et al., 2016). We use a default hydrology model where water is not conserved but it is stored locally in the till up to 2 m, and any amount higher than this maximum value is lost with no feedback. The yield stress is determined by:

$$\tau_c = c_O + (\tan\phi) N_{til} \tag{1.7}$$

where c_O is called the “till cohesion”, whose default value in PISM is zero

N_{til} determines the effective pressure, and

ϕ is the till friction angle, a piecewise-linear function of bed elevation given as

$$\phi(x,y) = \begin{cases} \phi_{min}, & b(x,y) \leq b_{min}, \\ \phi_{min} + (b(x,y) - b_{min})M, & b_{min} < b(x,y) < b_{max}, \\ \phi_{max}, & b_{max} \leq b(x,y) \end{cases} \tag{1.8}$$

where b_{min} and b_{max} are thresholds in the bed elevation, and

M is defined as $(\phi_{max} - \phi_{min})/(b_{max} - b_{min})$.

Forcing conditions for the present day atmosphere are spatially distributed near-surface air temperatures, and precipitation (for which we use RACMO2.3/ANT27, years 1979-2014; Van Wessem et al., 2014). The surface mass balance is computed from this input data. The air temperature is used to calculate the energy available to melt ice at the ice surface interface by employing a positive degree-day (PDD) model (Aschwanden et al., 2013; Seguinot et al., 2014). PDD is defined as the integral of temperatures above 0 ° C in one year, which in our case is between 0.37 K and 8.36 K. The lapse rate (8.0 K km^{-1}) applied to the 2 m air temperature forcings serves as the boundary condition for the conservation of energy equation which corrects the differences between the fixed surface ice elevation and the time evolving modelled elevation (Aschwanden et al., 2013; Seguinot et al., 2014). The ice shelf basal melt rate is controlled by the ocean's potential temperature (271.3 K) and salinity of the adjacent ocean (27.0 g/kg), which were used to initialise basal melt at the ice-ocean boundary layer (Holland and Jenkins, 1999). These are varied in Chapter 4 to investigate the effect of different ice-ocean interface parameters.

The calving rate at the ice margin is calculated from horizontal strain rates (Levermann et al., 2012) in combination with a prescribed minimum ice thickness of the ice front. This implies that the calving mechanism is related to the principal strain rate and an imposed minimum threshold value of the ice front:

$$c = K\dot{e}_{+}\dot{e}_{-} \tag{1.9}$$

where c is the average calving rate (m year^{-1}).

K is a constant parameter which can be tuned to match observed calving rates (Levermann et al., 2010, 2012), and

$\dot{e}_{+}$ and $\dot{e}_{-}$ are the principal horizontal strain rates (sec^{-1}).

In PISM there are four calving models from which two are employed: 1) The physically-based 2D calving parameterisation that implements a parameter (K) which incorporates the material properties of the ice, referred to as "eigencalving", and 2) a thickness threshold at the ice front. Both of these calving models were implemented simultaneously. The requirement for the latter calving law is to set a thickness (in m) where the thin widespread ice front that has values below the imposed thickness threshold value will calve from the ice front of the ice shelf.

Model domain

In our experiments, PISM is applied to the whole continent of Antarctica. For the initial spin-up process a uniform 10 km horizontal resolution was employed. Once a suitable steady state was reached, the model outputs from the coarse resolution were regridded to a 5 km horizontal resolution to capture the ice dynamics at finer resolution, which becomes the initial state for Chapter 2 only. All simulations are carried out in a computational box of 10 km horizontal resolution with a maximum height of 6000 m, having 21 vertical layers of ice thickness in the positive z-axis ranging from 71.87 m to 428.12 m depending on the local ice thickness.

The simulations at coarse resolution do not resolve ice dynamics in an optimal way but enable multiple simulations to be run in a reasonable time, with available computing resources. At this stage, the simulations allow exploration of glaciological parameters for ice dynamics, rheology, subglacial hydrology, and calving that produce the best fit to the current LAGS configuration. The simulation at 10 km horizontal resolution which produces the best fit to the present day LAGS configuration is further tested at 5 km horizontal resolution. Numerical models can be resolution sensitive, but simulations at fine resolutions can be beyond the limit of the available computational resources, therefore the parameter search at coarse resolution is a compromise that is kept in mind when evaluating results.

The geometry of the domain is given by ice thickness from BEDMAP2 (Fretwell et al., 2013) and bedrock elevation data from BEDMAP2 (Fretwell et al., 2013) stitched to data from RTOPO-1 (Timmermann et al., 2010) underneath the ice shelf, as previously used by Pittard (2016). An initial appraisal of the geometry input data (shown in Chapter 2) revealed that the bedrock elevation at the southern-most grounding line of AIS in BEDMAP2 is much shallower than other data sources such as RTopo-1 (Timmermann et al., 2010), which includes the shape of the sub-ice shelf cavity underneath the AIS developed by Galton-Fenzi et al. (2008), and BedMachine by Morlighem et al. (2019). This region of elevated bathymetry causes the modelled grounding line to advance substantially, leading to inaccurately high values of grounded ice thickness. This work therefore uses a modified geometry (Figure 1.3) for areas beneath the floating ice shelf developed from that used by Pittard (2016) in order to improve the match between model and observation.

Our modified geometry was made by firstly applying linear smoothing through a convolution, affecting only neighbouring grid points on the topography and leaving the bathymetry bed elevation untouched. This was done only on the southern most part of the AIS within the enclosed region shown in Figure 1.3. The bed elevation was manually manipulated on certain grid cells to minimise the resulting abrupt drop, being cautious not to over-smooth. Hence, the topography of the grounded ice is constrained using BEDMAP2, whilst the bathymetry beneath the AIS and offshore is taken from RTOPO-1 (Timmermann et al., 2010), which incorporates an improved geometry of the AIS subglacial cavity from Galton-Fenzi et al. (2008) and our geometry modifications (Figure 1.3).

1.4.3 A steady state model for the LAGS in PISM

All ice-sheet models require initial conditions to begin their simulated time evolution. One common initial condition, useful when observed data cannot be used as an initial condition, is the steady state configuration of the ice sheet in question. A steady state configuration is one which has evolved for a sufficiently long time under constant parameters and boundary conditions that the ice sheet no longer changes with time. This configuration has the advantage of being realistic in that most ice sheets today are at or near steady state conditions, due to the fact that climate changes over the past have been quite slow, and only now, with human influences, are they suddenly changing. It is defined here as being where the grounding line is stabilised, the rate of change of ice volume approaches zero in the last 100 years (Bueler and Brown, 2009), and the rate of change of enthalpy approaches zero in the last 1000 years of the simulation (Pittard, 2016). The modelled steady state is an acceptable initial state if it replicates the current configuration of the LAGS variables such as: grounding line position, calving front position, ice thickness, ice flow pattern, and ice surface velocity.

To obtain a steady state model, a multi-phase initialisation spin-up procedure was used. The first step in the multi-phase procedure uses the geometry datasets described above to set up

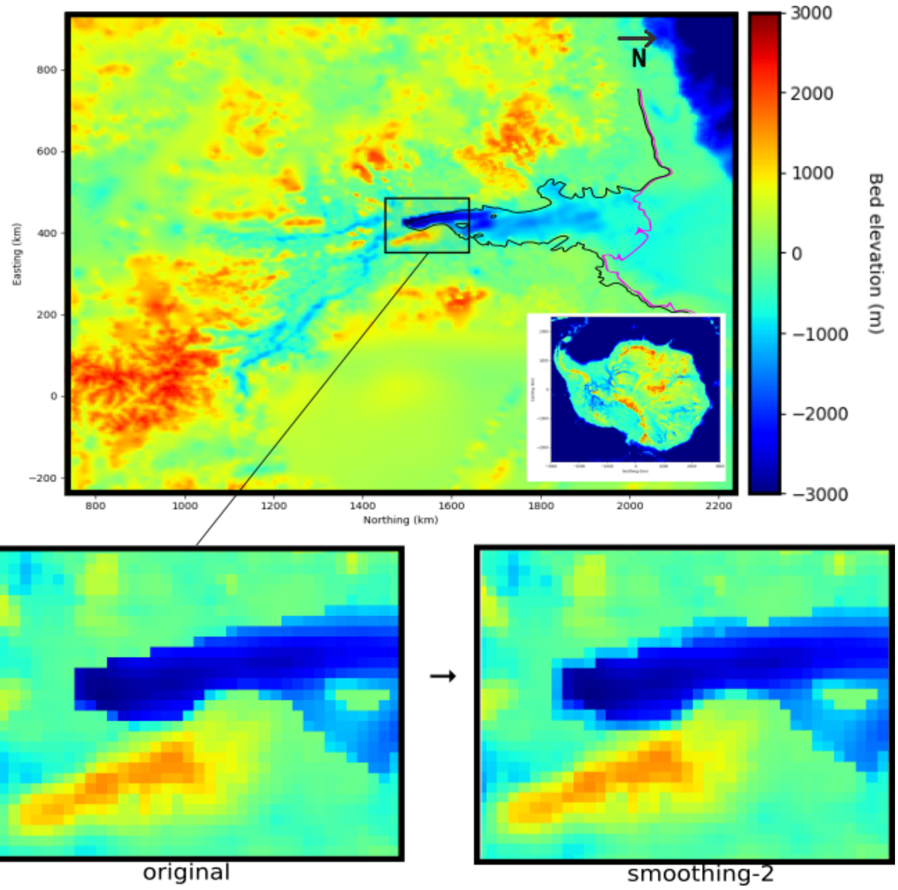

Figure 1.3: Bed elevation of the LAGS where modifications (refer to main text) were applied to the topography of BEDMAP2 to decrease the steep slope between the topography and bathymetry.

the computational domain. The second stage, which runs for 100 years, is the 'smoothing' stage. This stage uses the stress balance only for grounded non-sliding ice, i.e where the basal drag is very high, to smooth out the peaks in stress arising from ice surface roughness. The smoothed ice surface output is then supplied to the next stage where the geometry is held fixed to allow the thermal fields to evolve for 250 ka. The long duration is due to the slow rate of advection of thermal parameters within the ice sheet. From the thermally-evolved ice sheet (thermal structure of the ice sheet has been resolved), all lateral boundaries, and geometry are free to evolve in the last stage of the spin-up. This permits the ice sheet configuration within the computational domain to naturally evolve to a modelled equilibrium state of grounding line position, ice stream locations, and calving fronts which can be compared to observational data.

Parameter tuning

PISM has multiple choices for parameters that control ice flow, ice softness, sliding, and calving of ice front that affect ice dynamics of grounded ice and floating shelf (https://pism-docs.org/wiki/doku.php). The steady state solution was found using six optimised variables: sia_e, ssa_e, q (Eq 6), till (Eq 7), K (Eq 9), and thk by generating a 50 member Latin hypercube (Santner et al., 2003) within the ranges as shown in Table 1.1 (tuning performed by Steven Phipps, pers. comm. 2019).

Variable	lower range	upper range
sia_e (unitless)	1.0	4.5
ssa_e (unitless)	0.5	1.6
q (unitless)	0.15	1.00
till (unitless)	0.010	0.040
K (m s)	3.0e+16	1.0e+19
thk (m)	150	300

Table 1.1: Optimised variable ranges

Ice thickness and extent data were compared to the BEDMAP2 data set (Fretwell et al., 2013) (Figure 1.4 first panel). The upper ice surface velocity for the LAGS was compared to observed data (from Rignot et al., 2011, Figure 1.4, second panel). These two data sets were, it is noted, compiled/collected at different times: BEDMAP2 was compiled from multiple sources and published in 2013, while ice velocities were obtained from multiple satellite interferometric synthetic aperture radar images between 2007-2009. The periods of observation are sufficient to represent the observed LAGS configuration and flow dynamics because the AIS is understood not to be changing rapidly, and therefore these dynamic variables would not change over the space of a few years.

The current work makes use of preliminary modelling associated with a modern whole-continent Antarctic study at 15 km horizontal resolution (Steven Phipps, pers. comm.) which would not necessarily be optimised for the LAGs in particular. The bathymetry from BEDMAP2, as used in the whole-continent work, is too shallow under the AIS (as noted previously), however, the parameters used for the whole-continent provided a comparable match for grounding line position, ice thickness and velocity using our modified bathymetry, but not the calving front position of the AIS. Hence parameters that affect the calving front were further tuned based on BEDMAP2 ice front thickness and a previous study of the AIS by Pittard (2016). Table 1.2 shows the combination of values for the thickness threshold and eigencalving parameter (Levermann et al., 2012) that were tested to improve the calving front position of the AIS.

The modelled steady state of C1 is a retreated calving front at the centre of the Amery Ice Front, while C2 is an advanced calving front that again shows a retreated calving front at the centre

Identifier	Thickness threshold	Eigencalving
C1	200 m	3.3e+17
C2	225 m	3.3e+17
C3	176 m	2.0e+15
C4	176 m	2.0e+16
C5	225 m	1.9e+15

Table 1.2: Tuning of calving parameters at 10 km resolution

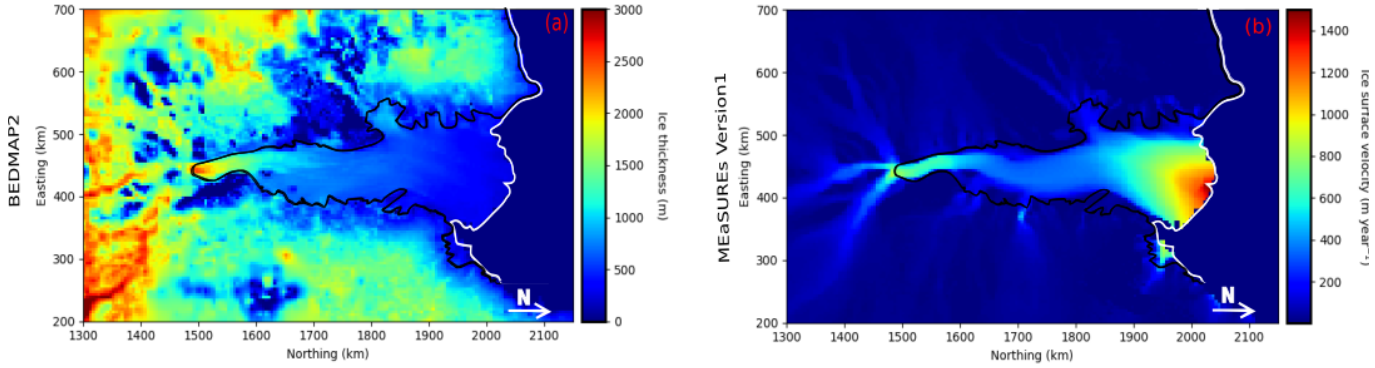

Figure 1.4: Ice thickness and upper ice surface velocity at 5 km resolution, from Fretwell et al. (2013) and Rignot et al. (2011) respectively, are used as present day constraints for the modelled steady state. Eastings and Northings here and on figures throughout the thesis relate to the grid used within PISM.

of the AIF. C3 produces an ice thickness that exceeds the computational domain, which causes the simulation to end before it reaches a steady state, and C5 produces an advanced calving front. The difference between C2 and C5 is the shape of the calving front: in C2 the centre of the calving front is retreated giving a concave profile while C5 gives a convex profile of the AIF. Since C2 and C5 have the same ice thickness threshold, it is likely that the eigencalving value generated the difference in the ice front profile. In C2, the eigencalving parameter is higher, which causes calving at a much faster rate than C5 in areas where both principal strain rates are positive (which occurs most commonly in the centre of the ice shelf). C4 parameter values give the best fit to the BEDMAP2 ice extent, although C4 shows slight advancement of the calving front on the eastern side of the AIF, and a slightly higher ice velocity (Figure 1.5a-1.5c).

Figure 1.5 second column, shows the modelled steady state at 5 km compared to the BEDMAP2 grounding line (Figure 1.5d), ice thickness (Figure 1.5f), and compared to Rignot et al. (2011) for ice velocity (Figure 1.5e). There is high misfit in velocity at the deep grounding line where the topography meets the bathymetry despite the smoothing performed. The misfit in velocity is likely caused by the abrupt drop in bedrock elevation (Figure 1.3 smoothing-2) causing ice to flow with high velocity across the height difference. The misfit in ice thickness is also more pronounced in the south of the AIS across the same spatial coordinates where velocity misfits occur. Despite these misfits, the grounding line position matches closely to present day observations, which is the first priority in our study, and the velocity and ice thickness misfit decreases along the shelf towards the ocean. This steady state is used as the initial state in Chapter 2, where other bedrock geometries and the addition of pinning points to the geometry are explored. The updated steady state model produced during the experiments detailed in Chapter 2 is then used as the initial state for the chapters that follow.

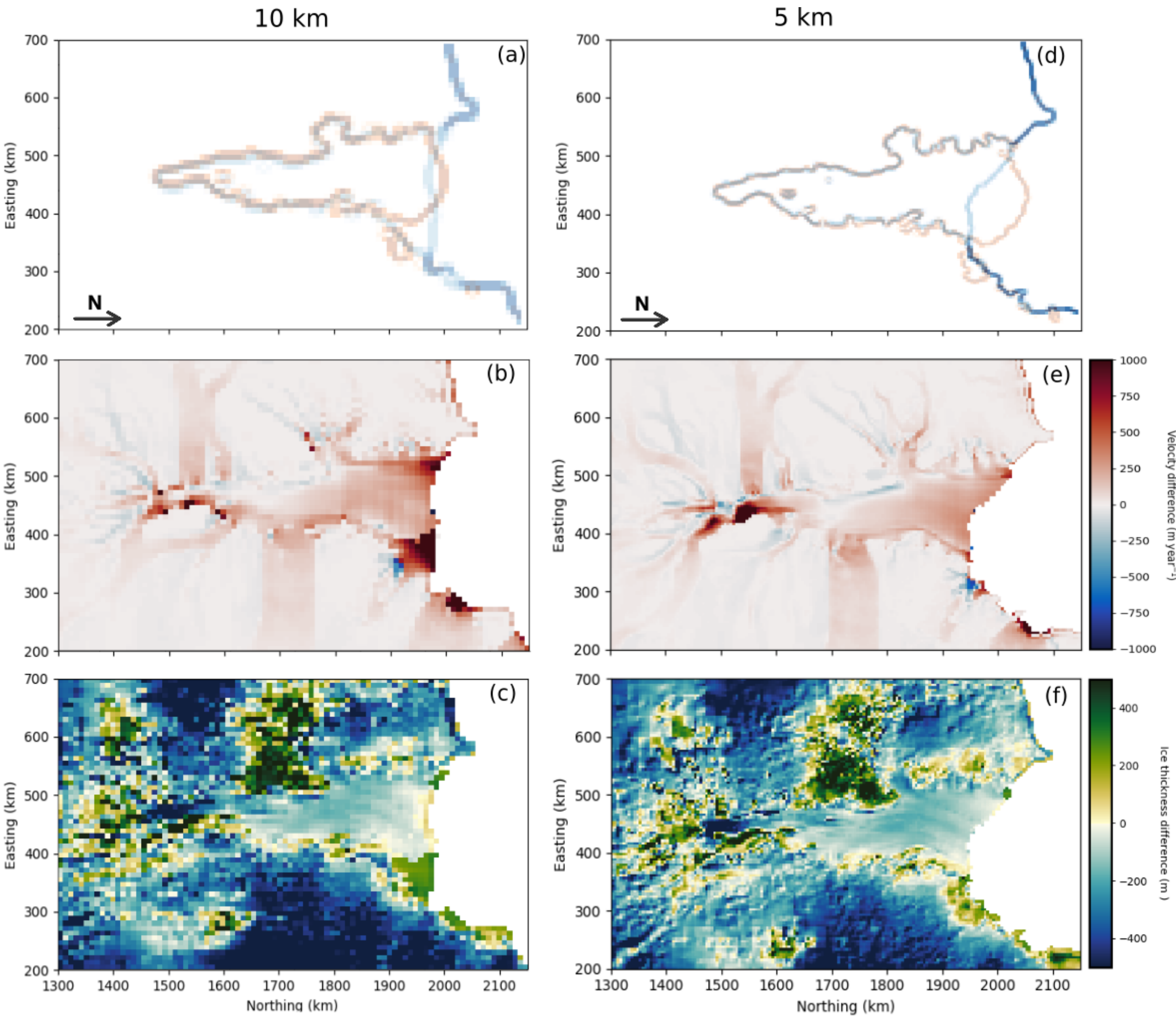

==

Figure 1.5: 1st column shows (a) modelled grounding line and ice extent (blue line) compared to BEDMAP2 (orange line), (b) ice velocity compared with Rignot et al. (2011), and (c) ice thickness compared to BEDMAP2; for a 10 km model resolution where calving parameters have been tuned. 2nd column shows a similar comparison for a 5 km model resolution using the same tuned parameters as the 1st column.

Parameter	Value	Description
sia_e (unitless)	2.7	Enhancement factor for grounded ice where vertical shear dominates.
ssa_e (unitless)	1.8	Enhancement factor for floating ice where horizontal shear dominates.
q (unitless)	0.8	Exponent in the pseudo-plastic flow law (Eq 6).
till (unitless)	0.01	A tuning parameter of the effective pressure of ice against pressurised water in the till, (Eq 7).
ϕ (unitless)	10.0, 25.9, -760.0, 1279.0	Tuning parameter of till strength, depending on bed elevation. It varies the strength of the basal resistance by setting till friction angle as a function of bed elevation, i.e at -760 m bedrock depth till angle is 10.0°, and when bedrock depth goes to 1279 m, till angle is 25.9° (Eq 8).
K (m s)	2.0e+16	Eigencalving parameter, relating calving rate to principal strain rates (Eq 9, Levermann et al. (2012)).
thk (m)	230.0	Minimum thickness limit where ice below this thickness is calved from the ice front of an ice shelf.

Table 1.3: Parameter choices

Context of the modelling research described this thesis

At the outset of this research, the decisions to use PISM for the numerical modelling and the use of a relatively large Antarctic domain were based on the potential extension of the modelling back to the Last Glacial Maximum. It was hoped to model the LAGS both for sensitivity to parameters of the present day (as has been achieved) and also over a longer time frame, with the context of modelling across the whole continent being provided by other researchers. This extended modelling proved impractical in the timeframe of the PhD candidature, and was also limited by unforeseen computing resource constraints including the severe flooding of 11 May 2018 that badly impacted the University of Tasmania high-performance computing facilities. It is acknowledged, therefore, that some limitations in the presented work (e.g. model resolution) relate to a research context extending beyond the work described in this thesis. The main research findings should nevertheless be robust, and able to be taken forward in informing future research.

1.4.4 Overarching investigations undertaken in this thesis

In this study an investigation of the dynamic response of the Lambert-Amery Glacial System to topographic geometry perturbations, the calving response to different scenarios of retreat for the Amery Ice Shelf, and the effect of model choices on basal melting and refreezing underneath the Amery Ice Shelf are explored. In so doing, this research appraises the misfits between simulated modelled outputs and observations. Hence, a general aim of this research is to progress understanding of whether the misfits occur through lack of detail in the currently available datasets, and/or parameter choices, that are used as boundary conditions for ice sheet modelling.

Chapter 2

Influence of the Bathymetry and Pinning Points on the Lambert-Amery Glacial System Ice Flow

Abstract

The Lambert-Amery Glacial System (LAGS) is composed of glaciers that terminate in the Amery Ice Shelf (AIS), together forming a drainage system which is the largest in East Antarctica. The AIS is the third largest ice shelf in Antarctica, but accounts for only 2% of the whole East Antarctic coastline. The spatial variability of the bathymetry underneath the AIS is partly known, although at low resolution. Bathymetry is important in ice sheet modelling, as high points often behave as pinning points, which impact the motion of and propagation of stress within the ice. Bathymetry can also control warm water pathways, which also influence ice sheet evolution. Herein a numerical ice sheet model at 5 km resolution was used to assess the influence of the bathymetry and pinning points on the ice dynamics of the LAGS. First, a present day configuration was simulated to obtain a steady state that fits closely to present-day observations. The steady state was then perturbed by changing the geometry to investigate the sensitivity of the LAGS model to bathymetry, and to pinning points near the calving front. Our results show that the bathymetry and the presence of pinning points are important boundary conditions in modelling the LAGS. The choice of bathymetry, and in particular the presence or absence of pinning points, substantially impacts the modelled grounding line position, the ice velocity across the grounding line, and the calving front position. The inclusion of pinning points near the calving front is critical since they generate a calving front position close to the present-day observations and additionally reduce the misfit between observed and calculated ice velocity across the grounding line. On the basis of these sensitivity tests, we show that an under-sampled bathymetry can lead to undue emphasis on poorly constrained ice sheet model

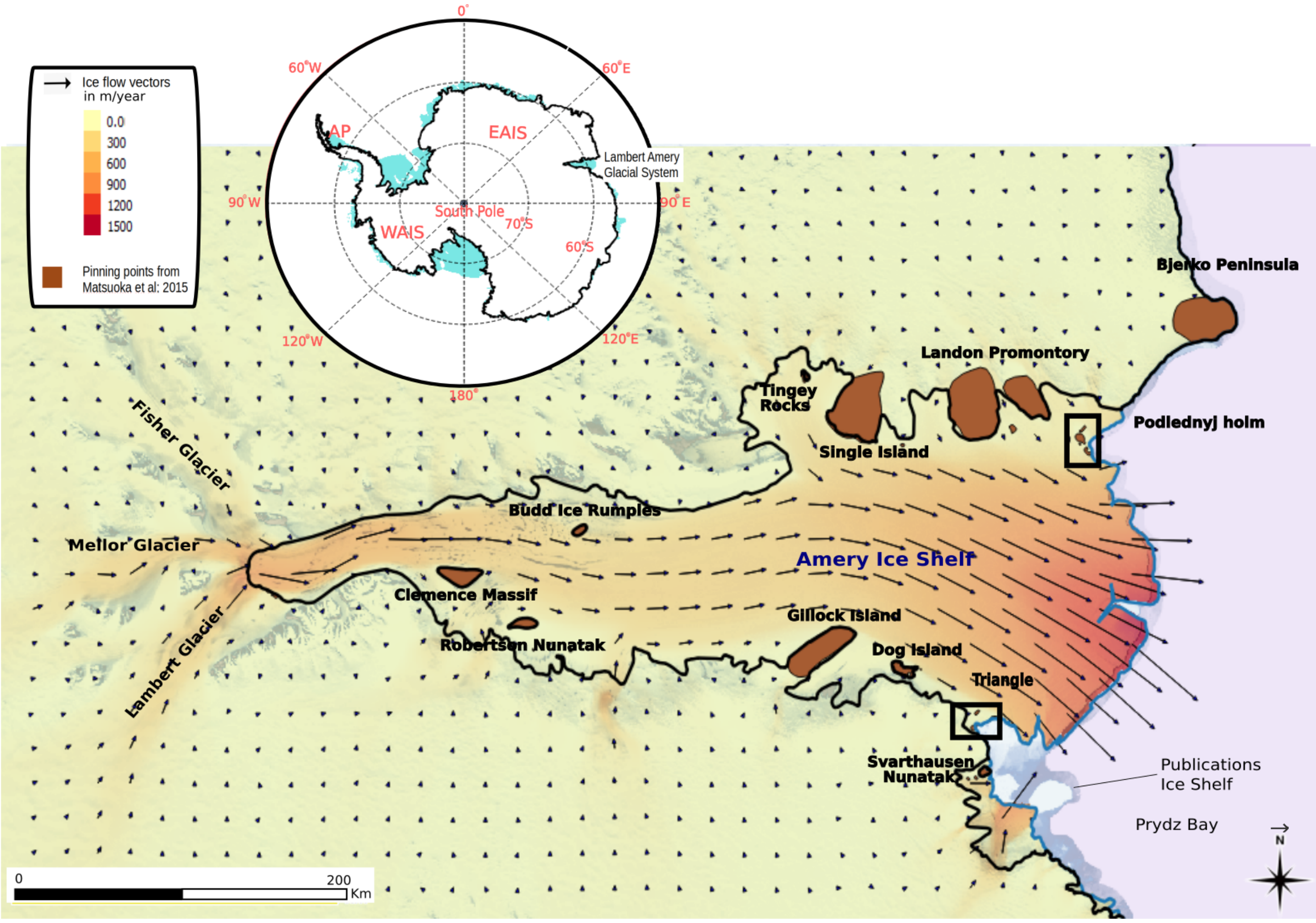

Figure 2.1: Inset: Location of the Lambert-Amery Glacial System (LAGS) in the East Antarctic Ice Sheet (EAIS) showing the location of the South Pole, West Antarctic Ice Sheet (WAIS), and Antarctic Peninsula (AP). Main map: The Amery Ice Shelf (AIS), along with the ice streams that feed it, taken from MODIS Mosaic Version 1; pinning points (brown; Matsuoka et al., 2015), and ice flow vectors (Rignot et al., 2011).

parameters when reproducing ice shelf extent. This shows the complex feedback between modelled ice dynamics and bathymetry, and the importance of bathymetry in future glacial system modelling.

2.1 Introduction

The Lambert-Amery Glacial System (LAGS) drains 10% of the grounded ice of the East Antarctic Ice Sheet (EAIS) through its major glacier, the Lambert Glacier, and other tributary glaciers (Zwally and Giovinetto, 2011). These glaciers feed the floating extension of the ice sheet that is the Amery Ice Shelf (AIS). Although the AIS spans only $\sim$ 200 km of the East Antarctic coastline, it has a significant impact on the overall mass balance of the EAIS as this drainage basin drains a volume of ice greater than the entire West Antarctic Ice Sheet (WAIS, Fricker et al., 2002b).

Ice shelves can affect the velocity of the Antarctic Ice Sheet by providing buttressing to the ice upstream, i.e. providing a force acting on a plane perpendicular to the ice flow (Dupont and Alley, 2005; Borstad et al., 2013; Gudmundsson, 2013; Liu et al., 2015). Buttressing slows down the flux of grounded ice to the ocean and can be caused by lateral shearing, which resists ice flow along lateral boundaries, by the presence of pinning points, which generate friction where they contact the base of an ice shelf, and by ice rises which obstruct the ice flow. Mass loss by basal melting or iceberg-calving of an ice shelf does not contribute substantially to sea-level rise since the volume of water has already been displaced by the volume of the floating ice. However, mass loss from an ice shelf can affect the stability of a drainage system by reducing the buttressing effect and increasing the rate of grounded ice discharge across the grounding line (i.e. the point at which grounded ice starts to float; Scambos et al., 2004; Rignot et al., 2004).

Recent glaciological studies modelling the Antarctic Ice Sheet under different boundary conditions indicate that the bathymetry and pinning points play an important role in ice sheet dynamics (Sun et al., 2014; Fürst et al., 2015; Bart et al., 2016; Berger et al., 2016; Silvano et al., 2016) as they impact directly on the surface undulation of ice streams, migration of grounding lines and glacier dynamics. The geometry of the bathymetry also influences deep ocean water currents, as deep troughs may allow the intrusion of circumpolar deep water (Galton-Fenzi et al., 2012) to reach under an ice shelf, enhancing basal melt (Nitsche et al., 2017). In other words, the bathymetry and pinning points impact the ice shelf configuration (e.g. geometry, ice thickness, ice velocity, and deformation of ice) and mass balance (e.g. calving and basal melting driven by ocean forcings), which in turn impacts the overall mass of an ice sheet.

Previous studies have demonstrated that the presence of multiple pinning points along an ice shelf can affect the dynamics of a whole ice shelf, as well as the flow of upstream grounded ice. Both large- and small-amplitude pinning points create longitudinal resistance, or buttressing (Hindmarsh, 2006; Schoof, 2007; Berger et al., 2016; Favier et al., 2016). Small-amplitude irregularities have been shown to influence the modelled dynamics of the ice on a large-scale (Berger et al., 2016; Pritchard et al., 2012). Studies by Jenkins et al. (2010) and Gladstone et al. (2012) show that the un-grounding of an ice rumple in the Pine Island Glacier contributed to the retreat that is still ongoing in the Amundsen Sea Embayment. Work by Fürst et al. (2015) and Berger et al. (2016) show that the ice shelf and ice shelf calving front respond differently to different types of pinning points. The extensional strain downstream of the pinning points, close to the calving front, gives rise to fractures and crevasses. These deformations cause enhanced flow of ice (Golledge et al., 2012) and impact the stability of the ice shelf (Matsuoka et al., 2015).

The bathymetry under the AIS is sparsely observed with few direct observations over the southern-most region, south of $\sim 71.6\ ^\circ$ S (Galton-Fenzi et al., 2008; Fricker et al., 2009). A previous modelling study by Galton-Fenzi et al. (2008) on the shape of the sub-ice shelf cavity under the AIS, extending south of this latitude, shows a sensitivity of the modelled rates of melting and freezing to the adopted bathymetry. Ocean circulation was found to follow the contours of the sub-ice shelf cavity under the AIS, allowing the warmer water above the pressure-melting point to erode the ice at the grounding line. Improved mapping of the AIS led to a major southward shift of the estimated grounding line position (Fricker et al., 2002b), improving the understanding of the ice dynamics of the AIS.

Along the AIS are large-scale ice rises (such as massifs, islands, and nunataks) that pierce through the ice shelf. These are visible in satellite imagery, either directly or through patterns of ice flow velocities (Rignot et al., 2011). Small-scale pinning points are harder to observe, and if remote sensing measurements are not spaced closely enough to each other, they will either partially or fully miss small-amplitude topographic irregularities in location, height, and diameter. Matsuoka et al. (2015), however, address this challenge and construct a data set of small-scale pinning points determined by combination of observations of elevated surface, the presence of surface crevasses, deviations in ice flow, and strain/velocity maps form synthetic aperture radar (SAR) interferometry to give the best possible chance of observing small features. In this study, the location of pinning points are extracted from Matsuoka et al. (2015) and include grounding zone points derived from synthetic aperture radar interferometry (Rignot et al., 2011) with laser altimetry from ICESat (Fricker et al., 2009; Brunt et al., 2010) and new additional island outlines from the MODIS Mosaic of Antarctica survey from 2009. High-resolution Landsat Image Mosaic of Antarctica data (Bindschadler et al., 2008), and IPY-MEaSUREs Antarctica velocity map data Rignot et al. (2011) was used to enable visually guided manual editing of the pinning points to better represent their exact extent.

Sun et al. (2014) explore the sensitivity of the AIS catchment to random noise added to the BEDMAP2 bathymetry data set (Fretwell et al., 2013) and find that the AIS model is sensitive to the amplitude of the added noise. However, their study explores the impact of variations in the region of grounded ice only. The sensitivity of the system to pinning points beneath the floating ice shelf is not included. While independent numerical studies of the AIS have investigated the response of the AIS model to either sub-shelf cavity geometry, grounding line position (Galton-Fenzi et al., 2008), or synthetic noise added to BEDMAP2 (Sun et al., 2014), there has been no comprehensive sensitivity study to examine which of the available bathymetry data sets would be best suited as a boundary input in ice sheet models. An under-sampled bathymetry can cause a large bias in modelled ice volume change as investigated in a continent-wide study (Gasson et al., 2015). A study examining the response of the Pine Island glacier in West Antarctica showed the ice volume to decrease by up to 25% if the boundary condition (bathymetry) needed for the ice sheet model is not well constrained (Durand et al., 2011).

We examine the effect of different published bathymetries on ice sheet model results for the AIS, including the addition of two pinning points close to the calving front, which are not included in most geometry datasets e.g. BEDMAP2. The aim of this study is to assess the impact of uncertainties in bathymetry on modelled ice sheet extent, to isolate bathymetric features that cause discrepancies between modelled and geomorphological field observations, and to identify the bathymetry that produces a modelled steady state most comparable to the present day configuration. In this contribution, we (i) investigate the response of the LAGS model to four available bathymetry data sets, (ii) determine the causes of mismatch of model outputs to observed ice shelf geometry, (iii) model the response of the Amery ice front (AIF) to pinning points at the calving front, and (iv) identify the optimum tuning of calving parameters. We use a numerical ice sheet model, and assess results based on discrepancies between modelled and observed measurements of ice thickness, upper surface ice velocity, and ice flow direction.

2.2 Methods and Data

2.2.1 *Parallel Ice Sheet Model*

The Parallel Ice Sheet Model (PISM: User's Manual available at www.pism-docs.org) Version 0.7.3 (Bueler et al., 2007; Bueler and Brown, 2009; Winkelmann et al., 2011; Martin et al., 2011) is a 3D, whole continent, thermomechanically-coupled hybrid model, i.e. the shallow ice approximation (SIA) and shallow shelf approximation (SSA) are superposed. SIA dominates in grounded ice with a non-sliding base, while SSA dominates in ice shelves and ice streams on grounded ice. SIA and SSA horizontal velocities are computed in the whole continental domain, where transition from one to another is calculated by a weighting function for a continuous smooth transition from SIA across the grounding line to SSA (Bueler and Brown, 2009).

The ice rheology is given by the Glen-Paterson-Budd-Lliboutry-Duval flow law (Paterson and Budd, 1982; Aschwanden et al., 2013; Lliboutry and Duval, 1985). PISM employs an enthalpy-based energy conservation scheme (Aschwanden et al., 2012) where ice flow is coupled to the temperature of the ice. The annual mean surface temperature, RACMO2.3/ANT27 for year 1979-2014 (Van Wessem et al., 2014), and geothermal heat flux (An et al., 2015) are provided as boundary conditions for the advection and vertical conduction of heat through the grounded ice layers, while pressure melting temperature is also needed in the case of ice shelves as a boundary condition (Winkelmann et al., 2011).

The bedrock is regarded as rigid, impenetrable, and parallel to basal shear stress, and basal sliding velocity. A pseudo-plastic power law relates basal shear stress and velocity at the ice-bed interface, and a quotient in the pseudo-plastic sliding law (q) is used to control the basal strength assuming that there is a layer of till underlying the grounded ice (Winkelmann et al., 2011; Bueler and Brown, 2009). The spatial location of ice streams is calculated from the yield stress, which is dependent on a subglacial hydrology model (Aschwanden et al., 2012, 2016), and the modelled till strength, which is a function of bed elevation (Martin et al., 2011; Winkelmann et al., 2011; Aschwanden et al., 2016). We use a default hydrology model where water is not conserved but it is stored locally in the till up to 2 m column height, and any amount higher than this maximum value is lost with no feedback. The stress boundary condition at the calving front is calculated from the mass continuity equation and the geometry. Horizontal strain rates are used to calculate the caving rate (Levermann et al., 2012) in combination with a prescribed minimum ice thickness of the ice front.

The surface mass balance is computed from input data of precipitation and near-surface air temperature (RACMO2.3/ANT27, year 1979-2014 (Van Wessem et al., 2014)). The air temperature is used to calculate the energy available to melt ice at the ice surface interface by employing a positive degree-day (PDD) model (Aschwanden et al., 2013; Seguinot et al., 2014). PDD is defined as the integral of temperatures above 0 ° C in one year, which in our case is between 0.37 K and 8.36 K. The lapse rate (8.0 K km^{-1}) applied to the 2 m (above surface) air temperature forcings serves as the boundary condition for the conservation of energy equation, which corrects the differences between the fixed surface ice elevation and the time evolving modelled elevation (Aschwanden et al., 2013; Seguinot et al., 2014). The ice shelf basal melt rate is controlled by the ocean's potential temperature (271.3 K) and salinity of the adjacent ocean (27.0 g/kg) which were used to initialise basal melt at the ice-ocean boundary layer (Holland and Jenkins, 1999).

PISM has multiple choices for parameters that control ice flow, ice softness, sliding, and calving of ice front that affect ice dynamics of grounded ice and floating shelf (https://pism-docs.org/wiki/doku.php). The steady state solution was found using six optimised variables (pers. comm. Steven Phipps, 2019): sia_e, ssa_e, q, till, K, and thk (Table 2.1). By generating a 50 member Latin hypercube (Santner et al., 2003, details in Chapter 1), these were selected to produce a steady state that deviates as little as possible from present day conditions of ice thickness, ice extent, and velocity. Simulations were first carried out at coarse resolution, 10 km horizontal resolution, where the computational domain has a maximum height of 6000 m with 21 vertical layers of ice thickness in the positive z-axis ranging from 71.87 m to 428.12 m depending on the local ice thickness. At finer grid, 5 km horizontal resolution, the height of the computational domain was set at 5000 m. The geometry of the domain is given by ice thickness and bedrock elevation data, which are described in full detail in Section 2.3.1 for each sensitivity experiment.

2.2.2 *Spin-up*

The boundary conditions that were used as inputs in a three-stage spin-up procedure at 10 km horizontal resolution were taken from present day climatology data as described in Section 2.2.1. Further boundary conditions relate to the bathymetry, and are described in the following text of Section 2.3.1 (Galton-Fenzi et al., 2008; Timmermann et al., 2010; Fretwell et al., 2013; Van Wessem et al., 2014; An et al., 2015). Simulations at coarse resolution do not resolve ice dynamics well, but enable multiple simulations to be run within reasonable computational time and resources. For the first stage, the present day climatology data were read in and the resolution of the simulation was specified. In the first and second stages, only the SIA stress was applied, with a 1 year and 100 year simulation respectively for each stage. In the second stage, the stress peaks arising from ice surface roughness were smoothed according to the default procedure within PISM. The output of this stage acted as input data for the next stage, where the geometry was held fixed and the thermal state of the ice mass was evolved in a 250,000 year run. In the last stage, the full physics of the model was applied, such as the parameters that govern the dynamics of ice, hydrology, basal sliding, and calving at the ice front. In this stage the geometry was allowed to evolve freely until it reached a steady state in terms of total ice volume, which occurred after 40,000 years (Bueler and Brown, 2009; Pittard, 2016).

Parameter	Value	Description
sia_e (unitless)	2.7	Enhancement factor for grounded ice where vertical shear dominates.
ssa_e (unitless)	1.8	Enhancement factor for floating ice where horizontal shear dominates.
q (unitless)	0.8	Exponent in the pseudo-plastic flow law.
till (unitless)	0.01	A tuning parameter of the effective pressure of ice against pressurised water in the till.
ϕ (unitless)	10.0, 25.9, -760.0, 1279.0	Tuning of till strength depending on bed elevation. It varies the strength of the basal resistance by setting till friction angle as a function of bed elevation, i.e at -760 m bedrock depth till angle is 10.0°, and when bedrock depth goes to 1279 m, till angle is 25.9°
K (m s)	2.0e+16	Constant relating calving rate to principal strain rates (Levermann et al., 2012).
thk (m)	230.0	Sets a thickness limit where ice below this thickness is calved from the ice front of an ice shelf

Table 2.1: Parameter choices

2.3 Experiments

We undertook three investigations in this study, two were sensitivity experiments (bathymetry and pinning points) while the third was the further tuning of calving parameters.

2.3.1 *Experimental design: Sensitivity to bathymetry*

We investigated the sensitivity of the LAGS to four different bathymetry data sets described below. Geometries 1,2 and 4 are widely used as boundary conditions for numerical modelling, either for the whole Antarctic continent or regional studies. Geometry 2 is specifically tailored to the AIS region. Each bathymetry was run through the multi-stage spin-up process at 10 km resolution to achieve a steady state. A summary of the imposed bathymetry geometries is described below.

- ***Geometry 1*** **:** The unmodified topography, bathymetry and ice thickness from BEDMAP2 (Fretwell et al., 2013), Figure 2.2(a).
- ***Geometry 2*****:** The bedrock elevation underneath grounded ice from BEDMAP2 was stitched to ocean-floor bathymetry from RTopo-1 (Timmermann et al. (2010)), which includes the shape of the sub-ice shelf cavity underneath the AIS developed by Galton-Fenzi et al. (2008) and used by Pittard (2016), Figure 2.2(b) and (e). To reduce steep gradients at the abrupt transition between the two data sets, linear smoothing was applied through a convolution affecting only neighbouring grid points on the BEDMAP2 bedrock data set, leaving the bathymetry bed elevation untouched, Figure 2.2(f). BEDMAP2 was used for the ice thickness.
- ***Geometry 3*****:** The bathymetry and ice thickness were taken from BedMachine (Morlighem et al., 2019), which uses the bathymetry from the International Bathymetric Chart of the Southern Ocean (IBCSO), Version 1 (Arndt et al., 2013) along with the bathymetry from Galton-Fenzi et al. (2008) for the sub-ice shelf cavity underneath the AIS, Figure 2.2(c). The ice thickness was computed from mass conservation along the edge of the ice sheet, which was interpolated to the interior ice sheet by kriging.
- ***Geometry 4*****:** Ice thickness and bathymetry were taken from RTopo-2 (Schaffer et al., 2016). North of 61.5° S, RTopo-2 uses the General Bathymetric Chart of the Oceans grid, GEBCO_2014 (Weatherall et al., 2015), and bathymetry of the sub-ice cavities for the Southern Ocean are taken from IBCSO Version 1 (Arndt et al., 2013). RTopo-2 uses ice thickness and topography underneath the grounded ice from BEDMAP2, stitched to the IBSCO bathymetry data within the sub-ice cavity zone, 10 km downstream of the grounding line, Figure 2.2(d).

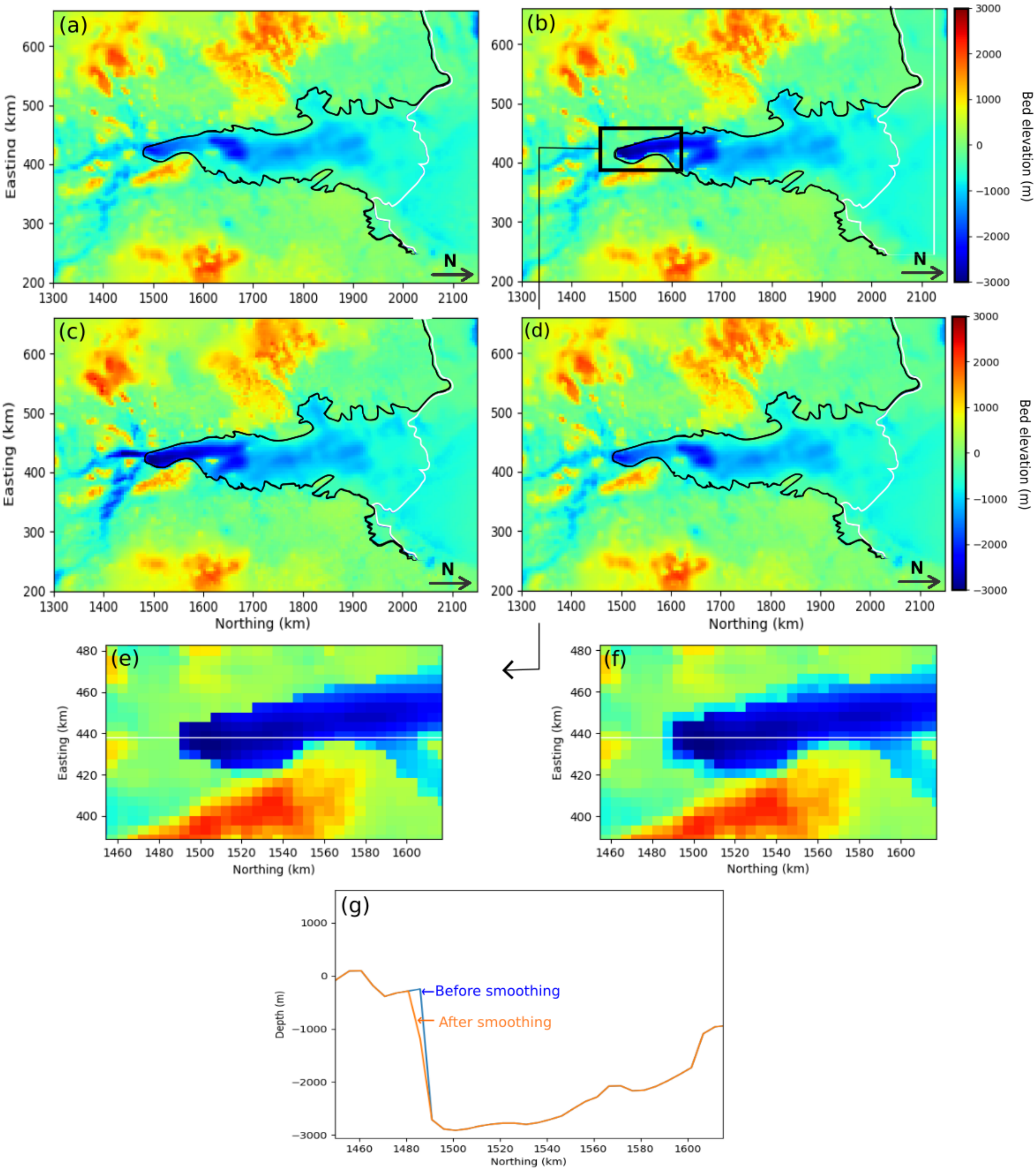

Figure 2.2: Bathymetry data sets: (a) Geometry 1: BEDMAP2, (b) Geometry 2: BEDMAP2 and RTopo-1, (c) Geometry 3: Bedmachine and Galton-Fenzi, and (d) Geometry 4: RTopo-2. (e) and (f) show detail of Geometry 2 at the grounding line, before and after smoothing was applied. The white solid line in (e) and (f) is where the cross section is shown in (g). References to datasets are given in text. All of the bathymetry geometries are sub-sampled to a 5 km regular grid. The colour scales for this figure, and the two following figures, are chosen for comparison to previously published results.

2.3.2 *Experimental design: Sensitivity to pinning points*

The second experiment set focused specifically on exploring the effects of including pinning points on the modelled flow of the AIS, particularly the two pinning points Podlednyj holm and Triangle, identified by Matsuoka et al. (2015) and shown in Figure 2.3a. The precise dimensions and location of these pinning points are uncertain (pers. comm. Galton-Fenzi, 2019; (Matsuoka et al., 2015)), therefore we postulated a range of different dimensions with reference to Matsuoka et al. (2015) to cover the potential extent of their spatial dimensions (Table 2.2). These were superimposed on Geometry 2. Geometry and thermal field variables from the Geometry 2 steady state were regridded to a 5 km horizontal resolution using PISM functionality (bilinear interpolator). The change in grid size required a further spin-up procedure, and the relaxation to steady state occurred after 38,000 years. The experiments firstly used a diagnostic simulation, followed by a prognostic simulation.

- ***Diagnositic***: Simulations from Cases I – V (Table 2.2) were carried out at 5 km horizontal resolution. These simulations tested PISM sensitivity to small changes in geometry.
- ***Prognostic***: Geometry Case IV was simulated over a 1700 year long runtime at 5 km horizontal resolution to assess the effect of the pinning points on the evolution of the LAGS.

2.3.3 *Experimental design: Tuning of calving parameters*

In PISM there are four calving models, of which two are employed in this study: 1) The physically-based 2D "eigencalving" parameterisation that implements a parameter 'K' relating calving rate to principal strain rates, and 2) a thickness threshold at the ice front. Both of these calving models were implemented simultaneously.

The steady state geometry from Case IV (Table 2.2) was the initial modelled state for investigating a range of values of the proportionality constant (K) and thickness threshold (Hcr) at the ice front, to determine the closest match to the observed calving front location (see Table 2.3). This experiment was designed to determine if the inclusion of pinning points in the geometry improved the model's ability to match the observed calving front location.

- ***Eigencalving*** : This model uses a constant K to derive the average calving rate from principal strain rates:

$$c = K\dot{e}_{+}\dot{e}_{-} \tag{2.1}$$

where 'c' is the average calving rate (m year^{-1}), and $\dot{e}_{\pm}$ are the principal strain rates (sec^{-1}) in two principal horizontal directions on ice shelves (Levermann et al., 2012).

Identifier	Description of perturbations
Case I	The synthetic pinning points were of the same height as stated in the inventory provided by Matsuoka et al. (2015), and filled one grid cell at 5 km resolution and they make no contact with the base of the ice shelf, Figure 2.3(a).
Case II	Same as Case I but the height of the pinning points, Podlednyj holm and Triangle, were increased by 20 m to make more grid points contact the base of the ice shelf, Figure 2.3(b).
Case III	Same as Case I, but both width and height of Podednyj holm and Triangle were modified. The width was extended to accommodate neighbouring grid cells, and the heights of the pinning points were elevated by 40 m. The grid cell (denoted by 'X') though elevated by an additional 40 m, was not high enough to make contact with the base of the ice shelf and therefore didn't fully represent the predicted extent of the pinning points, Figure 2.3(c).
Case IV	Same as Case III, but all the pinning points, including the grid cell denoted by 'X', depicted in Figure 2.3(d), make contact with the base of the ice shelf.
Case V	Control case, bathymetry as for Geometry 2, with subdued bathymetry (no pinning points in contact with the base of the ice shelf), refined to 5 km horizontal resolution, Figure 2.3(e).

Table 2.2: Synthetic pinning points generated for the Amery Ice Shelf. See also Figure 2.3.

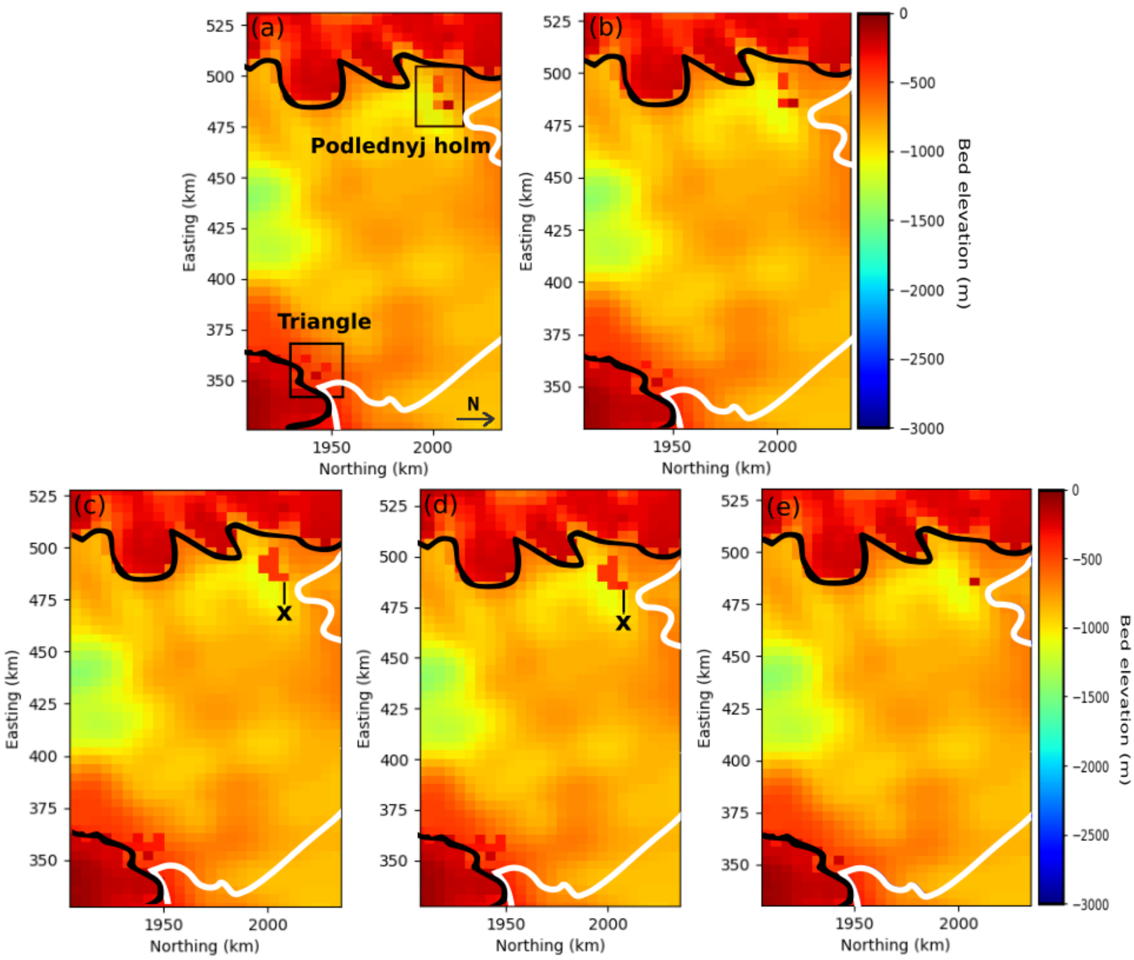

Figure 2.3: Figures (a-e) correspond to Cases I–V respectively, as described in Table 2.2. Podlednyj holm and Triangle are the additional pinning points added to our Geometry 2 bathymetry based on a glaciological study by Matsuoka et al. (2015). (a) shows both spatial and elevation coverage as stated in the inventory from Matsuoka et al. (2015), the other figures are varying geometries of these pinning points, which represent a range of possible extents and heights of the pinning points. The annotation 'X' in Figures (c) and (d) shows one grid cell at 5 km resolution: in (c) the height of 'X' has no contact with the AIS, while in (d) 'X' touches the underside of the AIS, causing basal drag. The grounding line location (black line) and the present day ice front (white line) are shown as an overlay.

The range of values were informed by a previous study by Pittard (2016) and a whole Antarctic continent simulation at 15 km resolution (pers. comm. Steven Phipps, 2019).

- ***Thickness threshold*** **:** This model sets a minimum ice thickness (Hcr) at the calving front. A range of values were tested, based on observed ice thickness at the calving front from BEDMAP2 (Figure 2.4a).

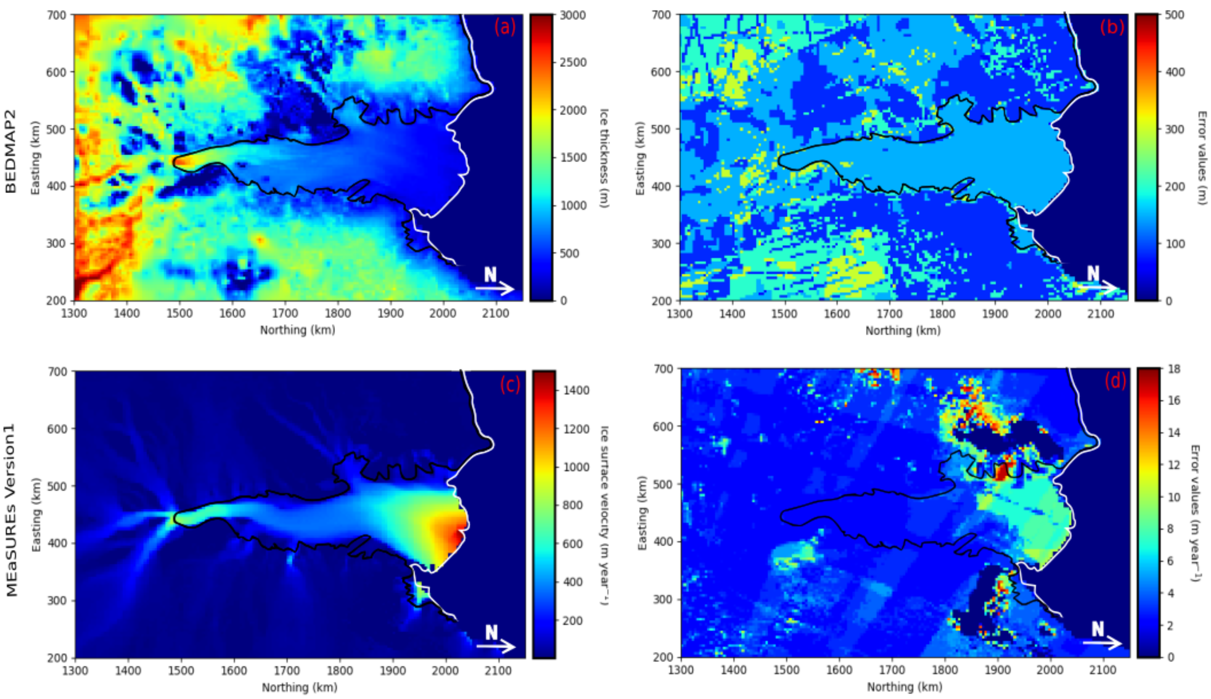

Figure 2.4: Observational data for AIS (a) BEDMAP2 ice thickness and ice shelf extent, (b) estimated error in ice thickness measurements, (c) annual Antarctic ice velocity from 2005–2017 (Rignot et al., 2011), (d) estimated error in ice velocity. Again, the colour scale reflects previous presentation of these data.

2.4 Results and Discussion

The main focus of the current study is the sensitivity of LAGS to variations in the geometry of bathymetry and pinning points used, related technical questions relating to the choice of calving parameters are also addressed. The differences between the observed and simulated grounding line, ice shelf front position, ice thickness and upper surface ice velocity were used as evaluation criteria. The observed present-day values used for this comparison were taken from BEDMAP2 (Fretwell et al., 2013) and MEaSUREs Annual Antarctic Ice Velocity (Version 1, Rignot et al., 2011, Figure 2.4).

2.4.1 *Sensitivity to bathymetry*

We present the response of the LAGS to the four different bathymetry geometries previously described (Section 2.3.1, Figure 2.2). This results are summarised in Figure 2.5 and Figure 2.6 by showing a comparison of observed and modelled extent of the evaluation criteria for the LAGS at steady state for each of the different bathymetry geometries.

Figure 2.5 shows the modelled grounding line and calving front position of the AIS obtained at steady state from each simulated bathymetry. Both Geometry 1 (Figure 2.5a) and Geometry 4 (Figure 2.5d) show a similar configuration whereby the southern-most part of the grounding line has advanced from the known grounding line position downstream to Clemence Massif, as

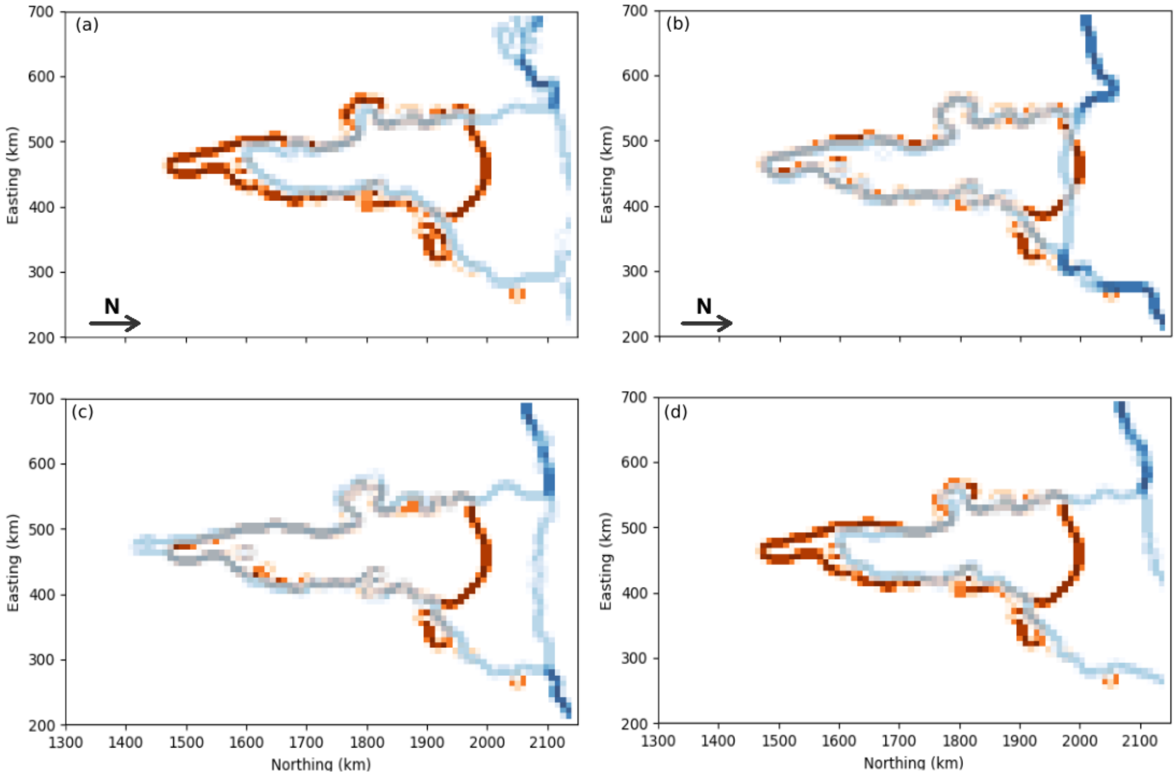

Figure 2.5: Comparison of the grounding line and calving front position between observed BEDMAP2 (red outline) and modelled results (blue outline) at steady state in a 10 km horizontal resolution simulation. (a) Geometry 1 (BEDMAP2), (b) Geometry 2 (BEDMAP2 and RTopo-2), (c) Geometry 3 (BedMachine), and (d) Geometry 4 (RTopo-2). Overlapping observed and modelled grounding lines appear as grey. Coastline overlapping with ice edge shows as dark blue.

shown in Figure 2.5 (red outline), and the direction of the southern-most tip of the grounding line points to the west. In both simulations the calving front is predicted to advance significantly from the present day position. Geometry 2 produces an advanced calving front in the east, but the grounding line remains similar to BEDMAP2 at 10 km resolution (Figure 2.5b), whereas Geometry 3 shows a retreated grounding line with an advanced calving front (Figure 2.5c).

A further comparison between the modelled results and present-day observations for ice thickness, ice shelf extent, and upper surface ice velocity may be made through examining Figure 2.6. The predicted steady state ice thicknesses of both Geometry 1 and Geometry 4 (Figure 2.6a, 2.6d) are significantly higher than observed values where the Lambert, Mellor, and Fisher glaciers join to feed the AIS. As for the velocity, Figure 2.6e, 2.6h, both demonstrate notable misfits. The similarity between modelled results from Geometry 1 and Geometry 4 is caused by the similarity of the bathymetric data sets BEDMAP2 and RTopo-2 up to the point 10 km downstream of the grounding line (Figure 2.7).

The results imply that both BEDMAP2 and RTopo-2 bathymetric data are unsuitable as boundary conditions for the LAGS with the adopted model setup. Their modelled steady states

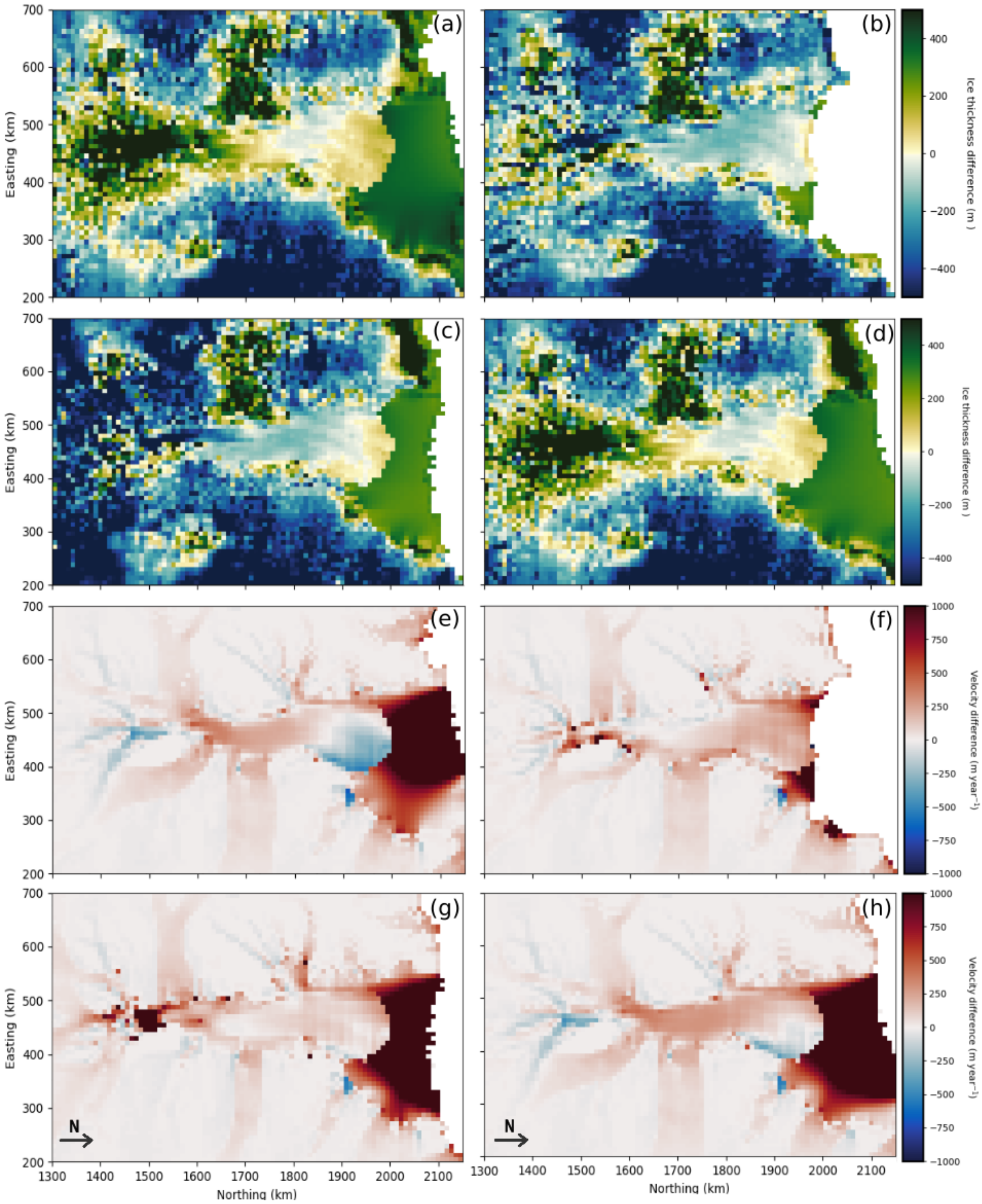

Figure 2.6: Top panel: Differences between modelled ice thickness and observed ice thickness from BEDMAP2 for (a) Geometry 1, (b) Geometry 2, (c) Geometry 3, (d) Geometry 4. Bottom panel: Difference between modelled surface ice velocity and observed velocity (Rignot et al., 2011) for (e) Geometry 1, (f) Geometry 2, (g) Geometry 3, (h) Geometry 4. Differences are taken as modelled minus observed. Both BEDMAP2 and Rignot et al. (2011) data do not extend beyond the present day ice front, hence the the ice thickness and ice velocity beyond the ice front are solely from the modelled states of each geometry. The colour scale for this figure, and subsequent figures, is perceptually-uniform and chosen with current good practice in graphics in mind.

differ significantly from the present day LAGS configuration. The model outputs for Geometries 1 and 4 also show advancement of the grounding line downstream to where Clemence Massif is located (Figure 2.8). This is caused by the shallow bed elevation being less than the ice draft near the grounding line, consequently generating a shallow ocean cavity, in these data sets. The shallow bathymetry results in higher modelled elevation of grounded ice at the glacier confluence, and this consequently leads to much advanced calving fronts when using Geometries 1 and 4.

The model outputs produced by Geometry 2 show a comparable grounding line and calving front position to observations (Figure 2.5b). The ice thickness and ice velocity, however, deviate from observations at the grounding line and at the calving front. The modelled ice shelf front is further advanced than the observed calving front in the east, which is where the ice shelf front of the AIS combines with the Publications Ice Shelf (Figure 2.1). The modelled ice shelf front is slightly retreated from the observed position at the ice front centre, and the western side of the ice shelf is modelled to be approximately close to the present day location (Figure 2.6b). The misfit in ice velocity south-east of the grounding line was caused by the abrupt drop in the bedrock topography as described above in Section 2.3.1. This steep bedrock gradient also generated misfits in ice thickness compared to BEDMAP2 (Figure 2.6b). The difference in velocity, Figure 2.6f, shows misfits at the south of the AIS across the grounding line and at the calving front. At coarse resolution, the variable that causes this misfit is uncertain. Therefore, in the next section this geometry will be further simulated at finer resolution.

The Geometry 3 results show a retreated grounding line with an advanced calving front (Figure 2.5c), which leads to thinner ice at the south part of the grounding line (Figure 2.6c). Because of the deeper trough in Geometry 3 (Figure 2.2c), the modelled ice thickness is lower than given in BEDMAP2. The deep trough extends towards the Lambert and Mellor Glaciers (Figure 2.1), which may have caused the predicted faster ice flow in this area, due to increased basal sliding probably related to the steep gradients (Figure 2.6g).

The results for Geometry 3, based on the Bedmachine database (Morlighem et al., 2019), suggest that this bathymetry is a better choice than G1 and G4 for modelling the AIS. In terms of the research presented in this thesis, the results for this bathymetry suggest that more detailed modelling would require a repeat of the optimisation of variables that was undertaken for continental-scale modelling (Steven Phipps, pers. comm, 2019) on which these experiments are based.

Of the four geometries tested, the simulation using Geometry 2 produces the best match to the observed grounding line location, and shows smaller misfits in ice thickness and ice velocity than the other employed bathymetries. This was therefore taken forward with a finer grid (5 km resolution) to be used as the bathymetry boundary condition (Figure 2.8) for the pinning

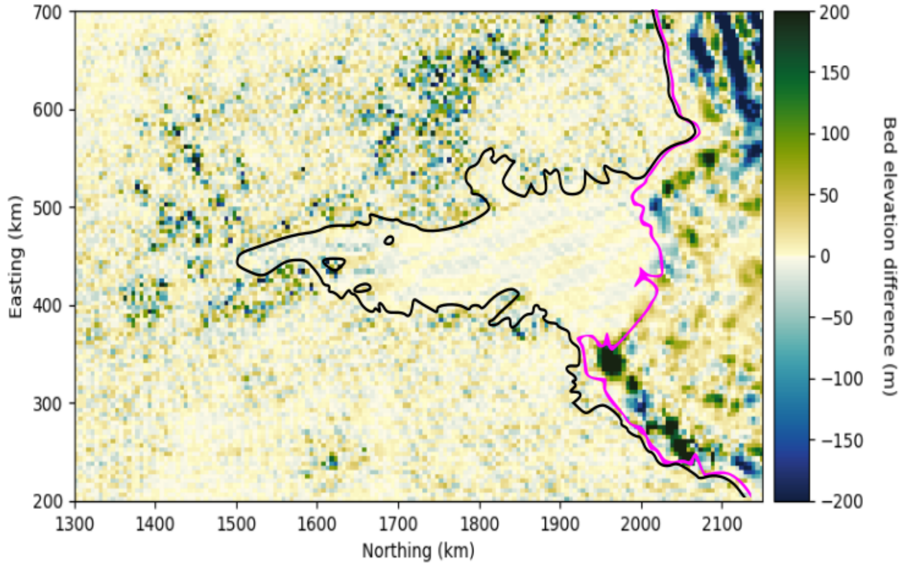

Figure 2.7: Difference between Geometry 1 (BEDMAP2) and Geometry 4 (RTopo-2) in bed elevation over the whole LAGS region. Misfits are small as both data sets use the bed elevation from Fretwell et al. (2013) under grounded ice. There are higher magnitudes of difference for the bathymetry in the open ocean since RTopo-2 uses the International Bathymetric Chart of the Southern Ocean (IBCSO) Version 1.0 (Schaffer et al., 2016), while BEDMAP2 uses GEBCO 2008, augmented by several other publicly available data sets (Fretwell et al., 2013). In general, while the RTopo-2 dataset was a forward development in comparison to RTopo-1, the area offshore from the AIS did not improve and using RTopo-1 (as used in Geometries 1 and 2) for this area remains a good choice.

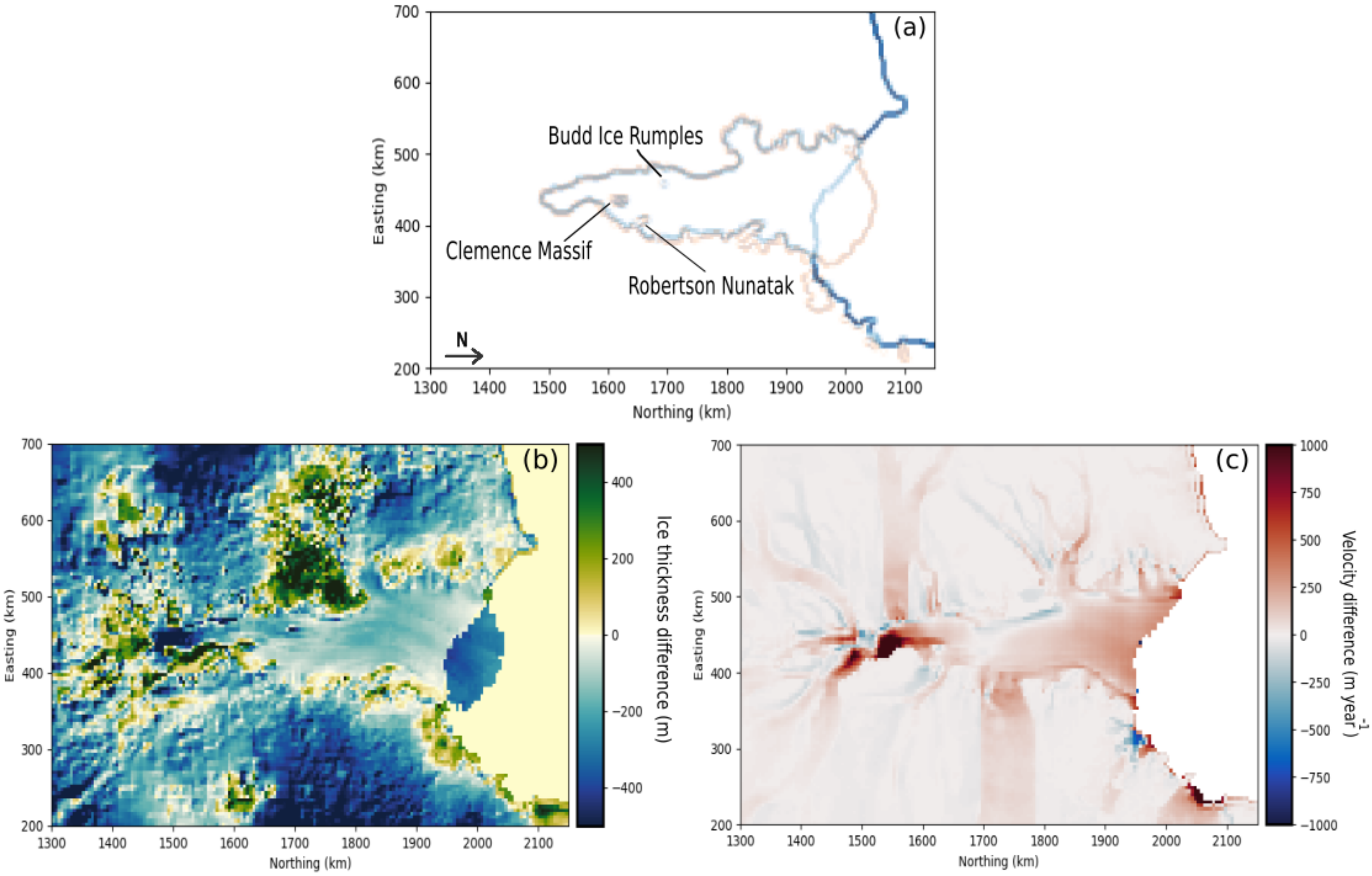

Figure 2.8: Steady state of Geometry 2 at 5 km horizontal resolution. (a) Comparison of the grounding line and calving front position between observed BEDMAP2 (pale red outline) and modelled results (pale blue outline) at steady state. Overlapping red and blue shows as grey. Coastline overlapping with ice edge shows as dark blue. (b) Ice thickness difference between the modelled steady state and BEDMAP2, and (c) Surface ice velocity difference between the modelled steady state and observations by Rignot et al. (2011).

point and calving parameter experiments. At 5 km horizontal resolution, large pinning points already present in the Geometry 2 bathymetry such as Clemence Massif, Robertson Nunatak, and Budd Ice Rumples are more pronounced than at 10 km resolution. After the spin-up to find the steady-state condition at 5 km resolution, there were no dramatic changes between the 10 km results and 5 km results in grounding line position in the southern part of the AIS relating to the increase in resolution (Figure 2.8a). In terms of the details of ice sheet response in the new steady state, the modelled grounding line on the eastern part of the ice shelf front advanced somewhat, but the calving front retreated. The misfits between the 5 km resolution modelling results and observations of ice thickness and ice velocity to the south east of the grounding line now show more clearly, as intense colours in the vicinity of the Clemence Massif, the effect of steep gradients where our two bedrock data sets join (Figure 2.8b, 2.8c). These misfits are addressed in subsequent sections, firstly by incorporating pinning points due to their strong influence on ice dynamics, and lastly by exploring calving parameters.

Comparison with other studies

A direct comparison of our results with related studies is limited because, to the authors' knowledge, relatively few similar studies have been performed for the LAGS. Sun et al. (2014) investigated the perturbation of bedrock for ice shelves including the AIS by adding low- and high- frequency noise patterns to the ice shelf bathymetry of the BEDMAP2 data set. They found that the ice sheet model of the LAGS (in BISICLES) was more sensitive to low frequency perturations of small amplitude than high frequency perturbations. This study used a simple model set up, and climate forcings, and the modelled state was not tuned to the LAGS present day flux. The simulations presented in our study start from a pre-computed steady state that is close to the present day dynamical state of the LAGS and AIS, and the results produced by adopting pinning points demonstrate that the AIS, and consequently LAGS, are sensitive to both the amplitude and extent of the synthetic pinning points (Figure 2.9 and Figure 2.11).

Investigations focused on other regions of Antarctica such as Pine Island Bay have found, in accord with the present study, that bathymetry features in the coastal region have a significant influence compared to those inland (Durand et al., 2011). The latter study is significant in that a full-Stokes finite element code was employed, and our study using the PISM (hybrid SIA-SSA) model produced similar results. In a more general PISM simulation of the response of an Antarctic-like continent-wide ice sheet since the last-glacial maximum, Bart et al. (2016) found that the bathymetry of the continental shelf, shallow or overdeepened, influenced the response to longer-scale climate forcings. A wide ranging review by Colleoni et al. (2018) noted the importance of high-resolution sub-ice shelf and continental shelf bathymetry as a priority to support ice sheet modelling, which is in accord with the findings of the present study.

2.4.2 *Sensitivity to pinning points*

To investigate the effect of pinning points on modelled ice shelf dynamics, we synthetically added two pinning points at locations near the calving front – Podlednyj holm and Triangle (Matsuoka et al., 2015) – to Geometry 2. We examine their influence on the modelled calving front position, ice thickness, and upper surface ice velocity. Since the precise dimensions of the pinning points are not well known, varying dimensions were adopted that would cover their potential range in elevation and width (Table 2.2, Figure 2.3) across five test cases (Cases I-V, with Case V being the control case with no change from Geometry 2). Firstly, diagnostic (i.e. non- time evolving) simulations were performed for all cases of the Podlednyj holm and Triangle pinning points to test the sensitivity of the modelled velocity to the existence of these pinning points.

The predicted calving front position (Figure 2.9, first row) to a small extent, and the instantaneous ice velocity to a considerable extent, show the influence of the addition of the pinning points (Figure 2.9, second row). The pinning points show this influence despite being of small scale (one grid cell at 5 km resolution). In Case I, the Podlednyj holm pinning point is the same as in Case V (Geometry 2), as expected there is no change in calving front position on the western side of the ice shelf, but the inclusion of the synthetic Triangle pinning point results in a very slight, instantaneous retreat of the neighbouring calving front (Figure 2.9 first row). In Case II, there are no further changes in the region neighbouring Triangle pinning point, and minimal changes to the calving front neighbouring Podlednyj holm pinning point. Case III and Case IV result in the same calving front position near to Triangle pinning point, but Case IV shows a slightly advanced calving front on the east side neighbouring Podlednyj holm.

The modelled instantaneous ice velocity presented as the difference between each new geometry and Case V (Geometry 2, control) is shown in Figure 2.9 second row. Case II, with increased pinning point height, results in a decrease in ice velocity in the vicinity of the pinning points. In Cases III to Case IV, where the dimension of synthetic Podlednyj holm is increased in both width and height, and with Case IV pinning point grid cell (marked X) making contact with the base of the ice, the modelled ice shelf velocity behind the ice front decreases in magnitude. In Case II, the additional 20 m added to the bed elevation in the grid cells of Podlednyj holm resulted in a decrease in velocity only where the grid points are located but the velocity at the calving front is still faster than Case V as shown in Figure 2.9 (Case II-Case V). But when the width and height of grid cells were progressively increased, as seen in Case III and Case IV, the velocity starts to decelerate from where the pinning points are located to the calving front, and at the calving front Case V velocity exceeds the modelled velocity from Case III and Case IV. Case II to Case IV indicate the velocity is influenced by both height and width of pinning points (Figure 2.9). This is highlighted between Case III and Case IV since the only difference between them is the height of one grid cell denoted as X in Figure 2.3d. From Figure 2.9 the velocity differences suggest that Case IV generates increased lateral spreading in the calving front neighbouring the Podlednyj holm pinning point. The velocity distribution for Case IV is different to Case III especially within the boxed region shown in Figure 2.9(Case IV-Case V). To better understand the dynamics and influences of the pinning points, a longer simulation (prognostic) was required.

The Case IV simulation, the most successful of the previous tests, was run for 1700 years until it reached steady state at 5 km resolution. The geometry of the Case IV modelled steady state differed significantly from the Geometry 2 modelled steady state. Figure 2.10 shows the difference in grounding line and calving front positions between these two geometries. With the addition of pinning points (Podlednyj holm and Triangle) the model predicts that calving front will be advanced relative to Geometry 2 (Figure 2.11a), resulting in a closer match to

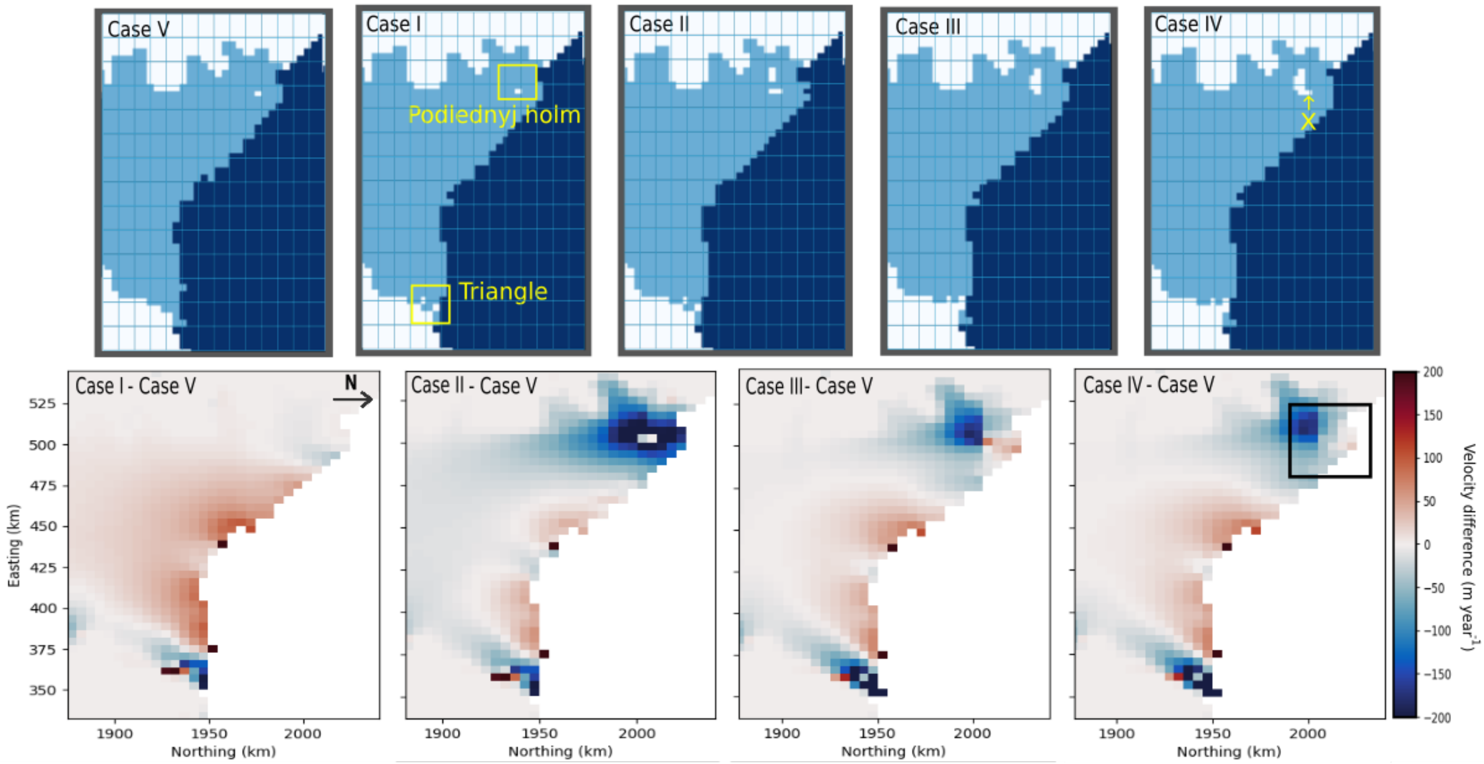

Figure 2.9: First row: the calving front position and pinning point extent resulting from a diagnostic simulation for each case described in Table 2.2. Case I and Case V (control case, same as Geometry 2) are displayed side by side to show the changes between two data sets with the least modification to the dimensions of the pinning points with the grid lines being added to aid visual interpretation (the do not represent model grid cells). Second row: the difference in the instantaneous velocity field caused by the addition of pinning points to the original model geometry (Geometry 2). The modelled surface velocity for Case I, Case II, Case III, and Case IV is compared to Case V, which is the steady state shown in Figure 2.8. Case IV has all grid points of Podlednyj holm in contact with the underside of the AIS, but in Case III one grid point (denoted as 'X' in Figure 2.3(c)) does not have any contact with the AIS.

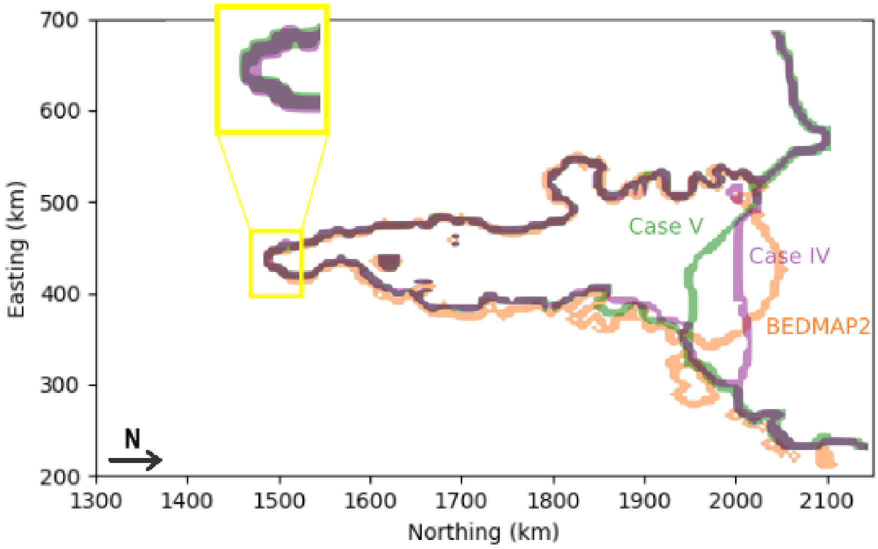

Figure 2.10: Steady state at 5 km resolution of grounding line and calving front positions for Case V (control case, unmodified Geometry 2, green) and Case IV (purple) both at 5 km horizontal resolution in comparison to the observed BEDMAP2 position (pale red). Overlapping lines show as dark grey.

observations, and there was a very small advancement of the grounding line at the southernmost part.

Figure 2.11(a-d) shows the difference between the steady state of Case V (Geometry 2 control) and Case IV. Figure 2.11a shows the ice thickness at the calving front is larger in Case IV than Case V, while Figure 2.11b shows that the velocity at the calving front is lower in Case IV. The percentage change in ice thickness between Case V and Case IV is notable in the south east of AIS the (rectangular box in Figure 2.11c). This location corresponds to the region of misfit that was seen in Figure 2.8. Concentrating on the differences in this location, and averaging over the region enclosed by the box, we find that in Case IV the ice thickness increased by 2.7% and the ice velocity reduced by 43%. The velocities in this region for Case IV (Figure 2.11e) are in closer agreement with observed values (Rignot et al., 2011) than the Case V velocities (Figure 2.11f). Hence, the presence of the pinning points provides buttressing, which slightly increases the ice thickness upstream and reduces its velocity. As the ice velocity decreases, the impact of the abrupt drop lessens within the enclosed box across the grounding line which was ~1700 m for Geometry 2, Figure 2.2b.

The introduced synthetic pinning points are of small topographic scale in comparison to ice rises such as Clemence Massif, which pierces through the AIS. Nonetheless, these pinning points enhance lateral spreading of ice at the calving front (shown by the instantaneous ice velocity result in the diagnostic experiment), and increase buttressing (shown by the slight increase in ice thickness and decrease in ice velocity in the prognostic experiment), which together increase the predicted ice volume of the AIS. There is also a very slight advance of the grounded ice all around the ice shelf. The simulation of the AIS based on Case IV pinning points is, in general, an improved fit in comparison to Case V, however, the configuration of the calving front (Figure 2.11e) could be further improved. This is addressed in the final set of experiments that follow a comparison of the pinning point results with other studies.

Comparison with other studies

Our finding that the AIS can be more accurately modelled by taking into account the presence of pinning points is in agreement with other recent research. In relation to general bathymetry studies, e.g. Durand et al. (2011) as noted in the previous section, accuracy of bathymetry is most important in the coastal region where the interplay between floating and grounding ice is most complex. With regard to studies specifically investigating pinning points, Favier et al. (2012) report that adding a pinning point beneath an ice shelf (full Stokes model) results in a shelf velocity decrease and an advance in the grounding line position. In a further example, Berger et al. (2016) find that an 8.7 km wide pinning point has a significant influence on modelling results (BISICLES) for the Roi Baudouin Ice Shelf (Dronning Maud Land, East Antarctica), and similar results are reported by Favier et al. (2016) for the response of an ice sheet model (BISICLES) to pinning points for several further locations in Dronning Maud Land. In a continent-wide study of Antarctica, Fürst et al. (2015) reach the same conclusion using a full Stokes model (Elmer/Ice), finding that ice velocity modelling can be improved with better understanding of the extent and locations of pinning points, and that such dynamically important features are not present in BEDMAP2. This study also remarks on the implications of ice sheet response to climate forcing that results in the ungrounding of a given ice sheet from its significant pinning points.

2.4.3 *Tuning of calving parameters*

In previous sections we described experiments that tested the bathymetry geometry, and subsequently the added pinning points, that resulted in an improved, but not exact, match to the present day AIS. We now describe experiments that test a range of calving parameters to further refine the modelled calving front location (Table 2.3). Again, the modelled ice front position was validated against the observed position from BEDMAP2. The experiments were performed using the bathymetry with added pinning points as in Case IV through prognostic simulations with the seven different calving parameter combinations given in Table 2.3 (P-I to P-VII).

The bathymetry and pinning point experiments used the P-I calving parameter values, which resulted in an position for the eastern ice shelf front that was slightly too advanced (Figure 2.12, P-I). To address this, in P-II we increased Hcr to 240 m, which led to a position for ice

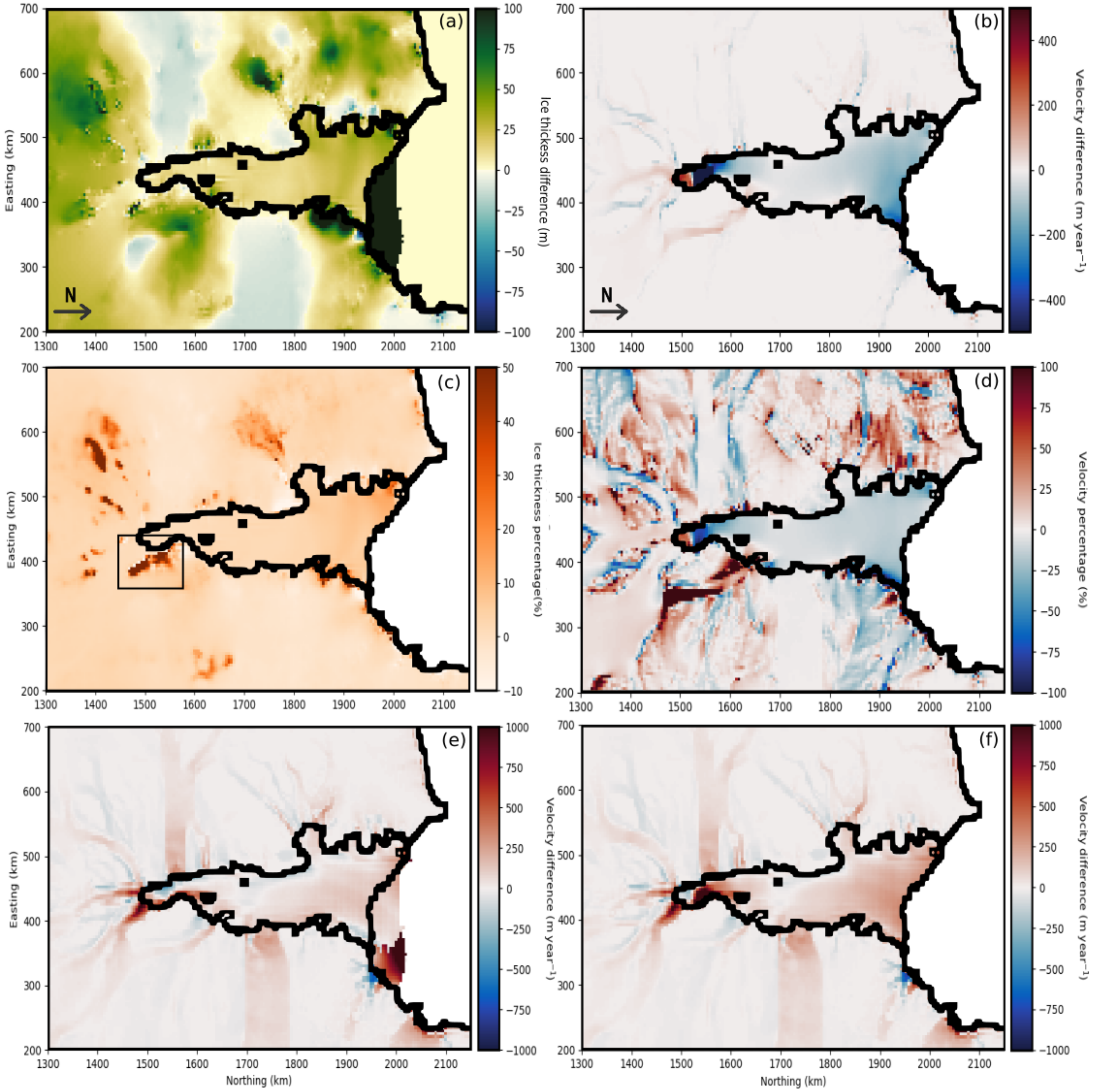

Figure 2.11: Comparison of the steady state of Case IV with Case V (Geometry 2). (a) Ice thickness difference. (b) Ice velocity difference. (c) Percentage change in ice thickness. (d) Percentage change in ice velocity. The small area enclosed within Figure (c) is used to quantify the changes in ice thickness and velocity at the grounding line. (e) Difference in ice velocity between Case IV and Rignot et al. (2011). (f) Difference in ice velocity between Case V and Rignot et al. (2011).

Identifier	Proportionality constant, K (ms)	Thickness threshold Hcr (m)
P-I	2.0e+16	230.0
P-II	2.0e+16	240.0
P-III	2.0e+16	150.0
P-IV	2.0e+15	240.0
P-V	2.0e+15	150.0
P-VI	1.9e+15	240.0
P-VII	1.9e+15	150.0

Table 2.3: Calving parameters combinations used to refine the calving front position.

front that was insufficiently advanced (Figure 2.12, P-II). In simulation P-III, Hcr was changed to 150 m. With such a low thickness threshold we expected to see an advanced ice front, since the AIS calving front is not less than 200 m, but the modelled result for P-III shows an ice front very similar to P-I (Figure 2.12). As the difference in ice thickness at the ice front between P-I and P-III is 80 m, a difference in calving behaviour would be expected. However, the resulting ice fronts for these two models are similar, suggesting that the imposed value of K may have caused strong calving rates (Levermann et al., 2012) that would not allow the ice front to advance. The results of P-I to P-III indicate that the utilised K value is unsuitable for modelling calving of the AIS using our model.

To improve upon the P-I to P-III simulations, we lowered the calving parameter value of K by one order of magnitude (Table 2.3) and performed simulations with Hcr at 240 m and 150 m. With Hcr set at 150 m, the calving front shows an advanced position (Figure 2.12, P-V) in comparison to the result using the calving parameters in P-III, but the match to the coastline in the west (upper part of figure) is lost. With Hcr set to 240 m the resulting model (Figure 2.12, P-IV) shows a calving front closest to the present day AIS configuration. The other two remaining simulations, P-VI and P-VII (Table 2.3), did not provide meaningful results as the ice velocity could not be calculated by the model (incompatible parameter combinations for the geometry). The value of K in the P-IV and P-V simulations indicates a strain rate that allows advance and retreat of the calving front, therefore this value of K (2.0e+15) is selected as the appropriate parameter choice.

The experiments on calving parameter combinations, refining the fit between modelled and observed assessment criteria, inform the interplay between boundary conditions and model parameters in numerical ice sheet modelling. In particular, the importance of bathymetry in the vicinity of the grounding line, and pinning points near the calving front, suggests that

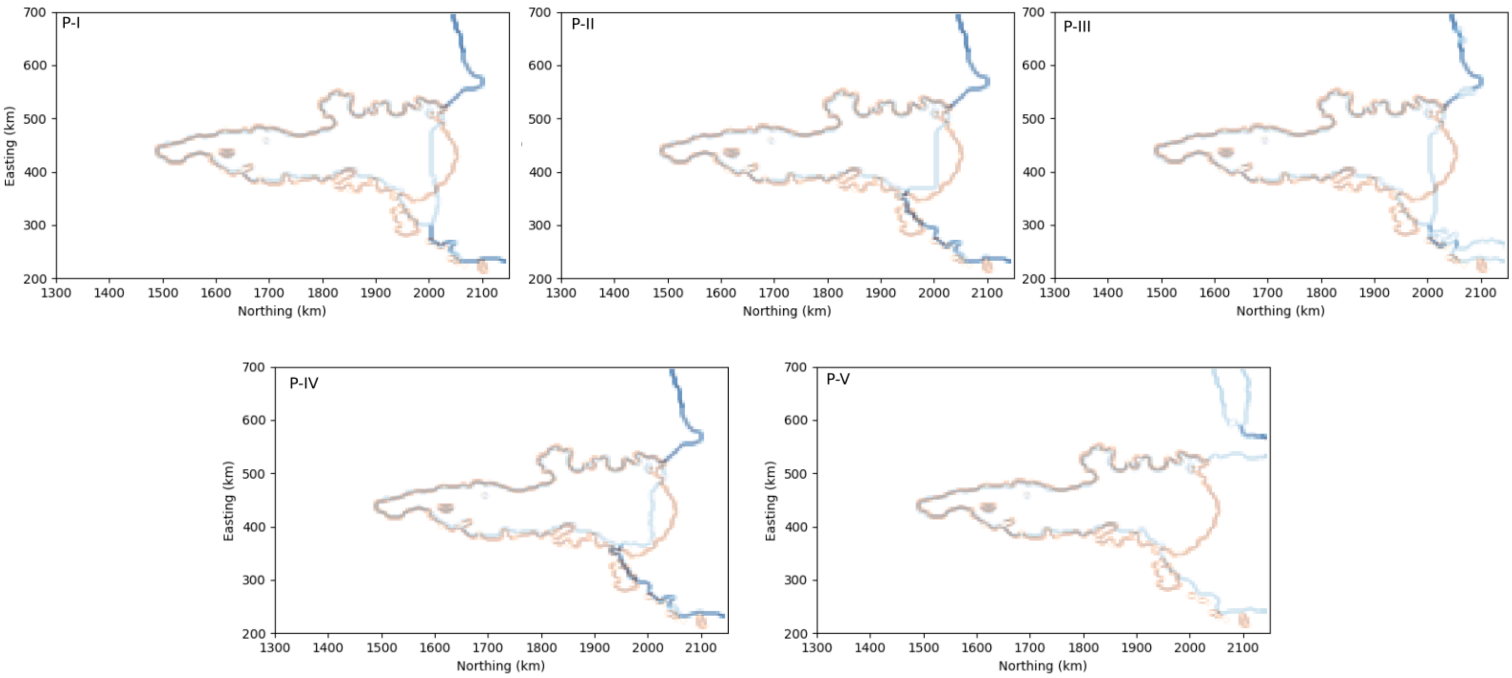

Figure 2.12: Modelled grounding line and calving front (blue) compared to observed location from BEDMAP2 (pale red). These figures show the configuration of the ice front using calving parameters given in Table 2.3. P-I to P-III have same values of K but different values of Hcr (thickness threshold), and P-IV to P-V have different values of Hcr but the same value of K.

tuning calving parameters when a model has under-sampled, low resolution bathymetry could lead to an undue emphasis on poorly constrained model parameters. This would result in high uncertainty in key outputs of ice sheet models, which could propagate into high uncertainty in predictions of, for example, mass loss and sea level rise.

2.4.4 *General Discussion*

Discussion material related to the bathymetry and pinning point experiments is located in the relevant section above. In the paragraphs below, we summarise the limitations of the modelling and present remarks relating to overarching implications of our experiments.

The experiments that we have carried out have been reported with the following limitations in mind: use of an approximate model (PISM), 5 km resolution, and lack of consideration of detailed ocean interactions. With regard to the use of PISM, the comparable findings of other studies using a full Stokes model for other ice shelf systems (Durand et al., 2011; Favier et al., 2012) suggest that the findings of the present study for the AIS (i.e. the use of PISM at 5 km resolution) are, in general, likely to be robust. The chosen resolution was limited by the available computing resource, but care would have to be taken in moving to higher resolution with a hybrid model such as PISM, which may not be the optimum choice for a detailed regional study particularly if significant HPC resources are available.

Another limitation of these simulations is the simple ocean forcing parameterisation used (Holland and Jenkins, 1999), which uses just one value for temperature and salinity to represent the whole ocean. Furthermore, the supplied temperature and salinity values were generated from whole continent ice sheet tuning and not concentrated on the Amery region. These values could impact other modelled parameters, but despite these limitations the results show a modelled steady state close to the present day LAGS and AIS configuration. More recent results relating to the impact of warm water pathways (Nitsche et al., 2017) are likely to impact on the AIS and are investigated in Chapter 4.

Our experiments indicate that a well-sampled bathymetry, and coastal pinning points in particular, impact significantly on the response of an ice sheet model. If the AIS is ungrounded from the pinning points near the calving ice front, this could have significant impact on the grounding line region upstream. The implication for mass-loss prediction is that each ice shelf system is likely to respond to climate forcings in a non-linear way as the ice retreats sequentially over small pinning points. At certain stages, the ice shelf as a whole would lose mass more slowly, when buttressed by a pinning point, followed by periods of accelerated retreat when the mass loss rate would increase, after ungrounding. The response of the AIS at successive stages of retreat is investigated further in the next chapter.

Progress in the near future is likely through the use of modelling/interpolation enhanced datasets (Morlighem et al., 2019; Leong and Horgan, 2020) that improve upon and/or complement the directly observational compilations such as BEDMAP2 (Fretwell et al., 2013). It is clear, however, that observational programs (e.g. airborne gravity, ice shelf seismic surveys, or AUV surveys) that improve knowledge of detailed bathymetry, including small features that could behave as pinning points, in the coastal zone are of highest priority.

2.5 Conclusions

A numerical ice sheet model was used to investigate the sensitivity of the LAGS to four geometries of the bathymetry and inclusion of synthetic pinning points at the calving front. The impact of calving parameter choice was also investigated. Our findings show the strong influence of the bathymetry on the evolution of the LAGS and the impact of pinning points of small-scale on the calving front position and ice velocity across the grounding line and calving front. Tuning of calving parameters allows the calving front position to be further refined.

Our experiments show that the choice of bathymetry substantially impacts the modelled grounding line position demonstrating that shallow bathymetries generate an advanced grounding line and calving front, which leads to inaccuracies in the modelled dynamics and stresses of the LAGS and AIS. In contrast, a bathymetry with a deep sub-ice cavity at the southern grounding line reproduces a grounding line position that is very close to observations. This consequently minimises the misfit between modelled and observed ice velocity and ice thickness of the LAGS. To identify the cause of the remaining discrepancies, further simulations were carried out on a finer grid with 5 km resolution. The present choice for the horizontal resolution (5 km) relates to the limit of available computational resource.

The inclusion of the synthetic pinning points, Podlednyj holm and Triangle, near the calving front reduces the misfit between modelled and observed calving front position, and upstream ice velocity near the deep ice in the south of the AIS. These synthetic pinning points are of small-scale (Podlednyj holm at 6 km^2; Triangle at 5 km^2) in comparison to other islands, rumples or nunataks within the LAGS but their presence is significant since they lead to an advancement of the grounding line. An iterative refinement of the dimensions of the newly included pinning points resulted in better predictions of ice velocity across the deep grounding line, ice thickness on the ice shelf, and calving front position. Their presence provided significant buttressing and led to slight lateral spreading of the calving front. The employed model is currently most limited by the simplicity of the ice-ocean interface parameterisation, nevertheless, the exploration of bathymetries and pinning points clearly indicates a geometry that is well-suited for present day simulations of the LAGS or for reconstructing the evolution of the LAGS over a long period of time. Buttressing by pinning points has particular impact in the case of a relatively narrow, incised channel such as found in the LAGS.

Overall, our findings demonstrate that perturbing the bathymetry under the AIS results in qualitative differences in model outputs over a large spatial scale. An under-sampled bathymetry could therefore lead to undue emphasis on poorly constrained modelling parameters that require tuning to reproduce the ice shelf dynamics. The results of these sensitivity experiments reinforce the importance of accurate bathymetric data at high resolution close to the grounding line and the accurate mapping of pinning points near the calving front that have basal contact with an ice shelf, even if the features are of small scale. Improved bathymetry data would reduce models bias and/or uncertainty in predictive simulations, both in the LAGS and other regions of Antarctica. These conclusions are expected to apply to other ice shelves, with either broad or narrow embayments. As only sparse and low resolution bathymetry data are presently available for most of Antarctica's ice shelves, our findings highlight the importance of a coordinated effort to obtain high-resolution bathymetry data sets for the regions under Antarctica's ice shelves.

Chapter 3

Stability of the Amery Ice Shelf to Retreat by Calving

The Amery Ice Shelf (AIS) is the largest ice shelf in East Antarctica. Its presence provides stability to the Lambert-Amery Glacial System (LAGS) due to the buttressing effect imposed by the floating ice shelf on the grounded ice of the LAGS. The last two large iceberg-calving events occurred in late 1963 to early 1964 when 10,000 km^2 of the ice shelf broke away, and in 2019 when a smaller area of floating ice, 1500 km^2, was released. Little is known, however, about the probable retreat of the AIS as a function of iceberg-calving including a potentially increased rate of calving in the future. Herein we use a numerical model to investigate the dynamic response of the AIS to retreat by calving. We impose different retreat scenarios across the AIS calving front and quantify changes in ice velocity, strain rate, strain-flow angle and calving rate. These variables are used to assess the stability of each calving front configuration, and dynamic changes to the ice shelf. In this context, the ice shelf is considered 'stable' if the model does not show significant advance, retreat or accelerated calving for the given ice front position.

Our results show that the area of truly passive ice on the AIS is slightly larger than found in previous studies, and this may be due to the presence of small-scale pinning points near the present day calving front which are included in our model but were neglected in previous modelling. We identify regions across the AIS where where ice removal might cause a speed-up of the neighbouring upstream region, but not a catastrophic speed-up of the whole LAGS. Two alternative criteria for ice shelf stability are in general agreement that the AIS is stable until it retreats to approximately 85 km upstream of the current calving front, meaning that retreat less than this would result in the likely re-advance of the remnant ice shelf if no further perturbation of the geometry occurs. In retreated geometries up to this point there is little acceleration of the ice at the grounding line. In the case of further retreat scenarios, the two criteria and calving considerations suggest that the central part of the AIS would be unstable, with a more stable situation arising when the retreat nears the topographic highs in the southern part of the AIS. Therefore our study suggests that the AIS can retreat without leading to significant contributions to sea-level rise.

3.1 Introduction

The Amery Ice Shelf (AIS) occupies 2% of the East Antarctic coastline and is fed by its main ice stream, the Lambert Glacier, and other tributary glaciers including Mellor and Fisher. These ice streams bring ice from as far inland as Dome Argus and Dome Fuji (Figure 1.2) and converge into a drainage system, draining a volume of ice greater than the entire West Antarctic Ice Sheet (WAIS). The entire drainage basin is equivalent to 10% (Zwally et al., 2012) of the area of the East Antarctic Ice Sheet (EAIS), with a flux of 56.0 ± 0.5 Gt year^{-1} at its grounding line (Rignot et al., 2013).

Antarctica gains mass from snow accumulation, and its main sources of mass loss are iceberg-calving and basal melt. The main contributor to mass loss from the Lambert-Amery Glacial System (LAGS) is calving, followed by basal melting (Rignot et al., 2013; Depoorter et al., 2013). Ice shelf basal melting and iceberg melt make a smaller contribution to sea-level change (Jenkins and Holland, 2007). A floating ice shelf provides stability to an ice sheet, buttressing the ice upstream and slowing down the flux of grounded ice to the ocean (Dupont and Alley, 2005; Borstad et al., 2013; Gudmundsson, 2013). Factors that contribute to such buttressing are the presence of pinning points, and lateral shearing from the channel walls. Pinning points are topographic rises from the seafloor that have contact with the base of a floating ice shelf and provide a buttressing effect. Small changes in basal melt rate can change the contact area of pinning points, which reduces frictional buttressing (Sun et al., 2014; Alley et al., 2015; Matsuoka et al., 2015; Berger et al., 2016). Also, accumulation of surface meltwater, for example in the presence of melt ponds on the surface of an ice shelf, can wedge open crevasses leading to hydrofracturing (the enhanced growth of crevasses by water pressure) which reduces backstress (resistance to ice flow), and can disintegrate an ice shelf (Pollard et al., 2015; DeConto and Pollard, 2016; Borstad et al., 2013). Changes in the configuration of an ice shelf can be triggered by warm ocean underneath the ice shelf leading to dynamic thinning of tributary ice streams (Pritchard et al., 2012).

The presence of frontal passive ice means that not every calving event produces an instantaneous dynamic ice shelf response (Reese et al., 2018b). Passive ice is defined as ice which provides limited buttressing to the rest of the shelf, and its removal from an ice shelf does not induce an increased flux of ice towards the ocean nor conduce any further retreat of the ice front (Fürst et al., 2016). However, changes beyond the passive ice area would lead to positive feedback and a catastrophic collapse of a significant part of the ice shelf (i.e. makes the ice structure unstable). For a homogenous ice shelf, the principal strain rate components may be considered (Doake et al., 1998) such that calving of the frontal part of the ice shelf becomes likely when the ice is no longer in compression. The existence of suture zones (a mechanically soft heterogeneity consisting of marine ice, meteoric ice and in situ snowfall with modified rheological properties) along the ice shelf is a factor that may contribute to stability. These zones hinder the propagation of rifts because the softer suture zone ice can deform to relieve stress concentrations around the rift tip (Jansen et al., 2013; McGrath et al., 2014; Borstad et al., 2017). Results from the Larsen C Ice Shelf (West Antarctica) suggest that when rifts or crevasses are able to cross the suture zones they propagate because purely meteoric ice is not malleable (Jansen et al., 2013; Kulessa et al., 2014; McGrath et al., 2014; Jansen et al., 2015; Borstad et al., 2017). Hence deformation, by both extension and compression, in the along-flow direction of ice impacts the calving front where strain rates are high, leading to the formation of crevasses, fractures or rifts, which control the formation of icebergs.

The calving of the Amery Ice Front is thought to occur in a cyclic fashion approximately every 60–70 years (Fricker et al., 2002b), a conclusion derived from 10 epochs that span from 1936 to 2000, with the last major events in late 1963 and 2019. The late 1963 to early 1964 event resulted in 10,000 km^2 of ice shelf being released. The event on 26th September 2019 appears to have occurred approximately 10 years earlier than expected with atmospheric extremes playing a significant role (Francis et al., 2020, in review) and resulted in the release of 1500 km^2 of ice. The calving of iceberg D-28 on 26th September 2019 occurred before the ice front reached the extent into Prydz Bay that preceded the 1963 event. This observation further prompts an investigation into the response by calving of the AIS to different scenarios of retreat from the present day configuration. To the author's knowledge, no previous study of the stability of the AIS under different retreat scenarios has been undertaken.

Herein, we use a hybrid ice sheet model to simulate responses for the AIS to study (i) the extent of passive ice on the shelf, where removal of the frontal section of an ice shelf does not provoke a sudden change in ice velocity, (ii) the stability of the Amery Ice Shelf under different retreat scenarios, (iii) the average horizontal calving rates across the ice front of the AIS for each retreat scenario. The aim of these experiments is to understand how the position of calving front would be likely to affect the remnant ice shelf.

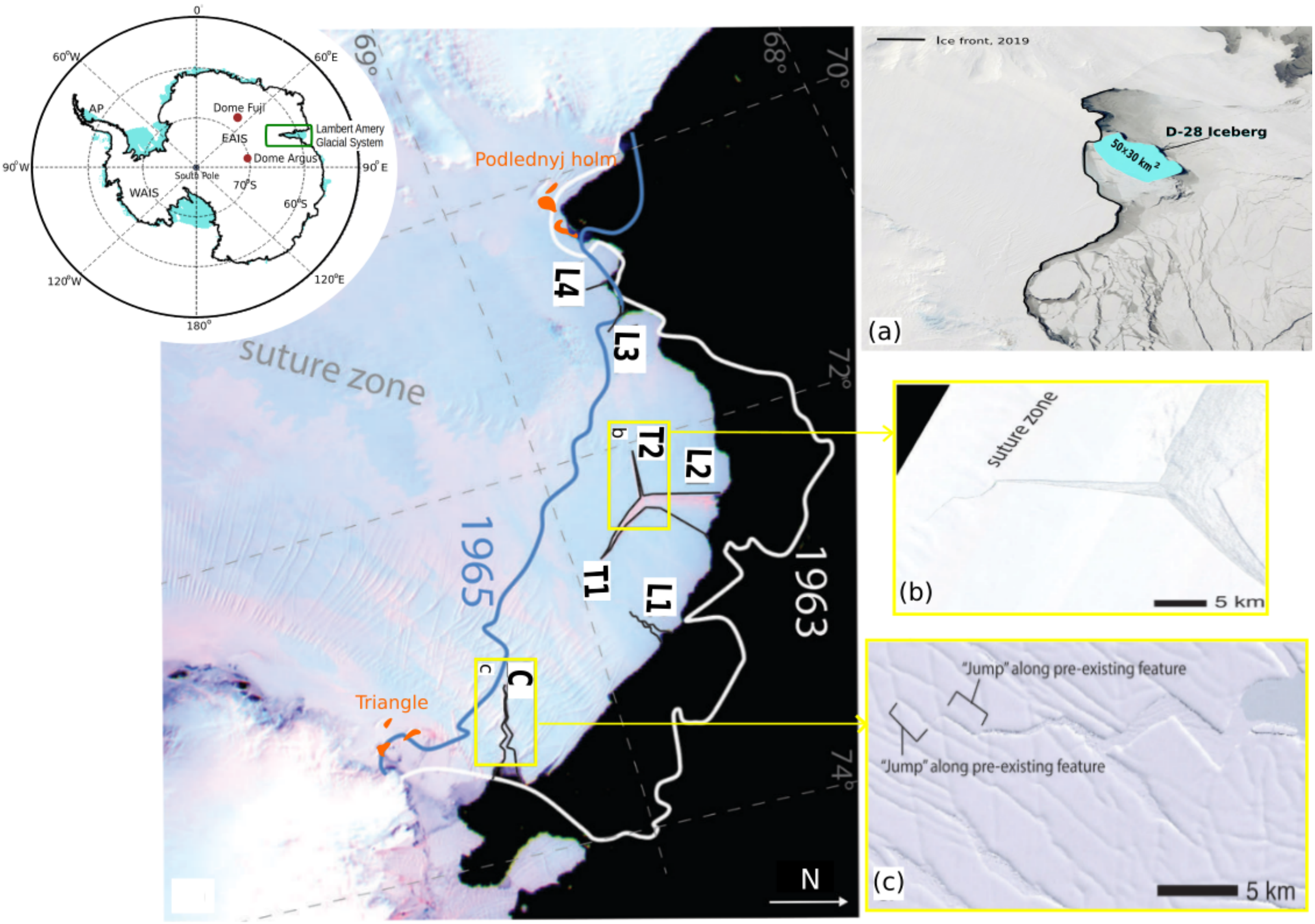

Figure 3.1: Main image shows rifts near the calving front of the Amery Ice Shelf before the calving of the D-28 iceberg (inset shows Antarctica with Dome Fuji and Dome Argus in East Antarctica). (a) Ice front image with new calving front configuration (solid black line) and the D-28 iceberg (light blue fill) on 26$^{\mathrm{th}}$ September 2019. (b) Enlarged figure of the area denoted as 'c' in panel a. (c) Enlarged figure of the area denoted as 'c' in main image. The main image, (b), and (c) are modified from Walker et al. (2015). Note that (b) and (c) are rotated with respect to the main image.

3.2 Background

3.2.1 *Calving of the Amery ice front*

Three major outlet glaciers (Lambert, Mellor, and Fisher Glaciers, Figure 3.1) drain the ice from the interior of the EAIS and feed the AIS. Where these glaciers merge, suture zones are formed (Jansen et al., 2013). Suture zones act to stitch together neighbouring meteoric flow units, and their presence inhibits the fast propagation of active rifts between the meteoric ice streams. The composite nature of suture zones makes them malleable with no fixed orientation, therefore rifts do not form in these regions, unlike in meteoric ice (Borstad et al., 2017). Temporal observations of rifts show that their length increases in episodic bursts, however, the widths of rifts grow steadily, akin to ice shelf spreading at the calving front (Bassis et al., 2005; Joughin and MacAyeal, 2005; Bassis et al., 2008). Propagation of rifts is affected by external forcings (e.g, ocean waves, tide, and atmospheric temperature rises leading to surface melt), and internal stresses that govern ice rheology (Bassis et al., 2008).

Figure 3.1(a) shows the rifts present near the calving front of the AIS in 2019, prior to and after the formation of iceberg D-28. Two rifts called the east rift (L1), and the west rift (L2) are longitudinal-to-flow rifts, and connect to two transverse-to-flow rifts (denoted T1 in the east and T2 in the west) forming a three way fissure at the base of rift L2 (Figure 3.1). This whole system has been referred to the Loose Tooth (LT; Fricker et al., 2002b). Additionally, further to the west of the LT system there are two longitudinal-to-flow rifts denoted L3 and L4 (Figure 3.1). The location of rifts L2 and L3 suggests their formation is related to flow bands, and is a result of ice sources and glacier history far upstream and a strong positive strain rate from the acceleration and widening of the shelf as it exits the narrow channel (Zhao et al., 2013). This may explain their formation in suture zones. The high transverse strain rates can separate the streams of ice flow from one another, creating weakened areas where rifts and crevasses can form. These rifts and crevasses are precursors to calving events (Walker et al., 2013).

On the eastern side of the Amery ice front there is a rift denoted simply as “C”, which is surrounded by multiple 40–50 km long crevasses. These crevasses intersect the longitudinal-to-flow rift C giving it a “zigzag” shape as it propagates upstream. Fricker et al. (2005) studied the two active longitudinal-to-flow rifts L1 and L2, from four sensors (Multi-angle Imaging SpectroRadiometer (MISR), Enhanced Thematic Mapper (ETM), RADARSAT, and ERS Synthetic Aperture Radar (SAR)) over a period of approximately eight years, and showed that the propagation of these rifts increases in summer and lessens in winter (Walker et al., 2015). The most recent (2019) calving of iceberg D-28 occurred on the section between L2 and L3 along the transverse-to-flow rift T2, where the distance between this section and the 1963 calving front position is nearly 40 km (Fricker et al., 2002b).

Previous investigations of factors influencing the AIS more generally include those concerning the active rifts along the calving front of the ice shelf as noted above (Walker et al., 2013), and the sensitivity of the LAGS to the geothermal heat flux boundary condition (Pittard et al., 2016). Gong et al. (2014) investigated the response of the AIS to warming climatic conditions using the BICICLES model with the distribution of basal melt being the main influence, causing thinning of the ice shelf. Such thinning is understood more generally to enhance the calving and retreat of ice shelves (Liu et al., 2015).

3.2.2 *Ice shelf safety margin hypotheses*

Although calving is a phenomenon that occurs in every ice shelf and is a major contributor to mass loss in Antarctica (Depoorter et al., 2013), understanding its full mechanical process is complex (Joughin and MacAyeal, 2005; Bassis and Jacobs, 2013). Multiple hypotheses have been formulated as criteria that establish critical ice front positions, beyond which the ice shelf becomes unstable, for different ice shelf configurations (Borstad et al., 2017). Previous related work, and hypothesised criteria, relating to ice shelf stability are individually discussed here to show the range of comparisons to be made for the AIS.

Fürst et al. (2016) use a method that quantifies upstream buttressing in a given horizontal direction by calculating the effective buttressing at each point in the ice shelf. This defines the extent of passive ice with little or no buttressing effect. The buttressing at a point within the ice shelf is determined by the difference between the depth-integrated stress exerted on the ice upstream of the point given the presence of an ice shelf downstream, and the depth-integrated hydrostatic driving pressure at that point (which would be the stress exerted in the absence of an ice shelf downstream). This difference is then normalised by the depth-integrated hydrostatic driving pressure.

Doake et al. (1998) considered the principal strain rate components of the northern Larsen Ice Shelf, treating ice as a continuum without fractures – an homogeneous ice shelf. Their approach focused on the contour that consists of only compressive strain rates of the second principal strain, called the "compressive arch". Calving beyond this arch was hypothesised to initiate an unstable ice shelf that would lead to an irreversible retreat of the whole ice shelf. Kulessa et al. (2014) and Jansen et al. (2015) examined rifting of the Larson C Ice Shelf using an ice shelf stability criterion based on the "stress-flow angle", the angle between the first principal stress and the ice flow direction. Regions of an ice shelf where the stress-flow angle approaches zero are considered susceptible to calving, due to the orientation of the tensile stress aligning closely to the ice flow direction, causing the first principal stress to act on the already existing rifts or crevasses. However, if the stress-flow angle approaches 90 ° then that region is hypothesised to exhibit stability.

From a modelling perspective, further insight may be gained by examining the probable re-

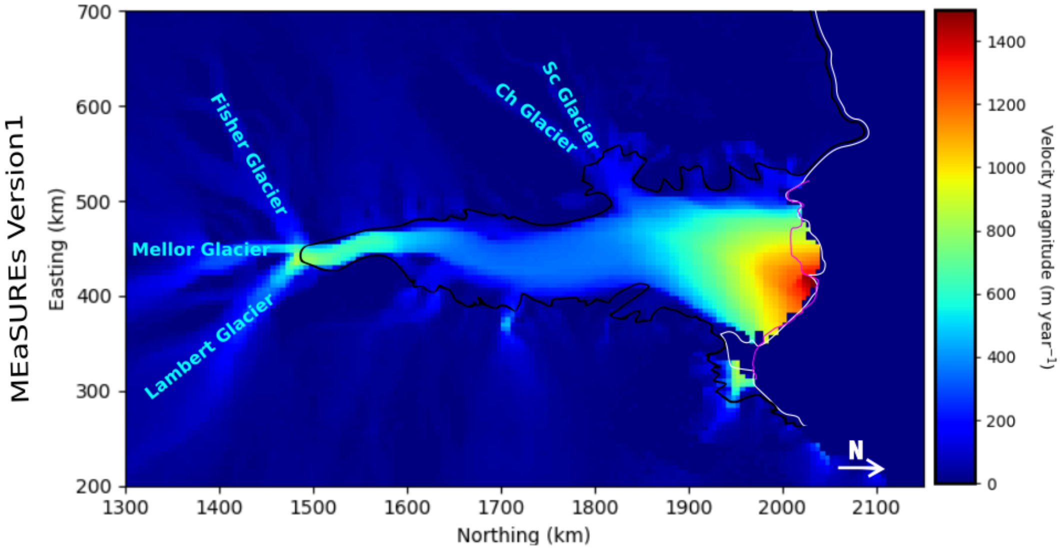

Figure 3.2: Ice velocity of the AIS from Rignot et al. (2013), showing the major Lambert, Mellor and Fisher Glaciers, along with the tributary Charybdis (Ch) and Scylla (Sc) Glaciers. The colour scale is chosen as similar to the original research from which this figure is taken. The grounding line (black line) and present day ice front (white line) are taken from Mouginot et al. (2017). The magenta outline is the calving front after the calving of D-28 iceberg

sponse of the ice front to calving through the eigencalving law (Levermann et al., 2012). This gives the calving rate at the ice front, based on the eigenvalues of the horizontal strain rate tensor. This calving rate may be compared to the frontal ice velocity (Figure 3.2) to infer if further retreat is likely. However, this method does not determine if a retreat is likely to be irreversible.

Investigations using the method of Fürst et al. (2016) do not address ice shelf stability, but rather differentiate the frontal section of an ice shelf which can be removed without causing a dynamical change to the remnant shelf. Investigations using the methods of Doake et al. (1998), and Kulessa et al. (2014) attempt to discover the conditions that would cause an irreversible retreat of an ice shelf. In this chapter we investigate the AIS response using each of these approaches, together with the calving rate to frontal ice velocity comparison.

3.3 Methods and Data

In this section, the numerical model used in this study is outlined, together with the observational datasets used as boundary conditions and model inputs. This is followed by an outline of the methods that underpin the numerical experiments: the along-flow strain rate is used to define five plausible retreat positions for calving fronts and the modelled values of the principle axes of strain underpin the stability analyses. In the final part of this section the experiments themselves are outlined.

3.3.1 *Parallel Ice Sheet Model*

The Parallel Ice Sheet Model (PISM: User's Manual available at www.pism-docs.org) Version 0.7.3 (Bueler et al., 2007; Bueler and Brown, 2009; Winkelmann et al., 2011; Martin et al., 2011) is a three-dimensional, computationally efficient model, coupled with basal sliding, and mass continuity at the calving front. It is a hybrid model that superposes two stress balance approximations: the shallow ice approximation (SIA), and the shallow shelf approximation (SSA). These stresses are used to calculate ice velocities of grounded ice, ice streams, and ice shelves. Stress, separated into shear and membrane stress (Hindmarsh, 2004, 2006), is a boundary force applied for ice flow, and PISM describes the velocity of ice as a function of driving stress (Bueler and Brown, 2009). The SIA dominates in grounded ice with a non-sliding base, while the SSA dominates in ice shelves and in fast moving regions of grounded ice (ice streams). These approximations are computed for the whole continental domain, and transition from one to another is calculated by a weighting function for a continuous smooth transition from the SIA across the grounding line to the SSA (Bueler and Brown, 2009).

The ice front position of an ice shelf is modelled by allowing the ice shelf to advance by a part of a grid cell, known as subgrid-scale representation (Albrecht et al., 2011), and the boundary condition at the calving front is a modification to the mass continuity and the SSA stress balance (Bueler and Brown, 2009). The stress at the calving front of an ice shelf, equates to a vertically integrated force balance formulated according to the equation

$$\int_{z_{sl}-\frac{\rho_i}{\rho_o}H_c}^{z_{sl}+(1-\frac{\rho_i}{\rho_o})H_c} \sigma.\mathbf{n}dz = \int_{z_{sl}-\frac{\rho_i}{\rho_o}H_c}^{z_{sl}} \rho_o g(z-z_{sl})\mathbf{n}dz \tag{3.1}$$

where z_{sl} is sea level, ρ_i and ρ_o are the densities of ice and seawater respectively, H_c is the ice thickness at the calving front, σ the Cauchy stress tensor, g is the acceleration due to gravity, and $\mathbf{n}$ =(n_x,n_y) is the horizontal normal vector perpendicular to the calving front.

The left hand side limits of the integration are terrain-following for outlet glaciers or floating calving fronts, and the right hand side calculates the pressure exerted by the ocean on the parts of the ice shelf that are below sea level. This equation determines the strain rates only on fully filled cells and not on the partially filled neighbouring cells at the ice front. Winkelmann et al. (2011) showed that the above equation can be used to distinguish three types of ice-ocean interface, namely the calving of floating ice shelf fronts, marine ice fronts at the coast that rest on the bedrock below sea level, and cliffs. Cliffs, in this application, also have ice fronts at the coast resting on bedrock, but the ice fronts are above sea level.

Levermann et al. (2012) introduced a calving rate law, the "eigencalving law", to the mass continuity equation in PISM (Winkelmann et al., 2011; Martin et al., 2011). While the advance of the calving front naturally happens through mass transport governed by the continuity scheme, retreat is governed by this physically-motivated calving law, which ensures (for example) that shelf ice would cut off at the mouth of a bays.

Boundary conditions and initialisation

The stress balances implemented in this study were the SIA and the SSA. The bedrock was regarded as rigid, impenetrable, fixed in all simulations, and parallel to basal shear stress and basal sliding velocity. The pseudo-plastic power law relates bed-parallel shear stress and velocity at the ice-bed interface and a quotient in the pseudo-plastic sliding law is used to control the basal strength assuming that there is a layer of till underlying the grounded ice (Winkelmann et al., 2011; Bueler and Brown, 2009). Equations are given in Chapter 1 that represent 'till cohesion' (Equation 1.7), and 'till friction angle' (Equation 1.8).

The basal shear stress, τ_b, is given by:

$$\tau_b = -\tau_c \frac{\mathbf{u}}{u^q_{threshold}|\mathbf{u}|^{1-q}}, \tag{3.2}$$

where τ_c is the yield stress, $\mathbf{u}$ is the sliding horizontal velocity vector, $u^q_{threshold}$ is a threshold velocity, and q is an exponent that can be tuned to adjust the sliding. If $q = 0$, then the above sliding law becomes a purely plastic sliding model.

The spatial location of ice streams is calculated from the yield stress, which is dependent on a subglacial hydrology model (Aschwanden et al., 2012, 2016) and the modelled till strength, which is a function of bed elevation (Martin et al., 2011; Winkelmann et al., 2011; Aschwanden et al., 2016; Pittard, 2016). We use a default hydrology model where water is not conserved but it is stored locally in the subglacial till up to a column height of 2 m, and any amount higher than this maximum value is lost with no feedback. The stress boundary condition at the calving front was based on the mass continuity equation and the geometry, which was held fixed in this study.

To initialise the diagnostic simulations, PISM requires boundary and forcing conditions. The bed topography and ice thickness, which provide the geometry of the domain, were taken from Fretwell et al. (2013) and stitched to a modified bathymetry around the southern most part of the grounding line, and included synthetic additions at the calving front representing the Podlednyj holm and Triangle pinning points (Figure 2.3 (d), full description in Chapter 2). Larger ice rises further south, closer to the grounding line (e.g. Clemence Massif, Robertson Nunatak, and Budd Ice Rumples) are also included. Forcing conditions for the atmosphere are present day spatially distributed near-surface air temperatures, and precipitation (RACMO2.3/ANT27, year 1979-2014; Van Wessem et al., 2014). The surface mass balance is computed from input data of precipitation and near-surface air temperature (RACMO2.3/ANT27, year 1979-2014; Van Wessem et al., 2014). The air temperature is used to calculate the energy available to melt ice at the ice surface interface by employing a positive degree-day (PDD) model (Aschwanden et al., 2013; Seguinot et al., 2014). PDD is defined as the integral of temperatures above 0 ° C in one year which in our case is between 0.37 K and 8.36 K. The lapse rate (8.0 K km^{-1}) applied to the 2 m (above surface) air temperature forcings serves as the boundary condition for the conservation of energy equation that corrects the differences between the fixed surface ice elevation and the time evolving modelled elevation (Aschwanden et al., 2013; Seguinot et al., 2014). The ice shelf basal melt rate is controlled by the ocean's potential temperature (271.3 K) and salinity of the adjacent ocean (27.0 g/kg) were used to initialised basal melt at the ice-ocean boundary layer (Holland and Jenkins, 1999).

The annual mean surface temperature and geothermal heat flux (An et al., 2015) are provided as boundary conditions for the advection and vertical conduction of heat through the grounded ice layers, while pressure melting temperature is also needed in the case of ice shelves as a boundary condition (Winkelmann et al., 2011). PISM calculates the ice temperature in these unequal horizontal layers. The forcing values were applied along with PISM tunable parameters that were generated in a large ensemble by Latin hypercube sampling (Santner et al., 2003) until a steady state was obtained close to the present day configuration (full details in Chapter 1).

Spin-up

The present day boundary and forcing conditions were used as inputs in a multi-stage spin-up procedure at a 10 km horizontal resolution. In the first and second stages, only the SIA stress was applied with one year and 100 year long simulations for each stage respectively. In the first stage, the present day climatology data are read in and the resolution of the simulation is specified. The second stage is the 'smoothing' stage. This stage uses the stress balance only for grounded non-sliding ice, i.e where the basal drag is very high to smooth out the peaks in stress arising from ice surface roughness. The output of this stage acted as input data for the next stage where the geometry was held fixed, allowing the thermal evolution of the ice mass in a 250,000 year run. The long duration is due to the slow rate of advection of thermal parameters within the ice sheet. From the thermally-evolved ice sheet, all lateral boundaries, and geometry are free to evolve in the last stage of the spin-up where the full physics of the ice sheet was applied for 40,000 years. A steady state was identified when the time series of total ice volume with respect to time showed little further change (Bueler and Brown, 2009;

Pittard, 2016). The thermal fields from the modelled state obtained with 10 km resolution were further simulated at 5 km horizontal resolution. This 'change in grid' approach saves computational resources, allowing a wide parameter search at a coarse resolution, which then required a further relaxation to steady state for 38,000 years. The parameters used are given in Table 3.1 and their values are discussed in detail in Chapter 1. Calving parameters were not needed here as the calving front position was enforced in each experiment for each retreat scenario as described in the following section.

Parameter	Value	Description
sia_e (unitless)	2.7	Enhancement factor for grounded ice where vertical shear dominates.
ssa_e (unitless)	1.8	Enhancement factor for floating ice where horizontal shear dominates.
q (unitless)	0.8	Exponent in the pseudo-plastic flow law (Eq 2).
till (unitless)	0.01	A tuning parameter of the effective pressure of ice against pressurised water in the till.
ϕ (unitless)	10.0, 25.9, -760.0, 1279.0	Tuning of till strength depending on bed elevation. It varies the strength of the basal resistance by setting till friction angle as a function of bed elevation, i.e at -760 m bedrock depth till angle is 10.0°, and when bedrock depth goes to 1279 m, till angle is 25.9°.

Table 3.1: Parameter choices.

3.3.2 *Along-flow strain rate of the Amery Ice Shelf*

The along-flow strain rate is used in this study to guide the construction of plausible retreated calving front traces following the method employed by Wearing et al. (2015). It is calculated from the modelled velocity of ice at each grid point, from values contained in adjacent cells of the ice shelf in the direction that aligns with the direction of ice flow, and its vector notation is given as:

$$f_1 = \hat{\mathbf{u}}.\mathbf{e}.\hat{\mathbf{u}} \tag{3.3}$$

where $\hat{\mathbf{u}}$ is a unit vector in the direction of ice flow, and $\mathbf{e}$ is the two-dimensional (2-D) strain rate tensor expressed as :

$$\mathbf{e} = \begin{pmatrix} e_{xx} & e_{xy} \\ e_{xy} & e_{yy} \end{pmatrix} = \begin{pmatrix} \frac{\partial u}{\partial x} & \frac{1}{2}(\frac{\partial v}{\partial x} + \frac{\partial u}{\partial y}) \\ \frac{1}{2}(\frac{\partial v}{\partial x} + \frac{\partial u}{\partial y}) & \frac{\partial v}{\partial y} \end{pmatrix} \tag{3.4}$$

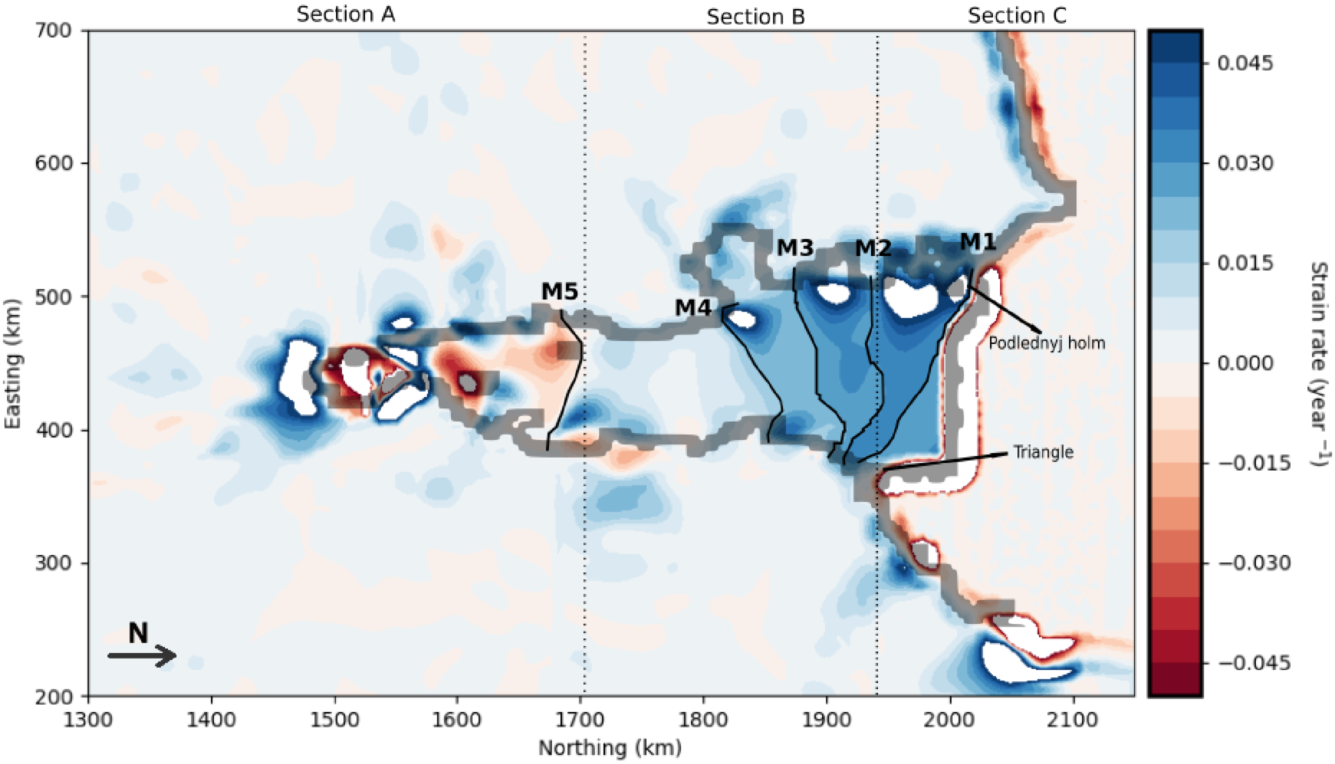

Figure 3.3: The along-flow strain rate on the AIS and inflowing glaciers, where blue is extensional flow and red is compressive, at 5 km horizontal resolution for the steady state model result. The dark grey line shows the grounding line and ice front, again for the steady state result. The five black solid lines represent the simulated model calving front geometries (M1 to M5) to be used as retreat scenarios in the experiments in this study. These are constructed to start from the west side of the AIS at logical intervals in space, taking into account notable features in the bathymetry. The traces of these model ice fronts then follow along-flow strain rate values of: 0.029, 0.029, 0.025, 0.020, and 0.002 year^{-1} respectively. The two pinning points, Podlednyj holm and Triangle, are located at the ice front (as in Figure 2.3(d)). The negative values at the ice front are a processing artefact (see main text).

where u is the velocity component in the x-direction, and v is the component in the y-direction.

To suppress artefacts in the strain rate due to noise, a 2D Gaussian filter (a Gaussian kernel with a 3 sigma standard deviation assuming a grid size of 5 km) is applied to the modelled ice velocity in both the x-direction (e_{xx}), and y-direction (e_{yy}). This filtering does not affect the larger-scale ice velocities or strain rates. The resulting array of strain values e_{xx}, and e_{yy} was then evaluated to obtain the spatially varying along-flow strain rate of the AIS, depicted in Figure 3.3 (5 km horizontal resolution, steady state).

Within Section A of Figure 3.3, the region upstream of the grounding line where the three glaciers (Lambert, Mellor, and Fisher glaciers) meet shows positive strain rates. At the transition zone between the grounded and floating ice, a high magnitude negative strain rate is seen. This is caused by the very narrow shape of the embayment. The negative strain rates continue downstream due to the presence of large ice rises such as Clemence Massif and Robertson Nunatak (Figure 3.4, M1) which compress the ice.

In Section B of Figure 3.3, the embayment broadens with an absence of pinning points leading to nearly zero to slightly positive strain rates, indicating that the ice flow is starting to spread. A high magnitude positive along-flow strain rate is observed where deformation is affected by the ice flow from the Charybdis and Scylla Glaciers, which impacts the ice flow direction perpendicular to the calving front. As these tributary ice flow entry points are not hindered by pinning points or ice rises, which is the case in Section A at close proximity to the grounding line, the deformation is solely due to ice spreading. Lastly, in Section C, the positive along-flow strain rate arises from further spreading of the ice and formation of fractures and rifts, as the ice advances towards the calving front of the ice shelf into the open ocean. The band of negative along-flow strain rates on the ice-ocean boundary along the coastline and ice front is due to the sampling of cells with zero ice velocity in the ocean.

Overall, these changes in strain rates along the AIS reveal that strain rates are strongly dependent on the geometry of the bathymetry and location of tributary glaciers flows along the ice shelf.

3.3.3 *Principal axes of strain*

Some of the experiments that we conduct in this study make use of criteria for assessing ice shelf stability that are based on principal strain rates. The 1st principal axis of strain is aligned along the maximum principal strain rate, and the 2nd principal axis of strain is along the minimum principal strain rate (perpendicular to the 1st principal strain rate). The deformation (compression) of the 1st principal strain rate on an ice shelf can be caused by pinning points or ice rises, which compress the ice as it flows. Shearing of ice in the 2nd principal axis of strain is due to lateral resistance as the ice drags against the channel wall. The convention for both principal strain rates is that they represent extension when they are positive.

Both strain rates can be positive or negative. For the AIS, at its calving centre when ice exits the confined embayment, both strain rates are positive due to the transition of the 2nd principal strain rate from compression to extension. This equates to an ice shelf spreading in the lateral and along-flow directions, and an absence of shearing along the channel wall. The behaviour of principal strain rates provides information to quantify the formation of crevasses and rifts at the ice front, and deformation upstream caused by pinning points.

The transformation of the strain rate tensor given in Equation 3 to a reference frame with an angle of orientation (θ) to the original frame is required to understand the possible variation in the direction of the two principal axes of strain along the AIS.

$$\begin{pmatrix} e'_{11} & e'_{12} \\ e'_{12} & e'_{22} \end{pmatrix} = \begin{pmatrix} cos\theta & sin\theta \\ -sin\theta & cos\theta \end{pmatrix} \begin{pmatrix} e_{xx} & e_{xy} \\ e_{xy} & e_{yy} \end{pmatrix} \begin{pmatrix} cos\theta & -sin\theta \\ sin\theta & cos\theta \end{pmatrix} \tag{3.5}$$

In the reference frame, the angle of orientation is evaluated from:

$$\theta = \frac{1}{2}\tan^{-1}\frac{2e_{xy}}{e_{xx}-e_{yy}} = \begin{cases} \theta_a \\ \theta_b \end{cases} \tag{3.6}$$

where the two principal axes of strain are separated by 90°, hence,

$$\theta_b = \theta_a + 90 \tag{3.7}$$

$$e'_{11} = max \begin{cases} e'_{11a} = e_{xx}cos^2\theta_a + e_{yy}sin^2\theta_a + e_{xy}sin\theta_a cos\theta_a \\ e'_{11b} = e_{xx}cos^2\theta_b + e_{yy}sin^2\theta_b + e_{xy}sin\theta_b cos\theta_b \end{cases} \tag{3.8}$$

which define the 1st principal strain rate to be aligned in the direction of maximum absolute principal strain rate. If e'_{11a} is less than e'_{11b}, then the 1st principal axis of strain is aligned at an angle of $\theta_b = \theta_a + 90$.

The calculated principal components of the horizontal strain rates are used to identify ice shelf stability following the method of Doake et al. (1998) and are also used together with the ice flow direction to calculate the strain-flow angle following the method of Kulessa et al. (2014).

The principal strain rates are also applied to the equation below (Levermann et al., 2012) which defines the average calving rate:

$$c = K\dot{e}_{11}\dot{e}_{12}, \tag{3.9}$$

where c is the average calving rate (m year^{-1}), K is a constant parameter which can be tuned to match observed calving rates , $\dot{e}_{11}$ and $\dot{e}_{12}$ are the principal strain rates (sec^{-1}).

3.3.4 *Experiments*

The model configurations of five different calving fronts for the AIS were constructed, representing a sequence of ice shelf retreat scenarios. These were defined by following contours through the along-flow strain rate from the steady state of the AIS which was simulated at a 5 km horizontal resolution with a freely evolving geometry (Figure 3.3 and accompanying text, Figure 3.4). Each synthetic configuration comprises the resulting ice surface elevation, bedrock elevation, and the calving front position. These were then simulated again at 5 km horizontal resolution but with no mass flux for a 0.1 year simulation run time, yielding the instantaneous modelled upper surface velocity of the ice of all five simulated model calving front geometries M1, M2, M3, M4 and M5 (Figure 3.5).

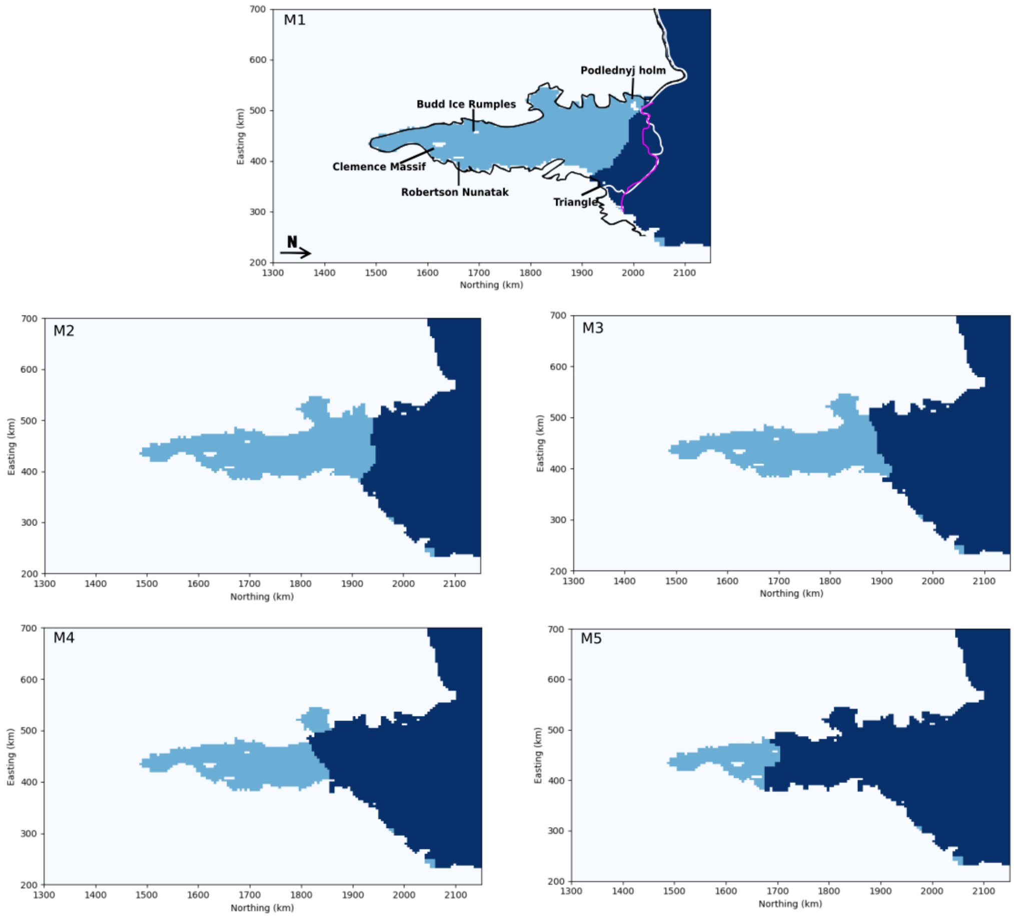

Figure 3.4: Synthetic ice shelf model geometries (M1 to M5) representing a sequence of retreat scenarios for the AIS for the calving fronts constructed as shown in Figure 3.3. Grounded ice areas (palest blue), the AIS (light blue) and ocean areas (dark blue) are shown. The modelled present day grounding line (black line), ice front before the calving of D-28 iceberg (white line), and ice front after D-28 iceberg calving (magenta line) is shown on the panel of M1.

To investigate the probable response of the AIS to retreat by calving for simulated ice shelves representing the five different retreat scenarios, several experiments were carried out. Firstly, to determine the extent of passive ice (Experiment 1), we compared the surface velocity of each model geometry against the spin-up simulation. Next, to examine ice shelf stability, we calculated the 2$^{\mathrm{nd}}$ principal strain rate component (Experiment 2), and the strain-flow angles between the strain rate and the ice flow direction (Experiment 3). Lastly, to determine if the ice shelf would be likely to advance or retreat (Experiment 4), the calving rates for each scenario were calculated, and the average of the highest calving rate values was compared to the ice velocity in the same grid cells.

3.4 Results

The following section describes the results of the four experiments for the five simulated ice shelf geometries to investigate the response of the AIS at each retreat scenario through a diagnostic modelling approach, and the resulting impact on ice velocity, ice flow direction along the ice shelf front, strain, and calving rates.

3.4.1 *Extent of passive ice - Experiment 1*

This experiment aims to identify the extent of the AIS that provides no buttressing and therefore has limited impact on ice shelf stability. Given the minimal speed-up in velocity upon removal, such sections of an ice shelf are known as "passive ice". Figure 3.5 shows the instantaneous model velocity when a frontal section is removed from the modelled steady state for the sequence of retreat scenarios (M1- M5). With every retreat position of the calving front a higher magnitude of velocity change occurs at the grounding line. The increase in ice velocity is negligible on the grounded ice sheet for each geometry, and velocity changes on the ice shelf are more pronounced at the calving front than for the deeper ice.

Qualitative changes in velocity in comparison to the modelled steady state are shown in Figure 3.6, again for each model geometry, to investigate which calving front is the closest upstream of the passive ice frontal region of the AIS. The percentage change in ice velocity for geometry M1 (Figure 3.6, M1) is higher on the eastern part of the ice shelf front, which may have been caused by the calving front retreating past the Triangle pinning point. Geometry M2 has an increased velocity across the whole calving front as shown in Figure 3.6 (M2). The increased velocity on the western part of the ice shelf front, in comparison to M1, may have been caused by the calving front having retreated upstream of the Podlednyj holm pinning point (Figure 3.4). Geometry M3 shows a significant increase in velocity, relative to M1 and M2, at the calving front and at the Charybdis and Scylla glaciers inlet, with velocity changes penetrating further south than geometry M2. This increase in velocity indicates that the calving trajectory of geometry M3 has passed the threshold of passive ice. Geometry M4 shows a dramatic increase in velocity at the calving front compared with M3 calving front, as well as along the Charybdis and Scylla glaciers inlet and NS region. The most extreme retreated calving front position of M5 shows a large increase in velocity for the southern region as far as the ice rise of the Clemence Massif.

The percentage change in velocity was calculated within three regions (enclosed in yellow outlines in Figure 3.5 (M1)) denoted as DI, CS, and NS. DI represents the deep ice of the LAGS, CS the Charybdis and Scylla glaciers inlet, and NS the neutral strain rate region (Figure 3.3). The calculated percentage velocity change in DI, CS, and NS is shown in Table 3.2. DI is a region which is not required for investigating passive ice as it is a non-frontal section of the calving front, but changes in DI likely indicate which calving front position would impact the deep ice and suggesting a change in buttressing effect with each retreat. The NS region serves as a general indicator region for the AIS as this region is dominated by neutral strain rate (Figure 3.3) where the embayment starts widening and there is an absence of pinning points.

DI	Values	CS	Values	NS	Values
M1	0.1%	M1	6.7%	M1	6.7%
M2	0.2%	M2	13.8%	M2	18.1%
M3	0.6%	M3	29.4%	M3	48.7%
M4	1.5%	M4	142.4%	M4	132.4%
M5	27.6%	M5	not applicable.	M5	not applicable.

Table 3.2: Percentage velocity change (areas DI, CS & NS are shown in Figure 3.5).

3.4.2 *Second component of principal strain - Experiment 2*

The hypothesis of Doake et al. (1998) states that a calving front is stable if the 2$^{\mathrm{nd}}$ component of principal strain at the calving front is compressive. Figure 3.7 presents the calculated 2$^{\mathrm{nd}}$ principal strain rate for each calving front geometry, including the modelled steady state. The modelled steady state (Figure 3.7, first panel) shows that AIS can be divided into two main sections on the basis of this property. Firstly, an area of compressive 2$^{\mathrm{nd}}$ principal strain rate near the calving front, followed by alternate zones of compression and extension in the 2$^{\mathrm{nd}}$ principal strain rate further upstream. These two sections are divided by a separator, shown as a solid black line in Figure 3.7 (steady state). At the ice shelf front of the modelled steady state there are sections where the strain rate is low compared to neighbouring sections. This may be related to the limited propagation of strain across the AIS and may share an underlying cause

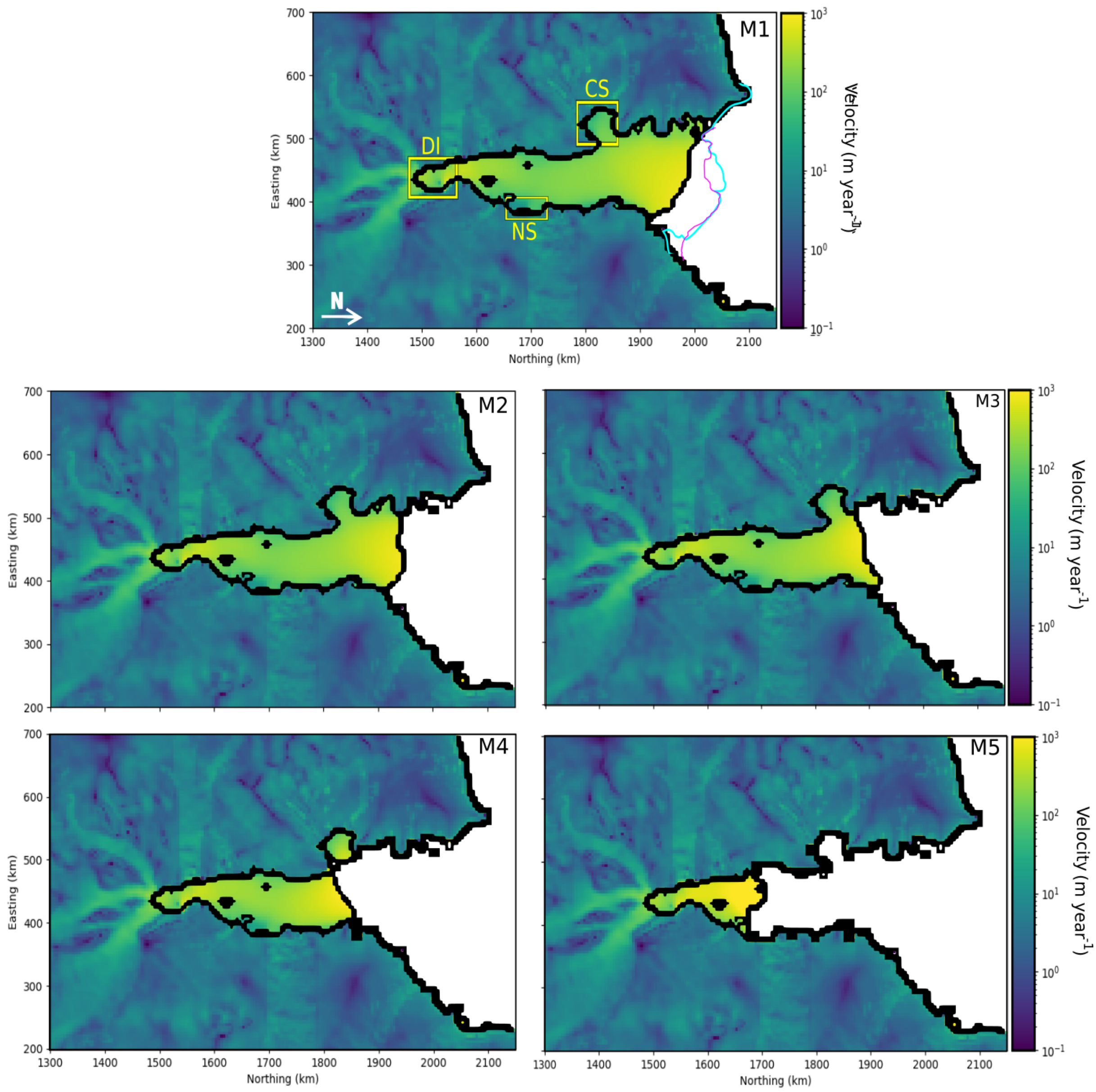

Figure 3.5: Instantaneous modelled ice velocity (logarithmic scale) across the AIS region, on removal of the frontal ice for simulated model calving front geometry (Figures 3.3 and 3.4). The enclosed regions, denoted DI, CS, and NS, are the regions for which the percentage changes in velocity are calculated (Table 3.2). The calving front (Mouginot et al., 2017) is shown as the cyan line and the calving front after D-28 iceberg calving is shown as the magenta line in the panel M1.

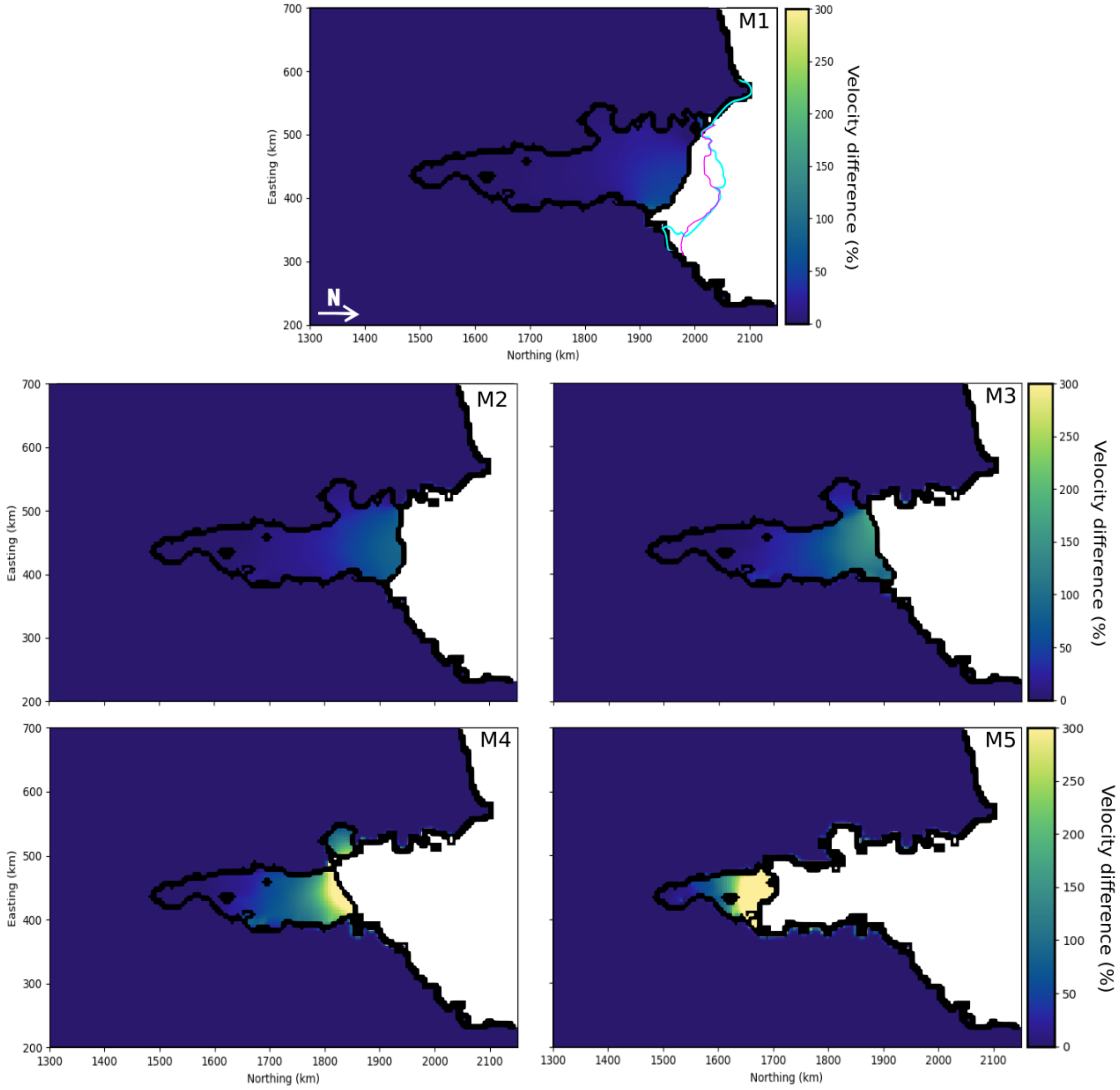

Figure 3.6: Percentage increase in ice velocity for each simulated model calving front geometry (Figures 3.3 and 3.4) in comparison to the steady state. There are no negative values for the change in ice velocity. The calving front (Mouginot et al., 2017) is shown as the cyan line and the calving front after D-28 iceberg calving is shown as the magenta line in the panel M1.

with the tendency of the AIS to generate along-axis rifts 3.1.

The configurations from steady state to M3 show compression in the 2nd principal strain rate at the ice shelf front, but this compressive region decreases in areal extent for calving front retreat positions further upstream (M4 and M5). The narrow band of low strain rate at the ice-ocean interface is a processing artefact due to the zero velocity in model cells outside the ice shelf. The absence of any compressive 2nd principal strain rates at the centre of the calving front of geometry M4, excluding the artefact, indicates that this geometry is likely to be an unstable system according to the theory of Doake et al. (1998). Geometry M5, which shows a high magnitude of compression, which indicates that the system has shifted to become stable again.

3.4.3 *Angle between principal stress and ice flow - Experiment 3*

As a further ice shelf stability criterion, we also conducted an experiment according to the method used by Kulessa et al. (2014) and Jansen et al. (2015), which uses the angle between the 1st principal stress and the ice flow direction. An ice shelf geometry is hypothesised to be stable for regions where this angle is close to 90°, while ice shelves with low stress-flow angles are likely to be more affected by small-scale calving because stresses act to open existing weaknesses. In a two-dimensional isotropic material, the principal orientations of stress and strain are the same. We therefore use strain-flow angles rather than stress-flow angles in this analysis of the AIS, as the two angles will be identical. The results are summarised in Figure 3.8 for all ice shelf retreat configurations explored in this study.

For the steady state (Figure 3.8, first panel), large strain-flow angles are found at the eastern and western margins of the calving front caused by lateral shearing. Overall there is a contrast between the western part of the calving front which is dominated by low strain-flow angles, and the central and eastern parts, which are dominated by higher strain-flow angles. Geometry M1 shows substantially the same pattern as the steady state (Figure 3.8 (M1)). In geometry M2, the western margin of the ice front is set upstream of Podlednyj holm and strain-flow angles approach 0°, but the angles increase towards the convex profile in the eastern section of the ice front suggesting that this portion would be more stable. The calving front of M3 mostly shows a low strain-flow angle across the calving front. This implies that this system is unstable, which is also the case for geometry M4. However, geometry M5 shows mainly large strain-flow angles at the calving front, indicating a stable AIS system for this calving front location.

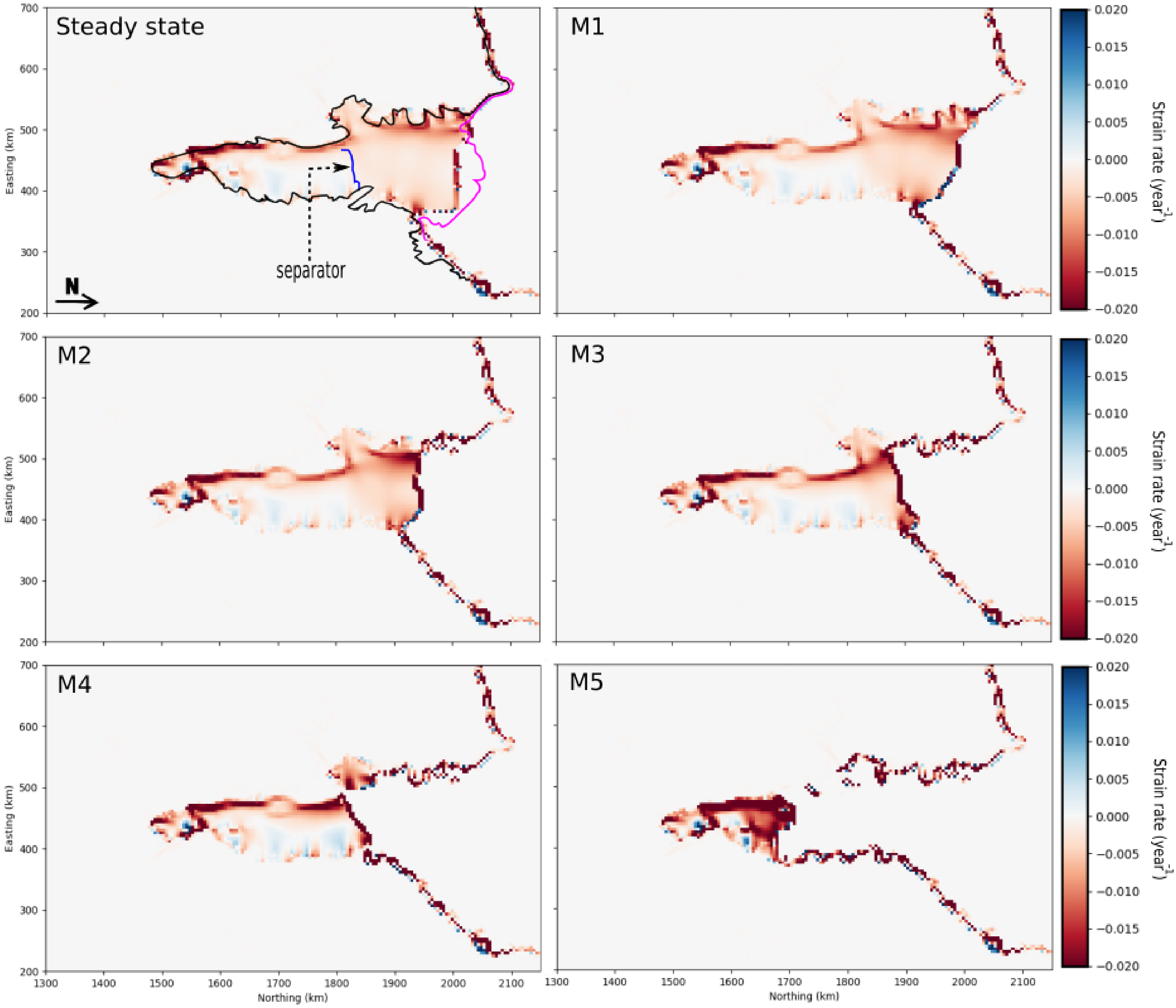

Figure 3.7: 2nd principal strain rates for each simulated model calving front geometry, where blue is extension, and red is compression. The fine blue line in the first panel indicated by the word 'separator' separates the oceanward region of compressive 2nd principal strain rate from the upstream region which has alternating areas of ice extension and compression. The present day grounding line (black line) and ice front (pink line) (Mouginot et al., 2017) is shown in the panel for M1.

3.4.4 *Calving rates - Experiment 4*

Calving rates are calculated for each simulated model geometry using the method of Levermann et al. (2012), based on both principal strain rates (Figure 3.9). The modelled present day steady state for the AIS shows very few locations where calving occurs, except in regions neighbouring the observed L1, L2 and C rifts. For geometry M1, there is no calving on the western part of

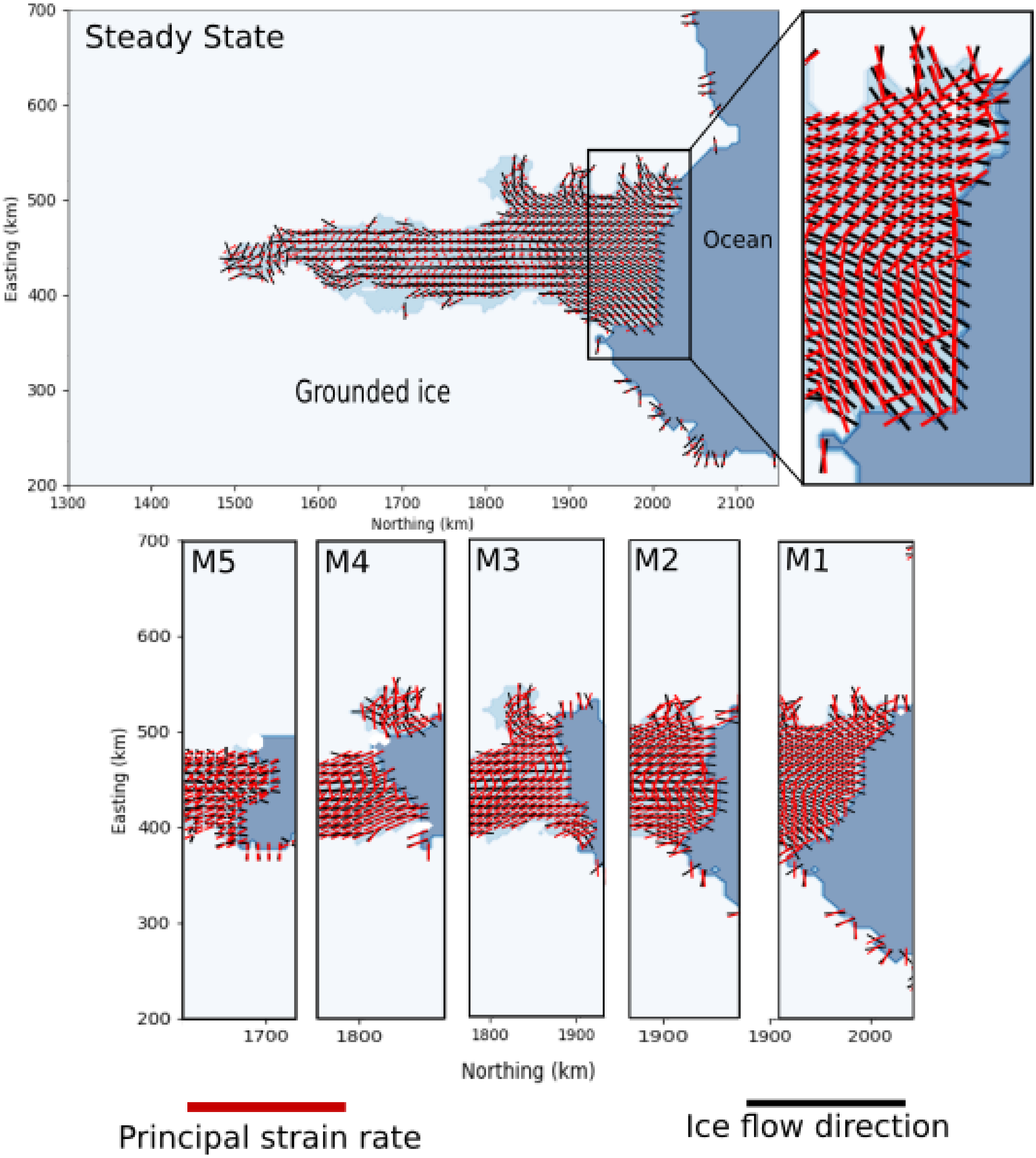

Figure 3.8: Ice flow direction (black bars) and 1st principal strain rate direction (red bars) for each geometry. Low strain-flow angles occur where the two bars align in direction. These regions are more likely to give rise to small-scale calving, whereas regions that exhibit strain-flow angles approaching 90° are likely to be more stable.

the ice shelf where it is pinned by the Podlednyj holm pinning points. On the eastern side of the ice shelf, the grid cells with the highest calving rates give an average calving rate of 2069 m year^{-1}. This implies a retreating eastern side of the ice front, as the average ice velocity in the same grid cells is only 737.0 m year^{-1}. Geometry M2 is predicted to calve on a narrower region at the eastern part of the ice shelf and its average calving rate is 1825 m year^{-1}, lower than the geometry M1 average calving rate but it would still retreat. Geometry M3 shows no calving along the majority of the calving front, indicating that this geometry is likely to advance rather than retreat. Geometry M4 has a slightly higher average calving rate than M2, of 1861 m year^{-1}, implying that the calving front might retreat because the ice velocity at M4 calving position is not more than 915.25 m year^{-1}. Lastly, the calving front of M5 has significantly higher average calving rates (4876 m year^{-1}) that would likely cause a rapid retreat as the ice velocity at M5 calving front position is close to 1766.0 m year^{-1}.

3.5 Discussion

In this section, the limitations of the modelling are noted, followed by a discussion of the results of the experiments for the AIS, and an appraisal of the study implications in the context of other related research.

The experiments in this study investigate the calving scenario from the geometry of an instantaneous retreat, and therefore the ice surface geometry is the same as the modelled steady state. Therefore, the calving front configuration is a straight cliff of thick ice which causes high strain at the calving front while in reality the calving front of the present day AIS tapers gradually. Another limitation of our simulations is that the coarse grid resolution that we employ (5 km, limited by available computing resources) may under-represent the strain deformation of ice at the calving front close to the grounding line or rifts. Ice sheet models are resolution dependent, therefore simulations at finer resolution would be able to capture the migration of the grounding line and strain where the ice starts to deform due to fractures. The role of marine ice is not explored in this study, although it is known to affect the stability of ice shelves (Holland et al., 2009; Craven et al., 2009b; Galton-Fenzi et al., 2012; Kulessa et al., 2014) and is present on the western AIS (Treverrow et al., 2010). Incorporating marine ice in a model could change the strain along the western part of the AIS resulting in different calving front geometries. Further, the AIS is known to exhibit significant surface melt, suggesting that hydrofracturing mechanisms (not included in the present study) could potentially reduce ice shelf stability in the future (Alley et al., 2018; Lai et al., 2020).

Passive stable ice occurs, for the models in this study, upstream from pinning points, as in the case for retreat geometries M1 and M2. The pinning points near the calving front of the AIS (see Chapter 2) contribute shear resistance and buttressing that mitigate ice flow (Gladstone et al., 2012; Fürst et al., 2015; Berger et al., 2016). In more detail, the M1 calving front sits

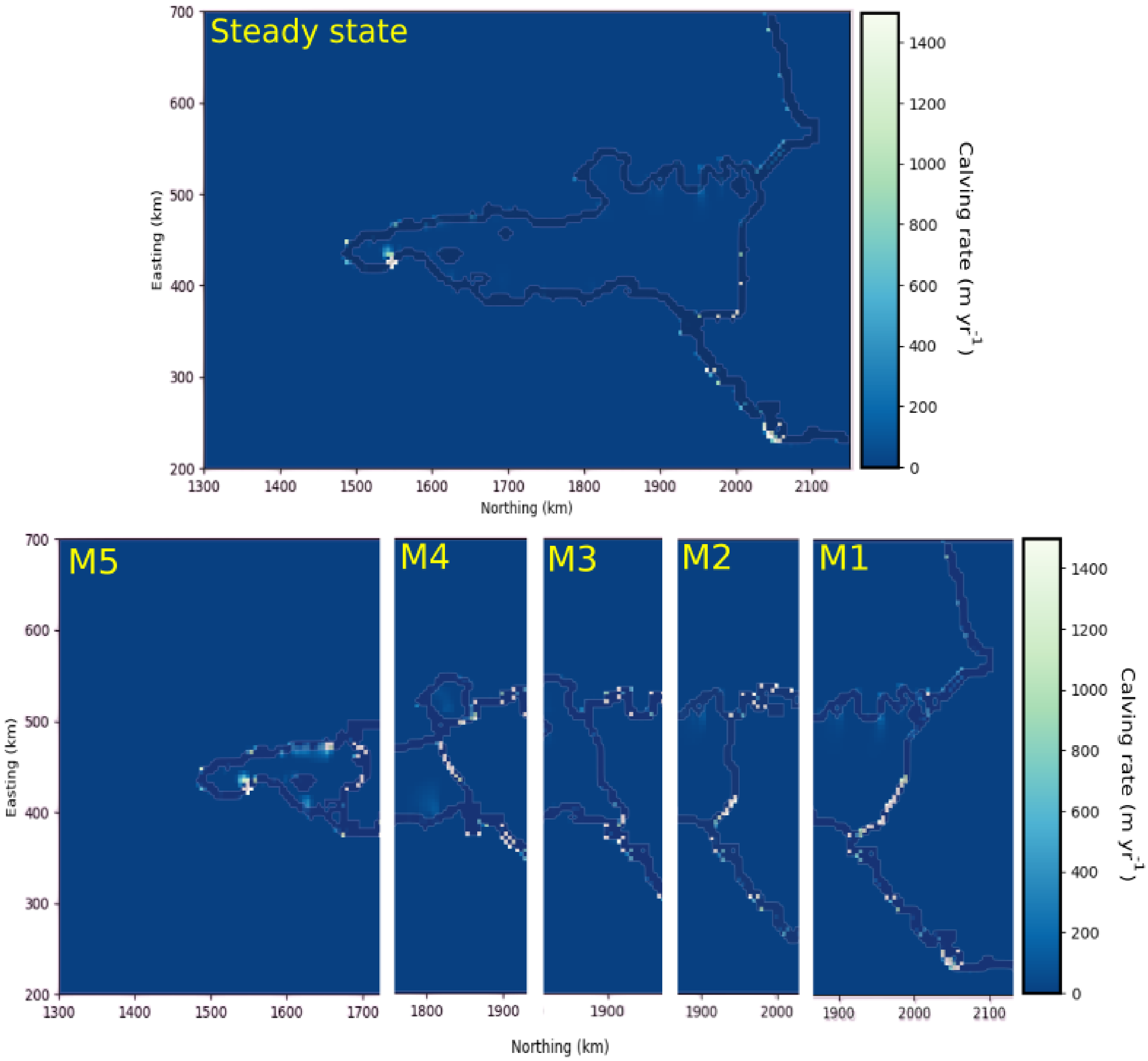

Figure 3.9: Calving rates are calculated only at the calving front according to the method of Levermann et al. (2012) for each simulated model calving front geometry (Figures 3.3 and 3.4).

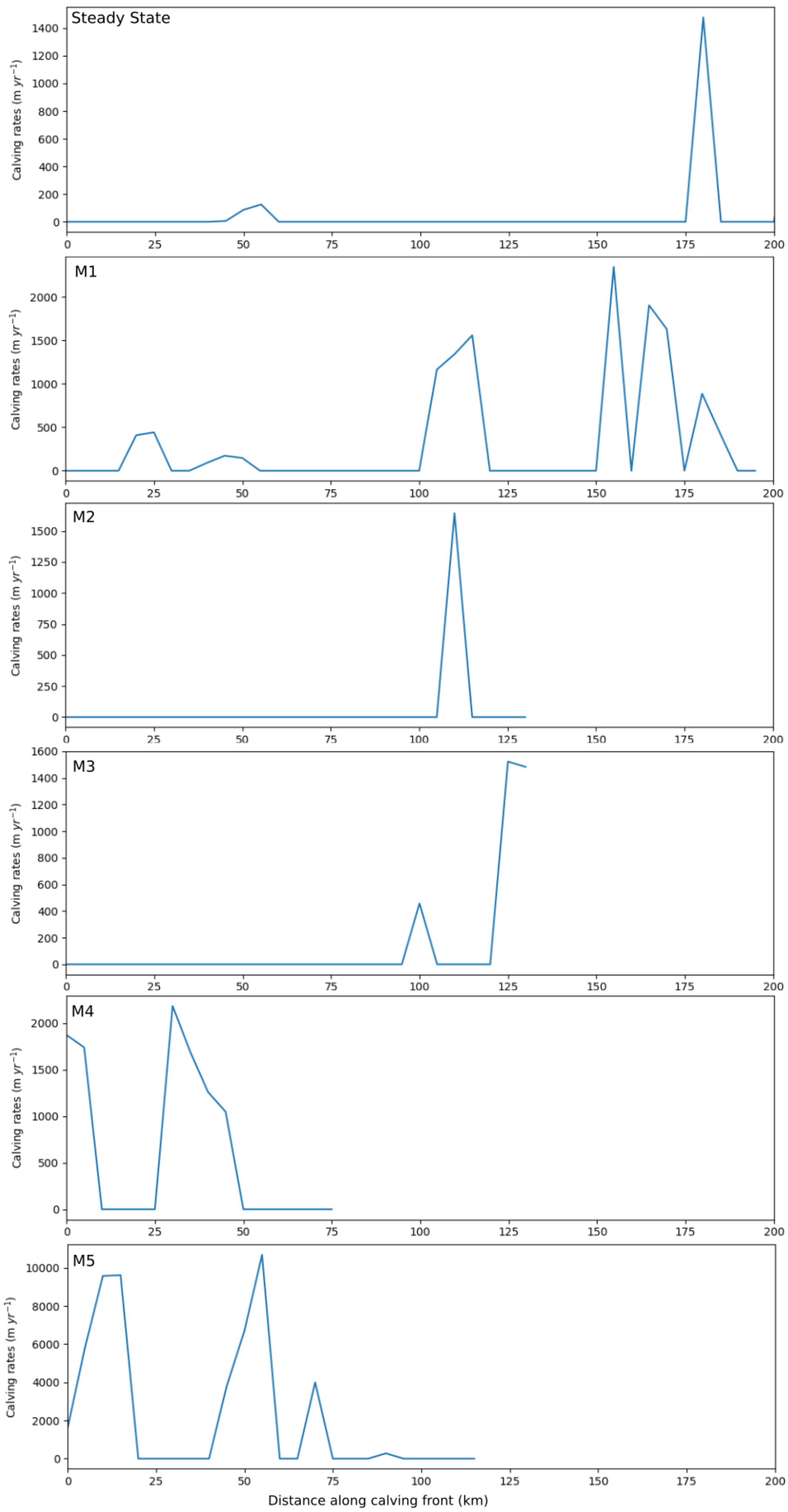

Figure 3.10: Calving rates as calculated at the calving front for steady state and the simulated model calving front geometry (Figure 3.9). Distance (x axis) is given from the coastal grounding line, and runs across the simulated ice front from west to east (upper to lower) in previous figure.

upstream from the Triangle pinning point, and there is a corresponding increase in velocity on the eastern side of the ice shelf (Figure 3.6). The M2 calving front is upstream of both Podlednyj holm (west) and Triangle (east) pinning points, and the velocity increases across the entire M2 ice front. The progressive increase in velocity at the calving front from M1 to M2 appears not to be sufficient to result in a sudden discharge of ice over the grounding line (Table 3.2), which suggests that a retreat of the calving front of 85 km would not lead directly to ice shelf collapse. However, the significant speed-up of velocity at the ice front of geometry M3 indicates that the threshold of passive ice has been exceeded. The increase in velocity at the ice front extends to the inlets of Charybdis and Scylla Glaciers, which would cause more influx of grounded ice from the upstream region. The deep ice at the south of the AIS does not show a significant increase in velocity until the M5 calving trajectory suggesting that a substantial retreat would have to occur to significantly increase the flux of grounded ice into the ocean.

The areal extent of passive ice from our results on the eastern part of the AIS is similar to Fürst et al. (2016) but on the western part of the AIS our results show more passive ice coverage. The bedrock boundary used in our study incorporates the pinning points (Podlednyj holm and Triangle) from Matsuoka et al. (2015) while the study by Fürst et al. (2016) used the BEDMAP2 dataset of Fretwell et al. (2013) who did not include the pinning points near the calving front of AIS. The inclusion of the pinning points suggests the mechanism for holding slightly more passive ice on the western part of the AIS in our results. Further, the region between M1 and M2, appears to be an intermediate case, i.e. not true passive ice: the ungrounding from Podlednyj holm has a noticable effect upstream, however, not to the extent of causing an extreme change in ice shelf dynamics. This is likely to be due to the region between Podlednyj holm and the embayment where the tributary (Charybdis and Scylla) glaciers join the AIS contributing some shear resistance.

A comparison of modelled ice shelf results is shown in Figure 3.11. The 2$^{\text{nd}}$ principal strain rate criterion suggests that a stable situation would result across the calving front of model geometries M1-M3 of AIS (Figure 3.7) becoming unstable for the calving front model geometry of M4. Geometry M5 also shows a stable system due to the presence of high magnitude compressed 2$^{\text{nd}}$ principal strain rate on the remnant ice shelf (Figure 3.7, M5). This criterion appears to show a stable state related to the lateral resistance to the ice flow from the sides of the narrow channel walls (M2,M3, M5). According to the strain-flow criterion, geometry M1 is likely to be stable (in agreement with the previous criterion), however, the low strain-flow angle for the western part of the calving front for geometry M2 more logically responds to the ungrounding from the pinning point. The strain-flow criterion for geometries M3 and M4 suggests both these geometries may be unstable and vulnerable to irreversible retreat. However, the physics of the mechanism proposed by Kulessa et al. (2014) and Jansen et al. (2015) is based on fractures, such as rifts and crevasses, which are orthogonal to ice flow only

(Bassis and Jacobs, 2013), whereas the AIS also exhibits rifting parallel to flow.

According to calving rates calculated by the method of Levermann et al. (2012), geometry M1 shows the likelihood of retreat in the eastern side of the AIF, which progressively decreases in magnitude and areal extent for geometries M2 and M3. Calving rates are negligible across the calving front of M3, but initially the AIF retreats further upstream if the calving front is calved upstream of pinning points. This transition likely occurs due to the configuration of M3 not being a stable system and would likely cause re-advancement of the remnant ice shelf if no further changes were to occur. M4 shows a strong likelihood of retreat, noting that both the above stability criteria investigations showed this retreat location to be unstable. In the extreme case, where the calving front is position as in geometry M5, then the AIS will likely undergo irreversible retreat due to decreased buttressing by the remnant ice shelf. Interestingly, the above ice shelf stability criteria (Doake et al., 1998; Kulessa et al., 2014; Jansen et al., 2015) predicted that this system would be stable for a retreated calving front with geometry M5 but calving rate values indicate a high retreat rate nearly across the whole remnant ice shelf.

Our findings add to the modelling study of Gong et al. (2014), who explored the AIS using the BISICLES framework, showing a thinning ice shelf in response to climate forcings. Results from both studies show that removal or thinning of ice does not cause significant changes to the ice dynamics at the deep grounding line. Both studies therefore suggest that a retreated calving front to geometries M1 and M2 would likely contribute negligibly to sea-level changes. Similarly, Pittard et al. (2017) also find, using the PISM model, that the LAGS is relatively stable with regard to significant ice mass loss under a range of warming scenarios.

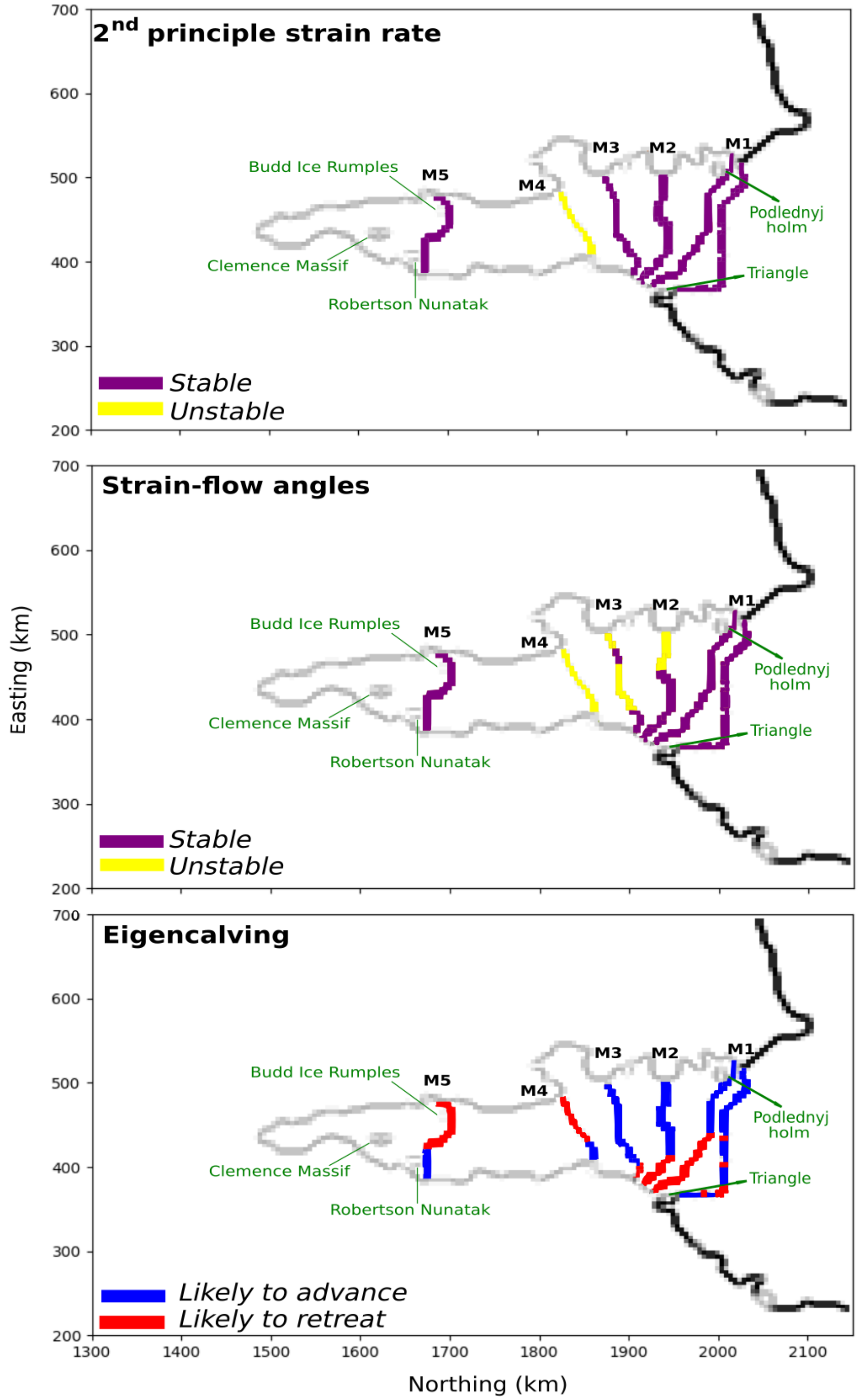

Figure 3.11: A comparison of the results using different methods. The upper panel (Experiment 2) shows results following the method of Doake et al. (1998), the middle panel (Experiment 3) shows results from the method of Kulessa et al. (2014) and Jansen et al. (2015). The lower panel (Experiment 4) shows the ice front calving rate (Levermann et al., 2012).

3.6 Conclusion

Numerical modelling results are presented, using the Parallel Ice Sheet Model, of the AIS under different scenarios of ice shelf retreat. Five different retreat scenarios are imposed and changes in ice velocity, strain rate, strain-flow angle and calving rate are investigated. These variables are assessed to understand the dynamic changes on the ice shelf for each retreat scenario. Our results identify sections of the ice front where ice removal does not cause a speed-up of the ice flow at the calving front. This area of passive ice is slightly larger than identified in previous studies of the AIS, and this is probably due to the presence of small-scale pinning points near the calving front (Podlednyj holm and Triangle) which were previously neglected. Our results indicate that that a region of ice that provides some resistance to flow extends a considerable distance upstream in the AIS, responding more actively to ice removal closer to where the tributary Scylla and Charybdis Glaciers join the main AIS.

Two criteria for ice shelf stability were tested based on strain rate, and strain-flow angle, and produced somewhat different results as to which retreat scenarios could cause the AIS to disintegrate. The strain rate criterion implies that the AIS would remain stable in the case of more severe retreat than the strain-flow angle criterion. Taken together the studies suggest that the AIS would be stable for a retreat of approximately 85 km upstream of the current calving front, and a retreat up to this point might result in a re-advance of the remnant ice shelf. Geometries with a retreat of less than 85 km reveal little change in the velocity of the ice at the deep grounding line, indicating negligible contribution to sea-level change from the AIS till the calving front position retreats more than 85 km further south. Results from all methods agree that a retreat position of greater than 160 km would result in an unstable AIS, which would be likely to undergo further retreat. The most extreme retreat scenario tested, approximately 280 km, close to the ice rise of Robertson Nunatak, shows greater stability than the intermediate geometries, but the likelihood of continued retreat by calving.

The approach of maintaining the same ice surface geometry for each retreat scenario, and employing a hybrid ice sheet model rather than a Full Stokes Equation ice sheet model, produces some uncertainty in the modelled results since it cannot capture the full stress regime of the AIS. Nonetheless, our results reveal the importance of the geometry of the coastal region which is an input needed in all ice sheet models. We also find that the previous criteria of ice shelf stability show some inconsistency in results for the AIS. This highlights the need for high-resolution bathymetry data sets, and further exploration of the heterogeneity of ice, to be able to project calving rates and sea-level changes from the AIS.

Chapter 4

The impact of basal melt and refreezing on the modelling of the Amery Ice Shelf

Abstract

The Lambert-Amery Glacial System (LAGS), a major drainage basin of East Antarctica, is one of the largest glacial systems on Earth. The area of the LAGS is $\sim$ 60,000 km^2, and it has the deepest grounding line of any ice shelf, 2500 m below sea level. The interface between ice and ocean at such a depth is dynamic, involving ice shelf evolution due to basal melt and refreezing underneath the base of the ice shelf. The extent of the net basal ice loss from the the Amery Ice Shelf (AIS) has been investigated using numerical ice sheet and ocean models but these and observational studies provide widely differing estimates of the mass balance. While there is much interest in the investigation of basal melt, the impact of choices within a model on patterns of melt and refreeze, and sensitivities in the resultant ice shelf system response have been less explored. Here we assess the response of the AIS to four different ice-ocean interface parameter combinations applied in the Parallel Ice Sheet Model (PISM). The experiments were carried out at 5 km horizontal resolution in two stages. First, ice-ocean interface parameterisations were tested in a diagnostic manner to assess their ability to reproduce basal melt and refreezing patterns from satellite-derived data. Second, the ice-ocean interface parameterisations were run over sufficient time to test their effect on grounding line position, calving front position, ice velocity, and ice thickness. Our experiments show that PISM's internal ice-ocean interface parameterisations do not reproduce basal melt and refreezing underneath the AIS as found in present-day observations. However, the the present day spatial pattern of basal melt on the eastern side of the AIS and in regions of deep ice near the southern grounding line, as well as notable refreezing on the western side of the calving

front of the AIS, could be reproduced by forcing the model with ice shelf melt rates from an ocean model. When the investigated parameter combinations were run over an extended time frame, the results showed the production of basal melt at the deep grounding line. For the AIS, this leads to little change in the position of the deep grounding line, but the modelled refreezing strongly influences the calving front profile. Our findings highlight the importance of the choice of ice-ocean interface parameters and, in particular, their effect on the basal melt spatial pattern. These differences would likely be amplified in longer simulations and could lead to over-estimation of predicted sea-level rise from the AIS.

4.1 Introduction

The ice shelves of Antarctica lose mass to the Southern Ocean through processes of calving and basal melt. The relative contribution of these mass loss processes in total is similar (basal melt being slightly higher) according to Depoorter et al. (2013), whereas Rignot et al. (2013) conclude that calving processes contribute more to the total. Both studies agree that calving processes are responsible for a greater proportion of mass loss from the Amery Ice Shelf (AIS) although basal melt is a significant contributor. The basal meltwater production of the Amery Ice Shelf (AIS) is comparable to that of the Ross Ice Shelf or the Filchner-Ronne Ice Shelf despite being smaller than both and accounting for only 2% of the East Antarctic coastline (Galton-Fenzi et al., 2012). The AIS has some of the deepest ice in Antarctica, $\sim$ 2500m below sea level at its deepest point. The high pressure at this depth lowers the local freezing point at the grounding line (Fricker et al., 2002a; Galton-Fenzi et al., 2008, 2012). The presence of ice at depth in contact with the ocean results in a significant ocean influence on the mass balance of the AIS (Adusumilli et al., 2018; Hindmarsh, 2006).

Basal melt is controlled mainly by intrusion of the Circumpolar Deep Water into the sub-ice shelf cavity (Holland et al., 2008; Galton-Fenzi et al., 2008, 2012), and by in situ hydrostatic pressure (Doake, 1976; Lewis and Perkin, 1986; Galton-Fenzi et al., 2012; Hoffman and Price, 2014). Basal melt from Circumpolar Deep Water is generated by incoming seawater, which melts the base of the ice shelf and consequently increases the flux of grounded ice to the ocean (Doake, 1976; Galton-Fenzi et al., 2012). The ocean temperature difference between the ambient ocean and the in situ freezing point creates a circulation of water, commonly known as an "ice-pump" (Lewis and Perkin, 1986). The water under the ice shelf close to the grounding line becomes buoyant as meltwater from the grounded ice mixes with the ambient water. This mixed water rises upwards and can draw heavier, warm sea water behind it. The mixed water cools as the local freezing temperature increases, and can freeze directly on the underside of the ice shelf base. The supercooling of the buoyant water under the ice shelf base creates frazil crystals (Galton-Fenzi et al., 2012) in the water column, leading to the formation of marine ice (Treverrow et al., 2010). Inferences from satellite radar and altimetry observations, and observations from drill hole campaigns investigating the AIS and ocean cavity below, show distinct areas of basal melting, and accretion of marine ice underneath the AIS (reviewed by Galton-Fenzi et al., 2012). Surface meltwater forms melt ponds that can be up to 3.5 km wide and 80 km long on the AIS surface (Phillips, 1998; Kingslake et al., 2017). These melt ponds mostly refreeze, or are absorbed into the firn layer, but could drain through crevasses or moulins to the subglacial hydrology system (Langley et al., 2016). Such crevasses contribute, for some ice shelves, to a process of hydrofracturing (Scambos et al., 2003) that accelerates ice shelf disintegration, with areas susceptible to such processes recently mapped on the basis of satellite images in a continent-wide study by Lai et al. (2020). Surface melt is not considered in this study, but is likely to become increasingly significant in a warming climate.

Recent studies show different estimates of net basal ice loss for the AIS, though it is believed to be in a steady state over multidecadal scales (King et al., 2007, 2009). Numerical modelling by Galton-Fenzi et al. (2012) predicts a net basal melt rate of 45.6 Gt year^{-1}, while an observational study using a combination of remote sensing data and in situ measurements (Wen et al., 2010) suggest either 51.5 $\pm$ 9.6 Gt year^{-1} or 46.4 $\pm$ 6.9 Gt year^{-1} depending on the adopted methodology. Yu et al. (2010) investigated the full LAGS catchment using combined SAR interferometry and texture information from MODIS imagery (to refine the position of the grounding line), calculating a net basal melt rate of 27 $\pm$ 7 Gt year^{-1}. The difference between studies using remote sensing data may be due to the adoption of different flux estimates at the AIS grounding line (Yu et al., 2010). Frazil crystal accretion in the western part of the AIS front is considered in the numerical modelling by Galton-Fenzi et al. (2012) but is not considered in the observational studies noted above. Additionally, regional variations in the mass balance of the AIS (Yu et al., 2010) and artefacts or gaps in the satellite data due to decreased track densities of satellites at (relatively) northerly latitudes (Adusumilli et al., 2018) can also contribute to discrepancies in results.

Herein we use a numerical ice sheet model to explore the sensitivity of the AIS to different ice-ocean interface parameters, sub-shelf ice temperature and sub-shelf melt rate, to answer the following questions:

- How well do PISM's internal ice-ocean interface model options, and alternative inputs from three-dimensional ocean models, reproduce the observed magnitude and spatial variability of basal melt and refreeze for the AIS?
- Does the choice of ice-ocean interface parameters affect the geometry (grounding line position, calving front position, ice thickness) and velocity of the AIS?

We carried out numerical experiments, using PISM, with four different ice-ocean interface parameter combinations (IOPs) as input to a modelled steady state representing the present

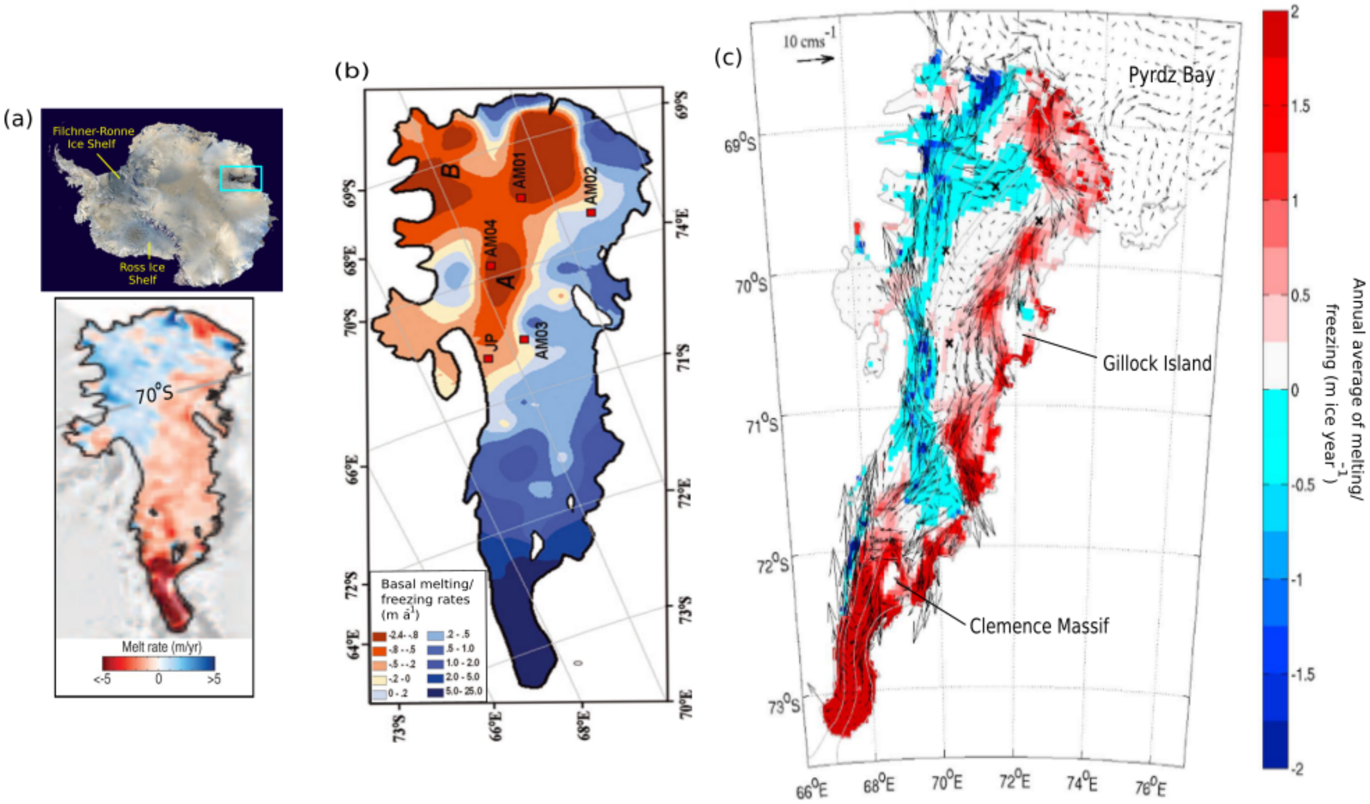

Figure 4.1: Estimates of Amery Ice Shelf basal melt and freeze rates. The top panel of (a) shows the Amery Ice Shelf region in Antarctica, and the lower panel depicts basal melting >-5 m year^{-1} (red) to freezing <+5 m year^{-1} (blue; reproduced from Rignot et al., 2013), (b) Spatial distribution of basal melt/freeze where ranges of red colours show basal freezing and ranges of blue colours show basal melting areas (noting the reversed colour scale, reproduced from Wen et al., 2010), (c) The annual averaged pattern of basal melting (positive, red) and freezing (negative, blue) superimposed with depth average currents (reproduced from Galton-Fenzi et al., 2012).

day LAGS. Our experiments firstly test the influence of each IOP on the predicted pattern of basal melt and refreezing underneath the AIS. Secondly, we investigate how the choice of IOP impacts the response of the AIS to forcing over time. In our assessment of results, we make comparisons to present day observations, as a consistent point of reference.

4.2 Methods and Data

4.2.1 *Parallel Ice Sheet Model (PISM)*

PISM Version 0.7.3 is a 3D, thermomechanically-coupled hybrid ice sheet model (PISM: User's Manual available at www.pism-docs.org) (Bueler et al., 2007; Bueler and Brown, 2009; Winkelmann et al., 2011; Martin et al., 2011). The hybrid model superposes both the shallow ice approximation (SIA), and shallow shelf approximation (SSA). The SIA is a 'zero-order' model which computes the dynamics of grounded ice where there is negligible basal velocity, whereas the SSA solves the ice dynamics in regions where basal shear stress is zero, and longitudinal stresses dominate. The SIA and SSA horizontal velocities are computed in the whole continental domain, where transition from one to another is calculated by a weighting function for a continuous smooth transition from the SIA across the grounding line to the SSA (Bueler and Brown, 2009).

The ice rheology is given by the Glen-Paterson-Budd-Lliboutry-Duval flow law (Paterson and Budd, 1982; Lliboutry and Duval, 1985; Aschwanden et al., 2013). PISM employs an enthalpy-based energy conservation scheme (Aschwanden et al., 2012) where ice flow is coupled to the temperature of the ice. The annual mean surface temperature (RACMO2.3/ANT27, 1979-2014, Van Wessem et al., 2014) and geothermal heat flux (An et al., 2015) are provided as boundary conditions for the advection and vertical conduction of heat through the grounded ice layers, while pressure melting temperature is also needed in the case of ice shelves as a boundary condition (Winkelmann et al., 2011). The bedrock is regarded as rigid, impenetrable, and parallel to the basal shear stress and basal sliding velocity. A pseudo-plastic power law relates basal shear stress and velocity at the ice-bed interface, and a quotient in the pseudo-plastic sliding law (q) is used to control the basal strength assuming that there is a layer of till underlying the grounded ice (Winkelmann et al., 2011; Bueler and Brown, 2009).

The spatial location of ice streams is calculated from the yield stress, which is dependent on a subglacial hydrology model (Aschwanden et al., 2012, 2016) and the modelled till strength, which is a function of bed elevation (Martin et al., 2011; Winkelmann et al., 2011; Aschwanden et al., 2016). We use a default hydrology model where water is not conserved but it is stored locally in the till up to 2 m, and any amount higher than this maximum value is lost with no feedback. The stress boundary condition at the calving front is calculated from the mass continuity equation and the geometry. Horizontal strain rates are used to calculate the caving rate (Levermann et al., 2012) in combination with a prescribed minimum ice thickness of the ice front.

4.2.2 *Initialisation*

To initialise the simulations, PISM requires boundary and forcing conditions. Bed topography from Fretwell et al. (2013) is stitched to a modified bathymetry around the southern-most part of the GL (Galton-Fenzi et al., 2008; Timmermann et al., 2010) including synthetic representation of Podlednyj holm and Triangle pinning points at the calving front(Matsuoka et al., 2015, full description in Chapter 2). The ice thickness is also taken from Fretwell et al. (2013).

Forcing conditions for the atmosphere are present day spatially distributed near-surface air temperatures, and precipitation (RACMO2.3/ANT27, 1979-2014 (yearly averaged), Van Wessem et al., 2014). The surface mass balance is computed from input data of precipitation and near-surface air temperature (RACMO2.3/ANT27, years 1979-2014, Van Wessem et al., 2014). The air temperature is used to calculate the energy available to melt ice at the ice surface interface by employing a positive degree-day (PDD) model (Aschwanden et al., 2013; Seguinot et al., 2014). PDD is defined as the integral of temperatures above 0 ° C in one year which in our case is between 0.37 K and 8.36 K. The lapse rate (8.0 K km^{-1}) applied to the 2 m air temperature forcings serves as the boundary condition for the conservation of energy equation which corrects the differences between the fixed surface ice elevation and the time evolving modelled elevation (Aschwanden et al., 2013; Seguinot et al., 2014).

As for oceanic forcing, the ocean's potential temperature (271.3 K) and adjacent ocean salinity (27.0 g/kg) were used to initialise basal melt at the ice-ocean boundary layer (www.pism-docs.org). These values were obtained by tuning the ocean forcing values for the whole Antarctic continent along with PISM tunable parameters (Table 4.1) that were generated in a 50 member ensemble by Latin hypercube (Santner et al., 2003, full description in Chapter 1). All the simulations were performed in a computational box where the maximum height of the domain is kept at 5000 m for ice thickness, the thinnest ice layer has a model dimension of 71.875 m while the thickest layer is 428.125 m. The geometry of the domain is a modified bathymetry as noted above.

4.2.3 *Spin-up*

The boundary conditions that were used as inputs in a multi-stage spin-up procedure at 10 km horizontal resolution were taken from present day climatology data as described in Section 4.2.2 (Galton-Fenzi et al., 2008; Timmermann et al., 2010; Fretwell et al., 2013; Van Wessem et al., 2014; An et al., 2015). Simulations at coarse resolution do not always resolve ice dynamics well, but enable multiple simulations to be run within reasonable computational time and resources. For the first stage, the present day climatology data were read in and the resolution of the simulation was specified. In the first and second stages, only the SIA stress was applied. The second stage simulation was run for 100 years to smooth out the stress peaks arising from ice surface roughness. The output of this stage is used as input for the next stage where the geometry was held fixed to allow the thermal evolution of the ice mass over 250,000 years. In the last stage, the full physics of the model was applied, such as the parameters that govern the dynamics of ice, hydrology, basal sliding, and calving at the ice front. In this stage the geometry was allowed to evolve freely until it reached a steady state with a good match to the present day AIS (Rignot et al., 2013; Fretwell et al., 2013), in particular, the location of the grounding line, ice thickness and ice velocity. With those criteria satisfied to an acceptable degree, the steady state is judged to have been achieved when the time series of ice volume with respect to time levels out (Bueler and Brown, 2009; Pittard, 2016).

The steady state model at 10 km horizontal resolution was then regridded to a 5 km horizontal resolution simulation where the evolving mass and energy state variables were interpolated from the coarse grid. The change in grid size required a further relaxation to steady state for 38,000 years. The steady state from the 5 km resolution was then adopted as the modelled state used for the investigation of the response to the four IOPs.

4.2.4 *Ice-ocean interface parameter combinations*

PISM provides multiple different approaches to modelling the ice-ocean interface beneath the ice shelf, either within the modelling environment or through the ability to take external datasets as input. Two boundary conditions are varied in this study: sub-shelf ocean temperature and sub-shelf melt rate. We use four different parameter combinations (IOPs) and compare their ability to reproduce the basal melt rates presented in Rignot et al. (2013) and their impact on the AIS evolution. The four parameter combinations are denoted: IOP-1 (const), IOP-2 (pressure_melt), IOP-3 (temp_flux), and IOP-4 (temp_salt) and are described below.

- ***IOP-1, const*:** In this default parameter combination for PISM, the boundary conditions are kept constant at the ice-ocean interface. The sub-shelf ice temperature is set to the pressure melting temperature for that elevation (depth), and the sub-shelf melt rate is fixed at 0.0519 m year^{-1}. In this parameter combination, the sub-shelf ice temperature does not influence the sub-shelf melt rate, and is used to calculate the ice temperature profile only.

- ***IOP-2, pressure_melt*:** This combination makes use of non-default options within the PISM framework. The sub-ice shelf ocean temperature, T_o, is set to a constant value of -1.7 °C (Winkelmann et al., 2011; Martin et al., 2011). The melt rate is calculated

Parameter	Value	Description
sia_e (unitless)	2.7	Enhancement factor for grounded ice where vertical shear dominates.
ssa_e (unitless)	1.8	Enhancement factor for floating ice where horizontal shear dominates.
q (unitless)	0.8	Exponent in pseudo-plastic flow law.
till (unitless)	0.01	A tuning parameter of the effective pressure of ice against pressurised water in the till.
ϕ (unitless)	10.0, 25.9, -760.0, 1279.0	Tuning of till strength depending on bed elevation. It varies the strength of the basal resistance by setting till friction angle as a function of bed elevation, i.e at -760 m bedrock depth till angle is 10.0°, and when bedrock depth goes to 1279 m, till angle is 25.9°
K (m s)	2.0e+16	A constant relating calving rate to principal strain rates (Levermann et al., 2012).
thk (m)	230.0	Constant thickness limit where ice below this thickness is calved from the ice front of an ice shelf

Table 4.1: Parameter choices.

using

$$\text{melt rate} = Q_{heat}/(L * \rho_i), \tag{4.1}$$

measured in m year^{-1}, where Q_{heat} is the net ocean heat flux into the ice (0.5 W m^{-2}), L is latent heat (3.34×10^5 J kg^{-1}), and ρ_i is density of ice (910.0 kg m^{-3}). The heat flux between the ambient ocean (of a given temperature and salinity) and ice is calculated using

$$Q_{heat} = \rho_o c_{po} \gamma_T F_{melt} (T_o - T_f), \tag{4.2}$$

where ρ_o is the density of ocean water at the given salinity, c_{po} is the specific heat capacity of the mixed ocean layer (3974.0 J K^{-1} kg^{-1}), γ_T is the thermal exchange velocity (1.00e-4 m s^{-1}), and T_f is the freezing temperature of the ocean of a given salinity at the elevation of the ice shelf base (details provided by Martin et al., 2011).

F_{melt} is a model parameter that requires tuning to match the present position of the grounding line and the spatially-observed melt rate as closely as possible. Five simulations were carried out to determine an appropriate value as $F_{melt} = 0.018$ (unitless) based on a match to present day observations (Rignot et al., 2013). This gives basal melt of the right order, and the areal extent of the predicted basal melt is somewhat closer to observations than other values tested.

- ***IOP-3, temp_flux*:** This parameter combination makes use of the ability to supply input boundary conditions to PISM from an external source. Sub-shelf ice temperature (Kelvin) and sub-shelf mass flux (kg $m^{-2}s^{-1}$) are prescribed from an ocean cavity model. We use average model outputs from a 20 year run of the Regional Ocean Modeling System (ROMS) three-dimensional numerical ocean model forced with seasonal climatology but no interannual variations (Galton-Fenzi et al., 2012). As with IOP-1, the sub-shelf ice temperature does not influence the sub-shelf melt rate, and is used to calculate the ice temperature profile only.

- ***IOP-4, temp_salt*:** In this case, we once again use Equations 4.1 and 4.2 to calculate basal melt rates, but this time the potential ocean temperature (T_o) and the salinity of the adjacent ocean at the ice-ocean interface are taken from the ROMS model of the AIS ocean cavity (Galton-Fenzi et al., 2012).

For the model initialisation (described previously in Section 4.2.2), in the case of IOP-1 and IOP-2, the ocean's potential temperature and adjacent ocean salinity were chosen based on a whole-of-Antarctica tuning to initialise the basal melt at the ice-ocean boundary layer for spin-up (Section 4.2.3). In the case of IOP-3 and IOP-4 the ocean's potential temperature and adjacent salinity were taken from ROMS focussed on the Amery region (Galton-Fenzi et al., 2012, Figure 4.1c).

4.2.5 *Experimental design*

These experiments are designed to assess the (a) ability of PISM to produce basal melt and refreezing close to present day satellite-derived values in terms of its magnitude and spatial pattern, and (b) the impact of the choice of IOP combination on the modelled response of the AIS.

- ***Experiment 1*:** The first experiment set was run as a diagnostic simulation, for one year, for each of the four different IOP combinations to compare the modelled basal melt/refreezing to present-day observations.

- ***Experiment 2*:** The second experiment set consisted of simulations for 200 one year time steps, with temporally-constant forcing data. Note that this is not intended to represent a direct prediction for the AIS over that time. The runtime of the simulations was chosen to give clearly sufficient iterations to infer sensitivity in the model response for the AIS, while keeping the cavity shape close to its present day geometry. A change in the cavity shape would significantly impact the predicted basal melt underneath the AIS and would hence make it difficult to compare the influence of the chosen IOP on the modelled response of the AIS as intended.

4.3 Results

4.3.1 *Present day basal melt and refreezing - Experiment 1*

The results of Experiment 1, investigating the basal melt modelled by PISM for the four IOP combinations, are summarised in Figure 4.2. A comparison of the modelled basal melt pattern with the observed values of Rignot et al. (2013), Figure 4.1, shows the following: IOP-1 represents a trival case for this diagnositic numerical experiment since the basal melt is fixed at a low, positive value (Figure 4.2a); the model that uses IOP-2 does not produce any refreezing for the one year time step (Figure 4.2b). In comparison to IOP-1, the IOP-2 combination results in a slightly higher basal melt at the southern, deep part of the grounding line, but neither is a close match to the observed melt-rates (comparison given below) nor the observed pattern of refreezing (Figure 4.1. Modelling using IOP-3 shows a melt-rate for the southern part of the AIS that is comparable to observed values, and also a zone of refreezing in the northwest part of the ice shelf although less in magnitude than observed (Figure 4.2c). Finally, the model using IOP-4 shows more extreme melt-rate values near the southern, deep part of the grounding line, but less refreezing in the northwest (Figure 4.2d), therefore, IOP-3 is the preferred combination based on this experiment.

Table 4.2 shows a simple, quantitative comparison of the spatial average basal melt-rate (m year $^{-1}$) of the AIS from each IOP tested in Experiment 1. The basal melt-rate for IOP-3 is 0.64 m year^{-1}, at the upper error bound of that calculated from observations by Rignot et al. (2013), which is 0.6 ± 0.4 m year^{-1} (Figure 4.1a, second panel), noting the large uncertainty of that estimate. IOP2 is also in agreement with observations in terms of the melt-rate, although the pattern of melt and refreezing is a better match to the model obtained using the IOP-3 combination.

Identifier	Melt rate
IOP-1	0.05
IOP-2	0.44
IOP-3	0.64
IOP-4	1.25

Table 4.2: Spatially-averaged basal melt production (m year $^{-1}$).

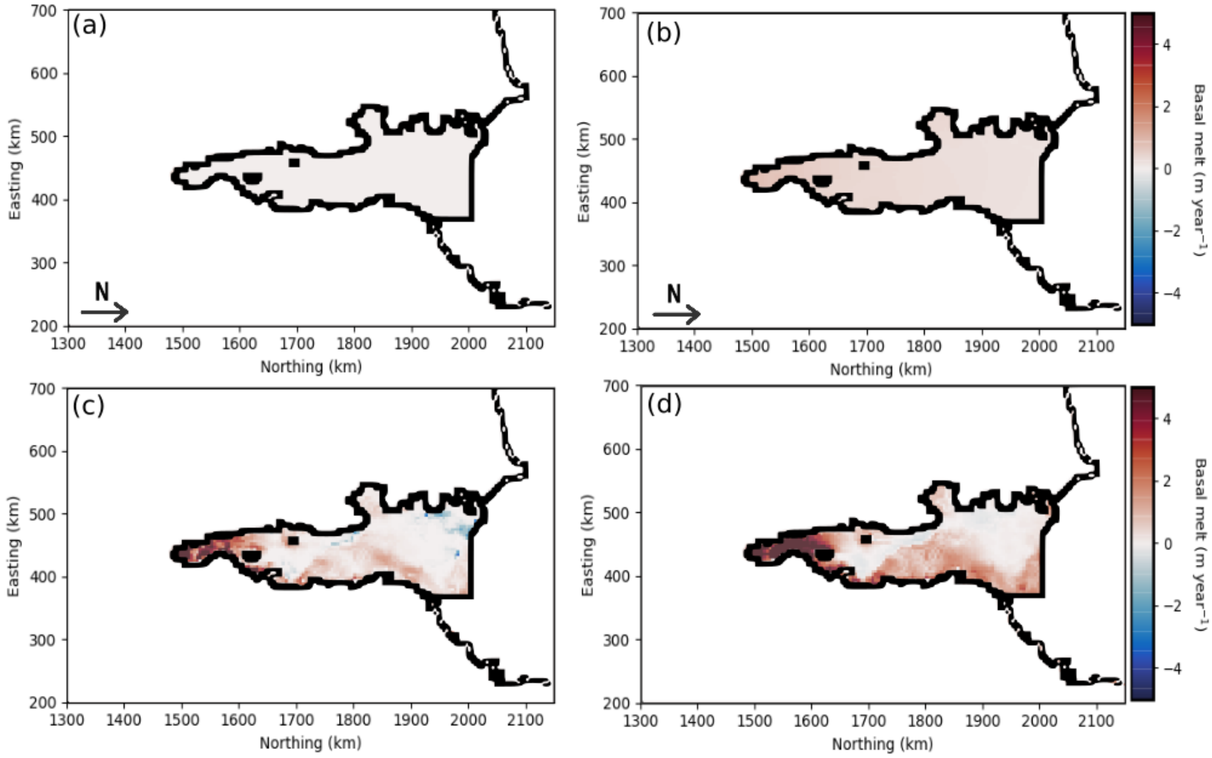

Figure 4.2: Basal melt-rate (red) and freeze-rate (blue) in m year^{-1} modelled using PISM with the ice-ocean parameter combinations detailed in Section 4.2.4: (a) IOP-1, (b) IOP-2, (c) IOP-3, and (d) IOP-4 for Experiment 1, a diagnostic run for a one year time step.

4.3.2 *Impact on AIS models - Experiment 2*

To analyse the impact of the different IOP combinations on the modelled response of the AIS, longer simulations were also carried out. Experiment 2 results were analysed to compare any migration of the grounding line and the ice front, and to compare the modelled basal melt-rate, the upper surface velocity, and the ice thickness after a prognostic, 200 year run. As explained above, the choice of run time allows for model response to be determined without invoking changes in the shape of the sub-ice cavity, hence retaining the focus of the experiments on the sensitivity to interface parameter choices. Since the basal melt-rate in IOP-1 was negligible this interface parameterisation was not carried forward to Experiment 2.

The response of the AIS, modelled using PISM with input combinations IOP-2, IOP-3 and IOP-4 is shown in Figure 4.3 and Figure 4.4, with a further quantitative comparison provided in Table 4.3. All three combinations resulted in little change in the grounding line in the south, with slight differences nearer to the calving front. IOP-3 predicted a slight advance and realignment of the ice front position with respect to the steady state position (Figure 4.3). IOP-2 and IOP-4 predicted a more retreated calving front when compared to IOP-3. This is consistent with the presence of refreezing in the northwest part of the AIS for IOP-3. IOP-4 show some refreezing in the northwest in Experiment 2, which appears to be negated by the much greater basal melt near the grounding line in terms of its affect on the ice front location.

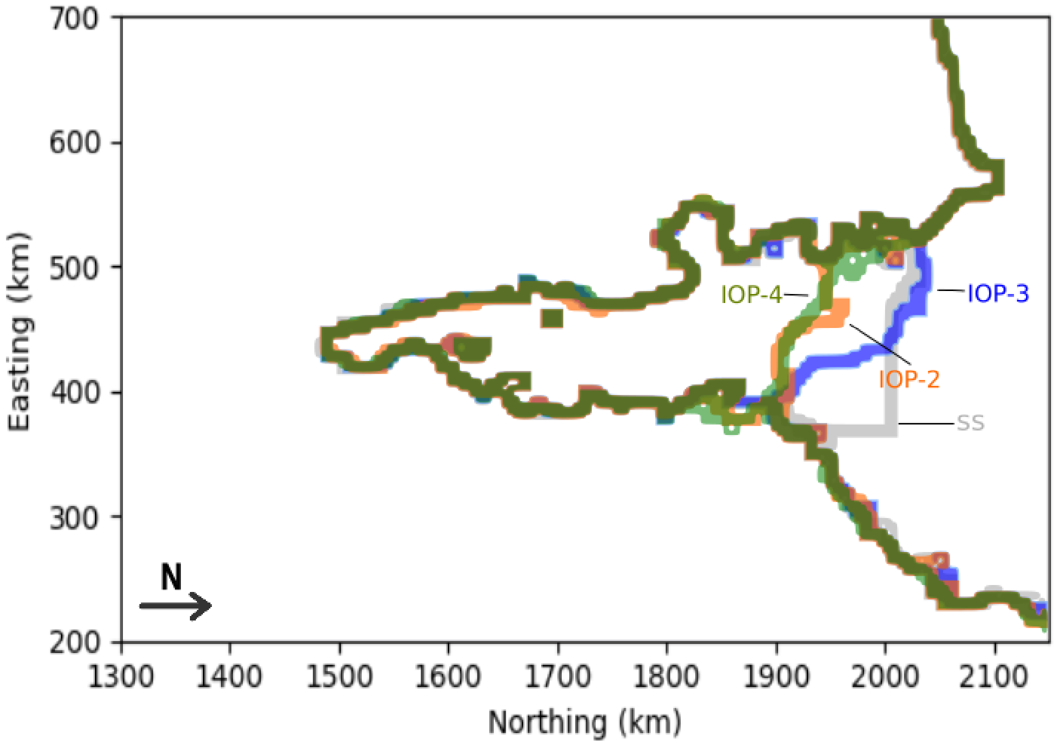

Figure 4.3: Grounding line and ice front positions modelled in PISM after a 200 year simulation (Experiment 2) using parameter combinations IOP-2 (pressure_melt, orange), IOP-3 (temp_flux, blue), and IOP-4 (temp_salt, green). The steady state (SS) model positions are indicated with a grey line as a reference.

Figure 4.4 (upper row) shows a pattern of basal melt resulting from the modelling using the IOP-2 combination that produces no refreezing and only limited basal melt in the southern most part of the ice shelf where the ice is deep. IOPs 3 and 4 display a high basal melt-rate in this location, with basal melt being very high when combination IOP-4 is employed (Figure 4.4g). Refreezing occurs in the model runs using combinations IOP-3 and IOP-4, but is more pronounced in IOP-3 in the northwest part of the ice shelf (Figure 4.4d). Hence, the IOP-3 combination remains the preferred choice for based on melt-rate pattern for the AIS after Experiment 2. The second row of Figure 4.4 shows the ice velocity for the three parameter combinations under test. The ice velocity difference (modelled - observed) when IOP-2 is used increases along the shelf and is the highest at the centre of the calving front. On the basis of the disparity between modelled and observed velocity, IOP-2 may be considered unsuitable for use in modelling the AIS. In contrast, the model runs that use IOP-3 and IOP-4 display a less severe progression of ice velocity difference from the south to the calving front of the AIS. The ice thickness is different for each IOP, with IOP-2 having thick ice in the southern part of the AIS while IOP-4 shows a larger negative ice thickness difference (modelled - observed) in comparison to IOP-2 and IOP-3. We quantified the ice thickness differences within the enclosed region (yellow box, Figure 4.4c) above the ice shelf cavity where the grounding line is deep.

Within this sample area, the ice thickness was predicted to be 15.9% and 9.7% higher than BEDMAP2 for IOP-2 and IOP-3 respectively, while IOP-4 had slighly less predicted ice than BEDMAP2 by 1%.

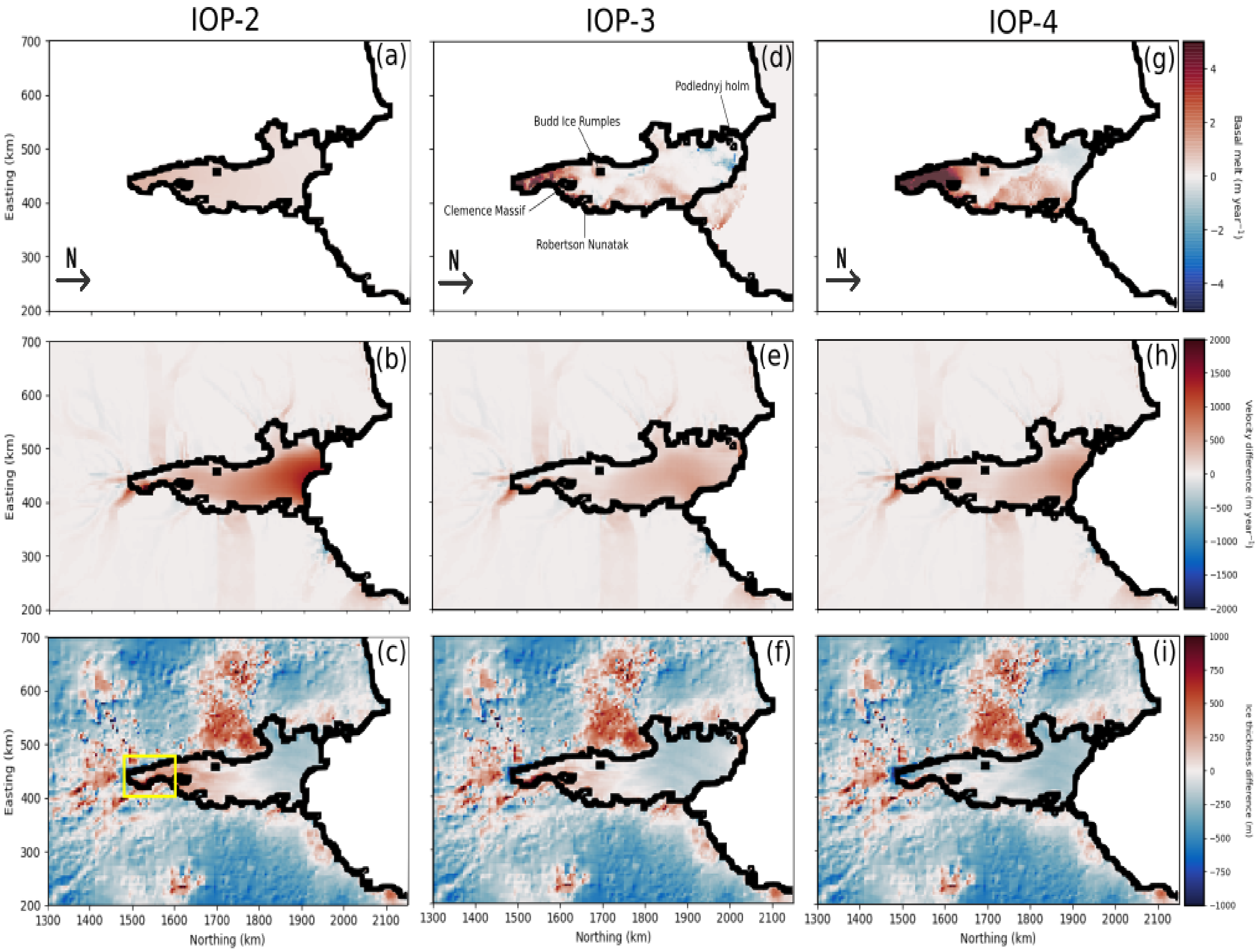

Figure 4.4: Upper row: the predicted basal melt-rate for IOP-2 (a), 3 (d) and 4 (g) at the end of a prognostic model run, over 200 years. Middle row: the upper ice velocity difference (modelled minus observed) for the three IOPs when compared with Rignot et al. (2011). Lower row: ice thickness difference (modelled minus observed) when compared with BEDMAP2 Fretwell et al. (2013). The change in ice thickness between the modelled results and BEDMAP2 was calculated within the enclosed yellow box (c).

As a final quantitative comparison, we calculate the average basal melt production of the AIS after a 200 year run (Table 4.3), which shows that IOP-3 melt-rates remain comparable to the estimated present day average basal melt-rate (0.6 ± 0.4 m year^{-1}; Rignot et al., 2013). Model runs using IOP-2 and IOP-4 have slightly high basal melt rates as IOP-2 has no refreezing and IOP-4 has weak refreezing at the calving front of the AIS.

Identifier	Melt rate
IOP-2	0.52
IOP-3	0.62
IOP-4	1.35

Table 4.3: Average basal melt-rate (m year $^{-1}$) of the AIS for the IOP combinations tested in Experiment 2, at the end of a 200 year run.

As a summary of findings resulting from the modelling in Experiments 1 and 2, IOP-1 is unsuitable due to a melt-rate that is too low, IOP-2 may be regarded as unsuitable based on the resulting AIS model showing an ice velocity that is too large, while IOP-4 is unsuitable due to the average basal melt-rate in the resulting model being too large. The combination of parameters used in IOP-3 is a good choice for both experiments, and across all the criteria used in the comparison with the observed AIS.

4.4 Discussion

In this section, the limitations of the study are noted followed by a discussion of the main findings. A comparison is then made with other investigations concerning the basal region of AIS and the modelling of basal melt of ice shelves more generally, including related software frameworks.

The experiments carried out in this study make use of an improved bathymetry geometry for the AIS that features pinning points close to the ice front (described in detail in Chapter 2). This bathymetry improves the response of the PISM model to forcing, enabling further experiments to be carried out to optimise model usage to refine this response. Hence, the underlying modelling framework in PISM on which this discussion is based has undergone considerable testing prior to the current set of simulations and can be considered robust for the consideration of basal melt. The present study makes a number of approximations that should be noted prior to analysis of the findings, most notably that the three-dimensional ocean model used as a boundary condition (for parameter combinations IOP-3 and IOP-4) is an averaged parameter set with no interannual variations. The subsequent utilisation of this model therefore implies temporally constant interface conditions, which is not strictly the case (Adusumilli et al., 2020). Running the experiment simulations over 200 one year time steps is not intended to make a prediction for a time 200 years from now, rather to explore the extent to which observables such as the ice front position and ice thickness are sensitive to differing basal melt inputs under current conditions of over a sufficient time frame. As noted previously, the present study does not consider the impact of a changing geometry of the sub-ice cavity. Such a study would require a coupled ocean-ice sheet approach and is the subject of current active development (Asay-Davis et al., 2016).

In the case of the AIS, Experiment 1 suggests that PISM's default ice-ocean interface parameterisation (IOP-1) and the simple melt parameterisation (IOP-2) cannot reproduce basal melt and refreezing rates that are comparable to present-day observations (Rignot et al., 2013). The upward movement of mixed water due to the deep ice close to the grounding line, and its subsequent refreezing in the northwest part of the ice shelf are needed considerations for refinement of the AIS response. IOP-4 makes use of a more detailed parameter combination for the ice-ocean interface and shows very high magnitudes of basal melt at the southern most part of the ice shelf near the deep ice of the grounding line, and refreezing rates at the western part of the calving front of the AIS that are lower than the result for IOP-3. This may be due to the approximation used in PISM where the ocean boundary transfer coefficients for heat and salt are held constant, rather than implementing ocean boundary transfer coefficients as a proportion of the friction velocity of the ocean; and/or the assumption of linear heat loss into the ice shelf that is proportional to the temperature gradient, calculated as the difference between the ocean temperature and the ice surface temperature (set at -20°C) over the ice thickness.

While IOP-4 attempts to incorporate more parameters, towards a better model, these proved less successful.

The introduction of ice-ocean boundary conditions based on the output of a three-dimensional ocean model, as tested in IOP-3, was the most successful combination, resulting in a similar spatial distribution of basal melting and refreezing to Rignot et al. (2013) and Wen et al. (2010), as shown in Figure 4.1a and 4.1b respectively). This represents a considerable improvement with the modelled average melt rate over the whole ice shelf being similar to the satellite-observed estimate of basal melt produced by Rignot et al. (2013), noting the high uncertainty although it is important to pay further consideration to the spatial pattern of melt.

Findings from Experiment 2 inform the understanding of how basal melt and refreezing would develop over a long time frame, given different input combinations. The basal melt produced by the use of the ocean input model, IOP-3, close to the southern part of the grounding line is also the most successful model run over a longer time frame with a reasonable match to observations. This result follows the general pattern around Antarctica, with the basal melt contribution to the ocean being highest in regions with deep ice (Silvano et al., 2016). In general this can result in grounding line migration and ice shelf thinning (Rignot and Jacobs, 2002). According to our tests, the grounding line position of the AIS does not show a strong tendency to migrate, although, the increased basal melting results in a reduction in ice thickness as shown in the lower row of Table 4.3.

The presence of refreezing, with a spatial pattern that shows strong refreezing in the northwest of the AIS is shown to be a key feature of the model using IOP-3 that leads to a realistic calving front position (Figure 4.4d). While IOP-4 also shows refreezing after running the model over time, the impact of the freezing for this parameter combination appears to be negated by the too-high basal melt near the southern part of the grounding line. In terms of modelled ice velocities, both IOP-3 and IOP-4 (Figure 4.4d and g) result in moderate ice velocities compared to IOP-2 (Figure 4.4 in spite of the basal melt in both IOPs being higher than in IOP-2. This points strongly to the importance of capturing refreezing near the calving front in understanding the response of the AIS. The ice thickness is larger at the grounding line for model runs using IOP-2 and IOP-3, compared to IOP-4, because melt rates are lower at that location. Refreezing at the calving front potentially increases buttressing and mitigates ice discharge. It is to be noted that the Podlednyj holm pinning point at the western calving front is present in all simulations.

In summary, refreezing underneath the AIS at the western part of the ice front significantly changes the calving front position and impacts the net basal mass loss of the AIS. This study is one of the first to investigate the use of an ocean model (IOP-3 and IOP-4: Galton-Fenzi et al., 2012) that includes frazil precipitation such that the impact of this freezing mechanism (Fricker et al., 2001; Treverrow et al., 2010; Wen et al., 2010) is effectively included.

Overall, the findings of this study suggest that numerical modelling of the AIS is not highly sensitive, with regard to grounding line position, or to ice-ocean interface inputs relating to basal melt. This finding is in common with the modelling study of Gong et al. (2014) looking at potential future climate forcing of the AIS using the BISCICLES framework. Correct basal melt at the deep grounding line is, however, needed to accurately model the pattern of melt and refreezing and our results suggest that this is a significant control on the position of the ice front. Where the ice front interacts with the sub-ice bathymetry, especially in the form of pinning points, this would likely impact the stability of the ice sheet.

Using ice-ocean interface parameter inputs based on a three-dimensional ocean model results in definite model improvements over parameterisations available as standard within PISM. In particular, the spatial pattern of basal melt and refreezing on the western side is captured with a reasonable match to AIS observations (Fricker et al., 2001; Craven et al., 2009b; Rignot et al., 2013). Further, this matches the well-understood mechanism noted by Rignot et al. (2013) that invokes "Coriolis-influenced transport and vertical mixing of ocean heat, the pressure dependence of the freezing point of seawater, and the sea floor and cavity morphology". On some large ice shelves, including the AIS, freezing is concentrated on the western sides, consistent with an oceanic circulation during which seawater is first cooled, freshened, and made more buoyant by melting (see also previous note regarding the inclusion of frazil precipitation). While the general pattern of basal melt near deep grounding lines, and refreeze near the calving front of major ice shelves is captured in a continent-wide modelling study by Reese et al. (2018a), the west-side assymmetry is not captured. This is likely due to the dominance of the pressure dependence variable that results in bands of decreasing melt rate towards the ice front from the grounding line. A study currently under review by Richter et al. (2020) aims at a similar understanding from the perspective of an Antartic-wide ocean model. Again, basal melt near the deep grounding line is captured in this study but refreeze and the assymetric west-east spatial pattern for the AIS are not reproduced.

In using ice sheet models to predict future mass loss for given drainage basins in Antarctica, our findings suggest that considering spatial patterns of basal melt rate and refreezing is of particular importance for the AIS, and also other ice shelves such as the Filchner that show strong west-east assymmetry. As a natural progression from regional studies such as that of Pittard et al. (2017) and continent-wide studies such as that of Golledge et al. (2015), we therefore recommend that three-dimensional ice-ocean interface models are utilized as inputs to PISM for such an ice shelf region or regions, and over longer time periods, a coupled ice-ocean approach should be considered. The estimated contribution of the AIS to future sea-level rise may be over-estimated in the absence of the temperature impacts of frazil precipitation (implicit or explicit) in modelling studies.

The results of this study are relevant to more sophisticated ice-ocean parameterisations such as the Potsdam Ice-shelf Cavity mOdel (PICO; Reese et al., 2018a), which has been built to work alongside PISM. PICO simulates the vertical overturning circulation in ice shelf cavities to capture the ocean circulation and estimate ocean-induced melting below ice shelves. When Reese et al. (2018a) applied this model to the whole Antarctic continent, the outputs showed a typical pattern of gradual bands of melting and refreezing along the AIS, which does not agree with the numerical findings of Galton-Fenzi et al. (2012), Figure 4.1c; or satellite observations as in Rignot et al. (2013), Figure 4.1a. The inaccurate spatial distribution of basal melt and refreezing under the AIS in PICO could have been caused by a number of potential limitations: (i) neglecting horizontal circulation of the ocean, (ii) neglecting the entrance of warm circumpolar deep water to the eastern part of the AIS and exiting of cool water along the western part of the AIS, and (iii) implementing constant turbulent salinity and temperature transfer rates. Additionally, the lack of a frazil precipitation model misses an important process for ice shelf dynamics in relation to the ocean, and will likely cause inaccurate calving front movement, and contribution to buttressing offered by refreezing. Though frazil precipitation may not be important for all ice shelves, for the AIS it is a very important dynamic oceanic process that generates a feedback loop between ice and ocean that likely contributes to the ice stability at the western calving front.

4.5 Conclusions

In this study, we used four individual ice-ocean interface parameter combinations to investigate the impact of such model parameterisation and parameter choices on the modelled basal melt rates of the Amery Ice Shelf (AIS). Numerical modelling experiments were carried out at 5 km resolution firstly to investigate the ability of the PISM ice sheet model to reproduce realistic basal melt for the AIS, and secondly to assess the impact of model choices relating to basal melt on the response of the AIS.

Our simulations show that the two internal ice-ocean interface parameterisations available within PISM (Version 0.7.3) do not reproduce the observed melt rate or refreezing of the AIS. The modelled melt rates are very low at the deep ice and on the eastern part of the ice shelf and the refreezing underneath the western part of the ice shelf, caused by mixed water rising and cooling down due to increasing local freezing temperature, is not replicated. However, using output from a three-dimensional ocean model to define conditions at the ice-ocean interface improved the modelled basal melt and refreezing pattern. This approach provides sufficient information to produce a reasonable match to the satellite-observed estimates of basal melt, both in terms of the average basal melt rate, and the spatial distribution of melt and refreeze.

A further set of simulations, run over 200 one year time steps, reinforces the importance of ice-ocean interface boundary conditions, with the input derived from the three-dimensional ocean model yielding the most realistic response of the AIS. Grounding line and ice front positions, ice velocity and ice thickness were all reasonably well matched to observations using this approach. The averaged basal melt rate produced using the ocean model input to the ice sheet model runs also showed a good match. The internal interface parameterisations available within PISM did not provide an acceptable modelled ice shelf response for the AIS.

Predictions of melt at a grounding line where the ice-ocean interface is deep are important for accurately modelling sea-level rise contributions in the short and long-term. Refreezing beneath the ice shelf enhances ice shelf stability, maintaining the position of the ice front, whereas basal melting thins and therefore destabilises the ice shelf. Therefore, studies which either neglect refreezing or under-estimate refreezing upstream of the western part of the calving front would predict a faster ice shelf retreat, overestimating future AIS mass loss.

Our results suggest that PISM may be used to model ice shelf response for ice shelves situated at the outlet glaciers with deep ice close to the grounding line provided that an ocean model derived ice-ocean interface parameterisation is used as input. Our findings are valid based on the assumption that the geometry of the sub-ice cavity and ocean current patterns are constant during the time frame of the simulation. Our study also shows the importance of basal melt-rate and refreezing patterns on ice sheet response and, by implication, confirms that initiatives that couple ocean forcing to ice dynamics are needed to progress the understanding of glacier systems such as the LAGS over longer time scales.

Chapter 5

Discussion and Conclusions

5.1 Main Findings

Ice shelves, as buttressing components of large glacier systems, are important in understanding the response of such systems to climate change as small changes in climatic conditions can result in significant changes to ice shelf stability. Uncertainties in the projected mass loss from Antarctic ice sheets is in part due to limitations in ice sheet modelling, which has led to widely varying predictions of sea-level rise (Patauri et al., 2014). The main findings of the research documented in this thesis contribute to a better understanding of the many factors that influence the modelled ice shelf response for the case of the Amery Ice Shelf (AIS) and hence the Lambert-Amery Glacial System (LAGS).

From 1968-1999, the AIS experienced no net change in velocity (King et al., 2007), and elevation change from 1968-2007 was near zero (King et al., 2009). This suggests the Lambert-Amery Glacier System (LAGS) has existed in a relatively stable state for multiple decades (King et al., 2007; Yu et al., 2010; King et al., 2012), which provides an excellent basis for initialising computational experiments. In Chapter 1, the use of a 3D, thermomechanically-coupled, hybrid ice sheet model, Parallel Ice Sheet Model (PISM) was introduced as the platform for numerical simulations. PISM requires climatology data sets as boundary conditions, which are used as inputs to initialise the model, with the model forced here by present day climatology. The geometry of the domain is allowed to evolve freely to establish glaciological parameters that result in a steady state. The stability of the LAGS enables the outputs of simulations to be considered in terms of their misfit with observations of ice shelf extent, ice thickness and surface velocity of ice collected over the recent decades without needing to consider their temporal variations, or that the ice shelf is in a transient configuration.

This thesis has documented the investigation of 1) the influence of the shape of the sub-ice shelf bathymetry on the AIS, and hence the LAGS; 2) the stability of the AIS under different retreat scenarios; and 3) the impact of different ice-ocean interface parameter combinations on the response of the AIS.

Bathymetry is an influential boundary in modelling experiments that impacts on ice velocity, ice flow pattern, and buttressing, and defines the geometry of the ice. Previous studies have shown that the inclusion of a deep sub-ice shelf cavity at the southern-most grounding line underneath the AIS in an ice sheet model improves the fit to the known present-day location of the grounding line (Fricker et al., 2002a; Galton-Fenzi et al., 2012; Fretwell et al., 2013). The objective of Chapter 2 was to explore the impact of different input bathymetry models on these aspects of the AIS, and hence the LAGS. Our experiments showed that the choice of bathymetry substantially impacts the modelled grounding line position with shallow bathymetries resulting in an advanced grounding line and calving front. In turn, this leads to inaccuracies in the modelled dynamics and stresses of the LAGS and AIS. In contrast, a bathymetry with a deep sub-ice cavity at the southern grounding line reproduces a grounding line position that is very close to observations. This consequently minimises the misfit between modelled and observed ice velocity and ice thickness of the LAGS. Chapter 2 also explored the addition of pinning points, and advanced understanding by showing that including small-scale pinning points near the present-day calving front of the AIS buttresses the flow at the ice front, slow down the ice velocity, and consequently increase ice surface elevation upstream. The modelling shows that this improves the fit of the model to the ice velocity across the grounding line. Adding the pinning points near the calving front also results in a modelled calving front closer in location to that of the present day. An under-sampled bathymetry could, in general, lead to undue emphasis on the tuning of modelling parameters that translate the physics from reality to a numerical model.

Having shown (in the first core research chapter, Chapter 2) that the AIS provides stability to the LAGS due to the buttressing effect imposed by the shelf on the grounded ice, the study documented in Chapter 3 of this thesis responded to the calving event of 2019 that was considered to have occurred earlier than expected (Francis et al., 2020). This study investigated the extent to which a significant retreat of the AIS calving front could decrease the buttressing effect, potentially increasing the contribution of the LAGS to sea-level rise through an increased flux of ice into the ocean. The objective of Chapter 3 was to to investigate the calving response of the AIS under different potential scenarios of retreat of the Amery ice front and assess the resulting impact on ice sheet stability. A range of potential calving front positions were constructed based along-flow strain rate contours of the ice shelf, and applied to a steady state model of the AIS. The study showed the extent of ice that could be removed without resulting in a significant acceleration of ice upstream, truly passive ice in front of the western pinning point, and ice with an intermediate degree of resistance to a change in ice shelf dynamics immediately behind. Two previously proposed approaches were used to determine the extent of ice shelf stability under the retreat scenarios tested, and the application of a calving law was also examined. Taken together, the approaches suggest that the AIS is stable (i.e. unlikely to undergo rapid further retreat) until it retreats to approximately 85 km upstream of the current calving front. Up to this point in the retreat there is little acceleration of the ice at the grounding line, meaning that the AIS can retreat substantially without contributing significantly to sea-level rise. For more extreme retreat scenarios, beyond the pinning points identified to be significant to ice dynamics in Chapter 2, the approaches gave mixed indications of ice shelf stability, with a suggestion that further retreat of the calving front could result.

A further factor that has an influence on the dynamics of an ice shelf is basal melt. For the AIS, basal melt is second to calving processes in being a major contributor to ice mass loss, but has significant mass loss through basal melt in comparison to much larger ice shelves. The objective of the research described in Chapter 4 was to investigate the different ice-ocean interface parameter combinations: internal options within PISM and supplied three-dimensional ocean models. The parameterisations were assessed on their ability to match observed rates of basal melt and refreezing under the AIS. Their impact on modelled grounding line position, ice front position, ice velocity and ice thickness was also examined. The results show that PISM's internal default interface parameterisation and a further simple melt parameterisation cannot reproduce high basal melt rates at the deep grounding line, nor refreezing on the western side of the calving front of the AIS. However, when pre-calculated sub-shelf melt rate data are taken from a regional numerical ocean model and used as input to PISM, then the modelled pattern of basal melt underneath the AIS is very close to present-day observations along with basal melt on the eastern side of the AIS due to intrusion of the warm Circumpolar Deep Water. A forward run of 200 one year time steps using three different ice-ocean interface parameterisations showed that the magnitude of basal melt at the deep grounding line significantly affects ice thickness, while refreezing influences the calving front position. This is possibly the first study of ice sheet response that incorporates a regional ocean model, implicitly considering mechnisms such as frazil precipitation. Previous studies (Pittard et al., 2017) have noted that the grounding line of the AIS is relatively stable with respect to climate forcing, and the present study suggests that the AIS gains further stability through the refreezing on the western side. This implies that ice mass loss from the AIS could be over-estimated in studies that do not include refreezing in the modelled ice shelf response.

As noted in the introduction, at the outset of this research, the decision to use the PISM computational framework for the numerical modelling and the use of a relatively large Antarctic domain were based on the potential extension of the modelling back to the last glacial maximum. This extended modelling proved impractical in the timeframe of a PhD candidature due to circumstances beyond the control of the author, and was also limited by unforeseen computing resource constraints. It is acknowledged, therefore, that some limitations in the presented work (e.g. model resolution) relate to a research context extending beyond the work described in this thesis. The main research findings, as outlined below, are nevertheless robust and may be taken forward in informing future research.

In summary, the main findings of the research described in this thesis are: 1) the importance to AIS dynamics of a bathymetry with a deep sub-ice cavity at the southern grounding line, and pinning points near the calving front; 2) the extent of ice that could be lost to the AIS without resulting in an unstable condition that could lead to an increased rate of ice mass loss; and 3) the importance to ice shelf stability and dynamics on the magnitude and spatial pattern of basal melt and refreezing. These findings add detail to the study by Pittard et al. (2017), which concluded the LAGS would be relatively stable to a range of future warming scenarios. The pinning points investigated in this research lend further stability to the AIS, and the extent of passive ice may be better understood as a result of the calving experiments of the present study. Further, the current pattern of refreezing confers further stability on the AIS provided the present day ice-ocean interface model remains valid.

The three core research chapters highlight important recommendations for future modelling studies of the AIS, and more generally: 1) to make use of a detailed bathymetry with attention to the area near the southern grounding line and all small pinning points at the calving front of the ice shelf; 2) consider multiple criteria in the assessment of ice shelf stability, as conclusions may differ depending on the approach employed; 3) make use of a three dimensional ocean model to define the ice-ocean boundary conditions, especially in the case of ice shelves with a distinct pattern of refreezing on the western flank.

5.2 Future Directions

Several potential areas of future research have emerged from research documented in this thesis:

- Simulations of the LAGS from the last glacial maximum to the present day.

  The LAGS shows sensitivity to the accuracy of bedrock elevation data sets and to pinning points, even of small-scale, beneath the AIS. Inclusion of accurate bedrock elevation data at the grounding line and ice front position would be expected to improve modelling results both for present day and, by implication, for paleo ice sheet simulations of the LAGS.

- Investigate ice shelf stability using a higher order model with better horizontal resolution.

  As noted in the previous section, the choice of using PISM as the modelling framework, the large continental modelling domain, and the consequent practical limitations in resolution were guided by a research context wider than the research included in this thesis. PISM does not include all nine principle stress components that describe the flow of ice, and the model resolution used (5 km) may have some impact on the representation of strain deformation along the ice shelf. Using a model, with adequately detailed bathymetry, that implements a regional Full Stokes Equation numerical ice sheet model at finer resolution would provide better knowledge of ice deformation, and better tracking of the migration of the grounding line when ice transitions from being grounded to floating.

  With regard to the research progressed in this thesis, the differing results in the second core chapter (Chapter 3; calving response) could be further explored. The experiments investigating ice shelf stability require simulation of multiple different geometries of an ice shelf that produce instantaneous dynamic changes in longitudinal stresses for ice streams, and vertical shear and sliding for grounded ice and across the grounding line. At fine resolution, small changes in ice dynamics near the grounding line and calving front would be captured, which would help to provide deeper analysis of the criteria for ice shelf stability, either for fractures that are orthogonal to ice flow (perpendicular to the calving front) or in the same direction as ice flow. Hence, potential scenarios of ice behaviour could be fruitfully progressed using a Full Stokes Equation, finer resolution model to achieve the modelled dynamical state of the ice shelf, and further examine the stability criteria.

- Coupled ice sheet-ice-ocean interface parameterisation for the LAGS.

  The results in the third core chapter (Chapter 4; basal melt) demonstrate that the choice of ice-ocean interface parameterisation has significant impact on the spatial pattern of basal melt and refreezing, and that this in turn influences the position of the calving front and ice dynamics. Simplified ocean models perform less well than those using a three-dimensional ocean model that enables a frazil ice precipitation component to be incorporated. Simulations with a coupled ice-ocean model providing mass flux at the ice-ocean interface will be required to explore the effect of a changing ice cavity shape for simulations over longer time frames or using temporal variations in climate forcing. Factors that control ice softness are also relevant since forcing from the ocean due to changes in temperature, tide, or salinity are conveyed into the interior ice sheet through ice streams. Ice streams act as a two-way energy transfer belt, the dynamic shifts of an ice drainage system or coastal region could be explored in more depth with a coupled model.

Stand-alone ice sheet models cannot simulate refreezing well. Refreezing underneath an ice shelf helps in buttressing and advancement of the calving front, therefore an ice-ocean interface parameterisation coupled to a full ocean cavity model would allow better representation of the complex process of basal melt and refreezing of ice, following both vertical and horizontal ocean circulation underneath the ice shelf and the consequences to ice dynamics. A coupled model would be able to simulate refreezing at the calving front, along with the calving laws that are employed in ice sheet models. Incorporating sub-annual timescales of ocean forcings in ice sheet models should also be considered to understand the impact of varying ocean boundaries on ice dynamics.

5.3 Conclusions

The LAGS is an excellent region for modelling studies since it has existed in a relatively stable state for multiple decades. This enables model results to be compared with the observed geometry and dynamics of the glacial system. The aspects of the model that are most sensitive under the influence of present day climate forcing can thus be better understood.

The choice of bathymetry impacts the modelled grounding line position with shallow bathymetries resulting in an advanced grounding line and calving front with inaccuracies in the modelled dynamics and stresses of the LAGS and AIS. In contrast, a bathymetry with a deep sub-ice cavity at the southern grounding line reproduces a grounding line position that is very close to observations and minimises the misfit between modelled and observed ice velocity and ice thickness of the LAGS. The inclusion of synthetic pinning points near the calving front causes an increase in ice elevation upstream of the calving front, which consequently reduces the misfit between observed and calculated ice velocity and calving front position.

By including the pinning points near the calving front of the AIS, the modelled areal extent of passive ice at the Amery ice front is identified as slightly larger than previously understood due to the effect of buttressing provided by the pinning points and coastal geometry, which were neglected in previous studies. There is disagreement between different criteria for ice shelf stability, as to the critical position of the calving front that would cause the AIS to disintegrate. The shear resistance provided by the embayment in which the AIS is located appears to have an influence, in addition to the pinning points. Nevertheless, appraisal of results from approaches taken together suggest that the AIS is stable (i.e. unlikely to undergo rapid further retreat) until it retreats to approximately 85 km upstream of the current calving front.

Basal melt is another factor that can affect the stability of the AIS. Exploring the existing ice-ocean interface parameterisations in PISM reveals that they cannot reproduce the observed regions of refreezing on AIS. Modelled basal mass flux can be improved when data from a three-dimensional ocean model are used as a model input. Basal melt rates at the deep grounding line affect ice thickness, while refreezing significantly changes the calving front profile. The modelled refreezing lends stability to the AIS while the present day ocean model remains valid.

The findings of the research described in this thesis demonstrate model sensitivity bedrock features including those of small-scale, and ice-ocean input data, for modelling ice dynamics. The findings also point to the influence of bedrock features more generally on the likely calving response of the ice shelf under different retreat scenarios. As a result of the research described in this thesis, it is recommended that efforts continue to improve bathymetry datasets, particularly in the difficult-to-observe regions of the deep grounding line and behind the calving front where the ice shelf encounters the ocean. It is also recommended that ocean models are considered as input to studies using PISM, rather than relying on internal parameter selections. Incorporating improved boundary conditions should enable future modelling studies to better predict the response of ice sheet systems to external forcings, and thus improve estimates of future ice mass loss and consequent contributions to sea-level rise.

Bibliography

Adusumilli, S., Fricker, H. A., Medley, B., Padman, L., and Siegfried, M. R. (2020). Interannual variations in meltwater input to the Southern Ocean from Antarctic ice shelves. *Nature Geoscience*, 13(9):616–620.

Adusumilli, S., Fricker, H. A., Siegfried, M. R., Padman, L., Paolo, F. S., and Ligtenberg, S. R. (2018). Variable Basal Melt Rates of Antarctic Peninsula Ice Shelves, 1994–2016. *Geophysical Research Letters*, 45(9):4086–4095.

Albrecht, T., Martin, M., Haseloff, M., Winkelmann, R., and Levermann, A. (2011). Parameterization for subgrid-scale motion of ice-shelf calving fronts. *Cryosphere*, 5(1):35–44.

Alley, K. E., Scambos, T. A., Miller, J. Z., Long, D. G., and MacFerrin, M. (2018). Quantifying vulnerability of Antarctic ice shelves to hydrofracture using microwave scattering properties. *Remote Sensing of Environment*, 210(January):297–306.

Alley, R. B., Anandakrishnan, S., Christianson, K., Horgan, H. J., Muto, A., Parizek, B. R., Pollard, D., and Walker, R. T. (2015). Oceanic Forcing of Ice-Sheet Retreat: West Antarctica and More. *Annual Review of Earth and Planetary Sciences*, 43(1):207–231.

An, M., Wiens, D. A., Zhao, Y., Feng, M., Nyblade, A., Kanao, M., Li, Y., Maggi, A., and Lévêque, J. J. (2015). Temperature, lithosphere-asthenosphere boundary, and heat flux beneath the Antarctic Plate inferred from seismic velocities. *Journal of Geophysical Research: Solid Earth*, 120(12):8720–8742.

Arndt, J. E., Schenke, H. W., Jakobsson, M., Nitsche, F. O., Buys, G., Goleby, B., Rebesco, M., Bohoyo, F., Hong, J., Black, J., Greku, R., Udintsev, G., Barrios, F., Reynoso-Peralta, W., Taisei, M., and Wigley, R. (2013). The international bathymetric chart of the Southern Ocean (IBCSO) version 1.0-A new bathymetric compilation covering circum-Antarctic waters. *Geophysical Research Letters*, 40(12):3111–3117.

Asay-Davis, X. S., Cornford, S. L., Durand, G., Galton-Fenzi, B. K., Gladstone, R. M., Hilmar Gudmundsson, G., Hattermann, T., Holland, D. M., Holland, D., Holland, P. R., Martin, D. F., Mathiot, P., Pattyn, F., and Seroussi, H. (2016). Experimental design for three interrelated marine ice sheet and ocean model intercomparison projects: MISMIP v. 3 (MISMIP +), ISOMIP v. 2 (ISOMIP +) and MISOMIP v. 1 (MISOMIP1). *Geoscientific Model Development*, 9(7):2471–2497.

Aschwanden, A., Aøalgeirsdóttir, G., and Khroulev, C. (2013). Hindcasting to measure ice sheet model sensitivity to initial states. *Cryosphere*, 7(4):1083–1093.

Aschwanden, A., Bueler, E., Khroulev, C., and Blatter, H. (2012). An enthalpy formulation for glaciers and ice sheets. *Journal of Glaciology*, 58(209):441–457.

Aschwanden, A., Fahnestock, M. A., and Truffer, M. (2016). Complex Greenland outlet glacier flow captured. *Nature Communications*, 7(May 2015):1–8.

Bart, P. J., Mullally, D., and Golledge, N. R. (2016). The influence of continental shelf bathymetry on Antarctic Ice Sheet response to climate forcing. *Global and Planetary Change*, 142:87–95.

Bassis, J. N., Coleman, R., Fricker, H. A., and Minster, J. B. (2005). Episodic propagation of a rift on the Amery Ice Shelf, East Antarctica. *Geophysical Research Letters*, 32(6):1–5.

Bassis, J. N., Fricker, H. A., Coleman, R., and Minster, J. B. (2008). An investigation into the forces that drive ice-shelf rift propagation on the Amery ice shelf, East Antarctica. *Journal of Glaciology*, 54(184):17–27.

Bassis, J. N. and Jacobs, S. (2013). Diverse calving patterns linked to glacier geometry. *Nature Geoscience*, 6(10):833–836.

Berger, S., Favier, L., Drews, R., Derwael, J. J., and Pattyn, F. (2016). The control of an uncharted pinning point on the flow of an Antarctic ice shelf. *Journal of Glaciology*, 62(231):37–45.

Bindschadler, R., Vornberger, P., Fleming, A., Fox, A., Mullins, J., Binnie, D., Paulsen, S., Granneman, B., and Gorodetzky, D. (2008). The landsat image mosaic of antarctica. *Remote Sensing of Environment*, 112:4214–4226.

Borstad, C., McGrath, D., and Pope, A. (2017). Fracture propagation and stability of ice shelves governed by ice shelf heterogeneity. *Geophysical Research Letters*, 44(9):4186–4194.

Borstad, C. P., Rignot, E., Mouginot, J., and Schodlok, M. P. (2013). Creep deformation and buttressing capacity of damaged ice shelves: Theory and application to Larsen C ice shelf. *Cryosphere*, 7(6):1931–1947.

Brunt, K. M., Fricker, H. A., Padman, L., Scambos, T. A., and O'Neel, S. (2010). Mapping the grounding zone of the Ross Ice Shelf, Antarctica, using ICESat laser altimetry. *Annals of Glaciology*, 51(55):71–79.

Bueler, E. and Brown, J. (2009). Shallow shelf approximation as a "sliding law" in a thermomechanically coupled ice sheet model. *Journal of Geophysical Research: Solid Earth*, 114(3):1–21.

Bueler, E., Brown, J., and Lingle, C. (2007). Exact solutions to the thermomechanically coupled shallow-ice approximation: Effective tools for verification. *Journal of Glaciology*, 53(182):499–516.

Church, J., Clark, P., Cazenave, A., Gregory, J., Jevrejeva, S., Levermann, A., Merrifield, M., Milne, G., Nerem, R., Nunn, P., Payne, A., Pfeffer, W., Stammer, D., and Alakkat, U. (2013). Climate change 2013: The physical science basis. contribution of working group i to the fifth assessment report of the intergovernmental panel on climate change. *Sea Level Change*, pages 1138–1191.

Colleoni, F., De Santis, L., Siddoway, C. S., Bergamasco, A., Golledge, N. R., Lohmann, G., Passchier, S., and Siegert, M. J. (2018). Spatio-temporal variability of processes across

Antarctic ice-bed-ocean interfaces. *Nature Communications*, 9(1).

Craven, M., Allison, I., Fricker, H. A., and Warner, A. R. (2009a). Properties of a marine ice layer under the Amery Ice Shelf, East Antarctica. *Journal of Glaciology*, 55(192):717–728.

Craven, M., Allison, I., Fricker, H. A., and Warner, A. R. (2009b). Properties of a marine ice layer under the Amery Ice Shelf, East Antarctica. *Journal of Glaciology*, 55(192):717–728.

Damm, V. (2007). A subglacial topographic model of the southern drainage area of the lambert glacier/amery ice shelf system - results of an airborne ice thickness survey south of the prince charles mountains. *Terra Antartica*, 14:85–94.

DeConto, R. M. and Pollard, D. (2016). Contribution of Antarctica to past and future sea-level rise. *Nature*, 531(7596):591–597.

Depoorter, M. A., Bamber, J. L., Griggs, J. A., Lenaerts, J. T., Ligtenberg, S. R., Van Den Broeke, M. R., and Moholdt, G. (2013). Calving fluxes and basal melt rates of Antarctic ice shelves. *Nature*, 502(7469):89–92.

Dinniman, M. S., Asay-Davis, X. S., Galton-Fenzi, B. K., Holland, P. R., Jenkins, A., and Timmermann, R. (2016). Modeling ice shelf/ocean interaction in Antarctica: A review. *Oceanography*, 29(4):144–153.

Doake, C. S. M. (1976). Thermodynamics of the interaction between ice shelves and the sea. *Polar Rec*, 18(112):37–41.

Doake, C. S. M., Corr, H. F. J., Rott, H., Skvarca, P., and Young, N. W. (1998). Breakup and conditions for stability of the northern Larsen Ice Shelf, Antarctica. *Nature*, 391(6669):778–780.

Dupont, T. K. and Alley, R. B. (2005). Assessment of the importance of ice-shelf buttressing to ice-sheet flow. *Geophysical Research Letters*, 32(4):1–4.

Durand, G., Gagliardini, O., Favier, L., Zwinger, T., and Le Meur, E. (2011). Impact of bedrock description on modeling ice sheet dynamics. *Geophysical Research Letters*, 38(20):6–11.

Favier, L., Gagliardini, O., Durand, G., and Zwinger, T. (2012). A three-dimensional full Stokes model of the grounding line dynamics: Effect of a pinning point beneath the ice shelf. *Cryosphere*, 6(1):101–112.

Favier, L., Pattyn, F., Berger, S., and Drews, R. (2016). Dynamic influence of pinning points on marine ice-sheet stability: A numerical study in Dronning Maud Land, East Antarctica. *Cryosphere*, 10(6):2623–2635.

Feldmann, J., Albrecht, T., Khroulev, C., Pattyn, F., and Levermann, A. (2014). Resolution-dependent performance of grounding line motion in a shallow model compared with a full-Stokes model according to the MISMIP3d intercomparison. *Journal of Glaciology*, 60(220):353–360.

Francis, D., Mattingly, K. S., Lhermitte, S., Temimi, M., and Heil, P. (2020). Atmospheric extremes triggered the biggest calving event in more than 50 years at the Amery Ice shelf in September 2019. (August):1–30.

Fretwell, P., Pritchard, H. D., Vaughan, D. G., Bamber, J. L., Barrand, N. E., Bell, R., Bianchi, C., Bingham, R. G., Blankenship, D. D., Casassa, G., Catania, G., Callens, D., Conway, H., Cook, A. J., Corr, H. F., Damaske, D., Damm, V., Ferraccioli, F., Forsberg, R., Fujita, S., Gim, Y., Gogineni, P., Griggs, J. A., Hindmarsh, R. C., Holmlund, P., Holt, J. W., Jacobel, R. W., Jenkins, A., Jokat, W., Jordan, T., King, E. C., Kohler, J., Krabill, W., Riger-Kusk, M., Langley, K. A., Leitchenkov, G., Leuschen, C., Luyendyk, B. P., Matsuoka, K., Mouginot, J., Nitsche, F. O., Nogi, Y., Nost, O. A., Popov, S. V., Rignot, E., Rippin, D. M., Rivera, A., Roberts, J., Ross, N., Siegert, M. J., Smith, A. M., Steinhage, D., Studinger, M., Sun, B., Tinto, B. K., Welch, B. C., Wilson, D., Young, D. A., Xiangbin, C., and Zirizzotti, A. (2013). Bedmap2: Improved ice bed, surface and thickness datasets for Antarctica. *Cryosphere*, 7(1):375–393.

Fricker, H. A., Allison, I., Craven, M., Hyland, G.and Ruddell, A., Young, N., Coleman, R., King, M., Krebs, K., and Popov, S. (2002a). Redefinition of the Amery Ice Shelf, East Antarctica, grounding zone. *Journal of Geophysical Research*, 107(B5):1–9.

Fricker, H. A., Coleman, R., Padman, L., Scambos, T. A., Bohlander, J., and Brunt, K. M. (2009). Mapping the grounding zone of the Amery Ice Shelf, East Antarctica using InSAR, MODIS and ICESat. *Antarctic Science*, 21(5):515–532.

Fricker, H. A., Popov, S., Allison, I., and Young, N. (2001). Distribution of Marine Ice Beneath the Amery Ice Shelf. *Geophysical Research Letters*, 28(11):2241–2244.

Fricker, H. A., Young, N. W., Allison, I., and Coleman, R. (2002b). Iceberg calving from the Amery Ice Shelf, East Antarctica. *Annals of Glaciology*, 34(October 2017):241–246.

Fricker, H. A., Young, N. W., Coleman, R., Bassis, J. N., and Minster, J. B. (2005). Multi-year monitoring of rift propagation on the Amery Ice Shelf, East Antarctica. *Geophysical Research Letters*, 32(2):1–5.

Fürst, J. J., Durand, G., Gillet-Chaulet, F., Merino, N., Tavard, L., Mouginot, J., Gourmelen, N., and Gagliardini, O. (2015). Assimilation of Antarctic velocity observations provides evidence for uncharted pinning points. *Cryosphere*, 9(4):1427–1443.

Fürst, J. J., Durand, G., Gillet-Chaulet, F., Tavard, L., Rankl, M., Braun, M., and Gagliardini, O. (2016). The safety band of Antarctic ice shelves. *Nature Climate Change*, 6(5):479–482.

Gagliardini, O., Zwinger, T., Gillet-Chaulet, F., Durand, G., Favier, L., de Fleurian, B., Greve, R., Malinen, M., Martín, C., Råback, P., Ruokolainen, J., Sacchettini, M., Schäfer, M., Seddik, H., and Thies, J. (2013). Capabilities and performance of Elmer/Ice, a new generation ice-sheet model. *Geoscientific Model Development Discussions*, 6(1):1689–1741.

Galton-Fenzi, B. K., Hunter, J. R., Coleman, R., Marsland, S. J., and Warner, R. C. (2012). Modeling the basal melting and marine ice accretion of the Amery Ice Shelf. *Journal of Geophysical Research: Oceans*, 117(9):1–19.

Galton-Fenzi, B. K., Maraldi, C., Coleman, R., and Hunter, J. (2008). The cavity under the Amery Ice Shelf, East Antarctica. *Journal of Glaciology*, 54(188):881–887.

Gardner, A. S., Moholdt, G., Scambos, T., Fahnstock, M., Ligtenberg, S., Van Den Broeke, M., and Nilsson, J. (2018). Increased West Antarctic and unchanged East Antarctic ice discharge over the last 7 years. *Cryosphere*, 12(2):521–547.

Gasson, E., DeConto, R., and Pollard, D. (2015). Antarctic bedrock topography uncertainty and ice sheet stability. *Geophysical Research Letters*, 42(13):5372–5377.

Gladstone, R. M., Lee, V., Rougier, J., Payne, A. J., Hellmer, H., Le Brocq, A., Shepherd, A., Edwards, T. L., Gregory, J., and Cornford, S. L. (2012). Calibrated prediction of Pine Island Glacier retreat during the 21st and 22nd centuries with a coupled flowline model. *Earth and Planetary Science Letters*, 333-334:191–199.

Golledge, N. R., Fogwill, C. J., Mackintosh, A. N., and Buckley, K. M. (2012). Dynamics of the last glacial maximum Antarctic ice-sheet and its response to ocean forcing. *Proceedings of the National Academy of Sciences of the United States of America*, 109(40):16052–6.

Golledge, N. R., Kowalewski, D. E., Naish, T. R., Levy, R. H., Fogwill, C. J., and Gasson, E. G. (2015). The multi-millennial Antarctic commitment to future sea-level rise. *Nature*.

Gong, Y., Cornford, S. L., and Payne, A. J. (2014). Modelling the response of the Lambert Glacier-Amery Ice Shelf system, East Antarctica, to uncertain climate forcing over the 21st and 22nd centuries. *Cryosphere*, 8(3):1057–1068.

Gudmundsson, G. H. (2013). Ice-shelf buttressing and the stability of marine ice sheets. *Cryosphere*, 7(2):647–655.

Hellmer, H. H. (2004). Impact of Antarctic ice shelf basal melting on sea ice and deep ocean properties. *Geophysical Research Letters*, 31(10):1–4.

Hindmarsh, R. C. (2006). The role of membrane-like stresses in determining the stability and sensitivity of the Antarctic ice sheets: Back pressure and grounding line motion. *Philosophical Transactions of the Royal Society A: Mathematical, Physical and Engineering Sciences*, 364(1844):1733–1767.

Hindmarsh, R. C. A. (2004). A numerical comparison of approximations to the Stokes equations used in ice sheet and glacier modeling. *Journal of Geophysical Research: Earth Surface*, 109(F1):1–15.

Hoffman, M. and Price, S. (2014). Journal of Geophysical Research : Earth Surface Feedbacks between coupled subglacial hydrology and glacier dynamics. pages 1–23.

Holland, D. M. and Jenkins, A. (1999). Modeling Thermodynamic Ice–Ocean Interactions at the Base of an Ice Shelf. *Journal ofPhysical Oceanography.*, 29(8)(1987):1787–1800.

Holland, P. R., Corr, H. F., Vaughan, D. G., Jenkins, A., and Skvarca, P. (2009). Marine ice in Larsen Ice Shelf. *Geophysical Research Letters*, 36(11):1–6.

Holland, P. R., Jenkins, A., and Holland, D. M. (2008). The response of Ice shelf basal melting to variations in ocean temperature. *Journal of Climate*, 21(11):2558–2572.

Jacobs, S. S., Hellmer, H., S. M. Doake, C., Jenkins, A., and M. Frolich, R. (1992). Melting of ice shelves and mass balance of Antarctica. *Journal of Glaciology*, 38:375–387.

Jansen, D., Luckman, A., Kulessa, B., Holland, P. R., and King, E. C. (2013). Marine ice formation in a suture zone on the Larsen C Ice Shelf and its influence on ice shelf dynamics. *Journal of Geophysical Research: Earth Surface*, 118(3):1628–1640.

Jansen, D., Luckman, A. J., Cook, A., Bevan, S., Kulessa, B., Hubbard, B., and Holland, P. R. (2015). Brief Communication: Newly developing rift in Larsen C Ice Shelf presents significant risk to stability. *Cryosphere*, 9(3):1223–1227.

Jenkins, A., Dutrieux, P., Jacobs, S. S., McPhail, S. D., Perrett, J. R., Webb, A. T., and White, D. (2010). Observations beneath Pine Island Glacier in West-Antarctica and implications for its retreat. *Nature Geoscience*, 3(7):468–472.

Jenkins, A. and Holland, D. (2007). Melting of floating ice and sea level rise. *Geophysical Research Letters*, 34(16):1–5.

Joughin, I. and MacAyeal, D. R. (2005). Calving of large tabular icebergs from ice shelf rift systems. *Geophysical Research Letters*, 32(2):1–4.

King, M. A., Bingham, R. J., Moore, P., Whitehouse, P. L., Bentley, M. J., and Milne, G. A. (2012). Lower satellite-gravimetry estimates of Antarctic sea-level contribution. *Nature*, 491(7425):586–589.

King, M. A., Coleman, R., Freemantle, A. J., Fricker, H. A., Hurd, R. S., Legrésy, B., Padman, L., and Warner, R. (2009). A 4-decade record of elevation change of the Amery Ice Shelf, East Antarctica. *Journal of Geophysical Research: Earth Surface*, 114(1).

King, M. A., Coleman, R., Morgan, P. J., and Hurd, R. S. (2007). Velocity change of the Amery Ice Shelf, East Antarctica, during the period 1968-1999. *Journal of Geophysical Research: Earth Surface*, 112(1):1–11.

Kingslake, J., Ely, J. C., Das, I., and Bell, R. E. (2017). Widespread movement of meltwater onto and across Antarctic ice shelves. *Nature*, 544(7650):349–352.

Kulessa, B., Jansen, D., Luckman, A. J., King, E. C., and Sammonds, P. R. (2014). Marine ice regulates the future stability of a large Antarctic ice shelf. *Nature Communications*, 5(April):1–7.

Lai, C. Y., Kingslake, J., Wearing, M. G., Chen, P. H. C., Gentine, P., Li, H., Spergel, J. J., and van Wessem, J. M. (2020). Vulnerability of Antarctica's ice shelves to meltwater-driven fracture. *Nature*, 584(7822):574–578.

Langley, E. S., Leeson, A. A., Stokes, C. R., and Jamieson, S. S. (2016). Seasonal evolution of supraglacial lakes on an East Antarctic outlet glacier. *Geophysical Research Letters*, 43(16):8563–8571.

Larour, E., Seroussi, H., Morlighem, M., and Rignot, E. (2012). Continental scale, high order, high spatial resolution, ice sheet modeling using the Ice Sheet System Model (ISSM). *Journal of Geophysical Research: Earth Surface*, 117(1).

Leong, W. J. and Horgan, H. J. (2020). DeepBedMap: Using a deep neural network to better resolve the bed topography of Antarctica. *The Cryosphere Discussions*, 1(April):1–27.

Levermann, A., Albrecht, T., Winkelmann, R., Martin, M., and Haseloff, M. (2010). Universal dynamic calving law implies potential for abrupt ice-shelf retreat. 12:2536.

Levermann, A., Albrecht, T., Winkelmann, R., Martin, M. A., Haseloff, M., and Joughin, I. (2012). Kinematic first-order calving law implies potential for abrupt ice-shelf retreat.

Cryosphere, 6(2):273–286.

Lewis, E. L. and Perkin, R. G. (1986). Ice pumps and their rates. *Journal of Geophysical Research*, 91(C10):11756.

Liu, Y., Moore, J. C., Cheng, X., Gladstone, R. M., Bassis, J. N., Liu, H., Wen, J., and Hui, F. (2015). Ocean-driven thinning enhances iceberg calving and retreat of Antarctic ice shelves. *Proceedings of the National Academy of Sciences*, 112(11):3263–3268.

Lliboutry, L. A. and Duval, P. (1985). Various isotropic and anisotropic ices found in glaciers and polar ice caps and their corresponding rheologies. *Ann Geophys V3, N2, March–April 1985, P207–224*.

Martin, M. A., Winkelmann, R., Haseloff, M., Albrecht, T., Bueler, E., Khroulev, C., and Levermann, A. (2011). The Potsdam Parallel Ice Sheet Model (PISM-PIK) - Part 2: Dynamic equilibrium simulation of the Antarctic ice sheet. *Cryosphere*, 5(3):727–740.

Matsuoka, K., Hindmarsh, R. C., Moholdt, G., Bentley, M. J., Pritchard, H. D., Brown, J., Conway, H., Drews, R., Durand, G., Goldberg, D., Hattermann, T., Kingslake, J., Lenaerts, J. T., Martín, C., Mulvaney, R., Nicholls, K. W., Pattyn, F., Ross, N., Scambos, T., and Whitehouse, P. L. (2015). Antarctic ice rises and rumples: Their properties and significance for ice-sheet dynamics and evolution. *Earth-Science Reviews*, 150:724–745.

McGrath, D., Steffen, K., Holland, P. R., Scambos, T., Rajaram, H., Abdalati, W., and Rignot, E. (2014). The structure and effect of suture zones in the Larsen C Ice Shelf, Antarctica. *Journal of Geophysical Research: Earth Surface*, 119(3):588–602.

Morlighem, M., Rignot, E., and Binder, T. (2019). Deep glacial troughs and stabilizing ridges unveiled beneath the margins of the Antarctic ice sheet. *Nat. Geosci.*

Mouginot, J., Scheuchl, B., and Rignot, E. (2017). MEaSUREs Antarctic Boundaries for IPY 2007-2009 from Satellite Radar, Version 2. [Indicate subset used]. Boulder, Colorado USA. NASA National Snow and Ice Data Center Distributed Active Archive Center. doi: http://dx.doi.org/10.5067/AXE4121732AD. [Date Accessed]. .

Nitsche, F. O., Porter, D., Williams, G., Cougnon, E. A., Fraser, A. D., Correia, R., and Guerrero, R. (2017). Bathymetric control of warm ocean water access along the East Antarctic Margin. *Geophysical Research Letters*, 44(17):8936–8944.

Paolo, F. S., Fricker, H. A., and Padman, L. (2015). Volume loss from Antarctic ice shelves is accelerating. *Science*, 348(6232):327–331.

Patauri, R., Meyer, L., and Core-Writing-Team (2014). IPCC 2014: Climate Change 2014: Synthesis Report. *IPCC, Geneva, Switzerland*.

Paterson, W. S. B. and Budd, W. F. (1982). Flow parameters for ice sheet modelling. *Cold. Reg. Sci. Technol*, 6:175–177.

Pattyn, F. (2018). The paradigm shift in Antarctic ice sheet modelling. *Nature Communications*, 9(1):10–12.

Phillips, H. A. (1998). Surface meltstreams on the Amery Ice Shelf, East Antarctica. *Annals of Glaciology*, 27:177–181.

Pittard, M. L. (2016). The dynamics of the Lambert-Amery glacial system and its response to climatic variations. *PhD thesis, University of Tasmania.*

Pittard, M. L., Galton-Fenzi, B. K., Watson, C. S., and Roberts, J. L. (2017). Future sea level change from Antarctica's Lambert-Amery glacial system. *Geophysical Research Letters*, 44(14):7347–7355.

Pittard, M. L., Roberts, J. L., Galton-Fenzi, B. K., and Watson, C. S. (2016). Sensitivity of the Lambert-Amery glacial system to geothermal heat flux. *Annals of Glaciology*, 57(73):56–68.

Pollard, D., DeConto, R. M., and Alley, R. B. (2015). Potential Antarctic Ice Sheet retreat driven by hydrofracturing and ice cliff failure. *Earth and Planetary Science Letters*, 412:112–121.

Pritchard, H., Ligtenberg, S., Fricker, H., Vaughan, D., Van den Broeke, M., and Padman, L. (2012). Antarctic ice-sheet loss driven by basal melting of ice shelves. *Nature*, 484(7395):502–505.

Pritchard, H. D., Arthern, R. J., Vaughan, D. G., and Edwards, L. A. (2009). Extensive dynamic thinning on the margins of the Greenland and Antarctic ice sheets. *Nature*, 461(7266):971–975.

Reese, R., Albrecht, T., Mengel, M., Asay-Davis, X., and Winkelmann, R. (2018a). Antarctic sub-shelf melt rates via PICO. *Cryosphere*, 12(6):1969–1985.

Reese, R., Gudmundsson, G. H., Levermann, A., and Winkelmann, R. (2018b). The far reach of ice-shelf thinning in Antarctica. *Nature Climate Change*, 8(1):53–57.

Richter, O., Gwyther, D., Galton-Fenzi, B., and Naughten, K. (2020). The Whole Antarctic Ocean Model (WAOM v1.0): Development and Evaluation. *Geoscientific Model Development Discussions*, (June):1–40.

Rignot, E., Casassa, G., Gogineni, P., Krabill, W., Rivera, A., and Thomas, R. (2004). Accelerated ice discharge from the Antarctic Peninsula following the collapse of Larsen B ice shelf. *Geophysical Research Letters*, 31(18):2–5.

Rignot, E., Jacobs, S., Mouginot, J., and Scheuchl, B. (2013). Ice-shelf melting around antarctica. *Science*, 341(6143):266–270.

Rignot, E. and Jacobs, S. S. (2002). Rapid bottom melting widespread near Antarctic ice sheet grounding lines. *Science*, 296(5575):2020–2023.

Rignot, E., Mouginot, J., and Scheuchl, B. (2011). Ice flow of the Antarctic ice sheet. *Science*, 333(6048):1427–1430.

Santner, T., Williams, B., and Notz, W. (2003). The design and analysis of computer experimentst. *Springer, New York.*

Scambos, T., Hulbe, C., and Fahnestock, M. (2003). Climate-induced ice shelf disintegration in the antarctic peninsula. *Antarctic Research Series*, 79:79–92.

Scambos, T. A., Bohlander, J. A., Shuman, C. A., and Skvarca, P. (2004). Glacier acceleration and thinning after ice shelf collapse in the Larsen B embayment, Antarctica. *Geophysical Research Letters*, 31(18):3–7.

Schaffer, J., Timmermann, R., Erik Arndt, J., Savstrup Kristensen, S., Mayer, C., Morlighem, M., and Steinhage, D. (2016). A global, high-resolution data set of ice sheet topography, cavity geometry, and ocean bathymetry. *Earth System Science Data*, 8(2):543–557.

Schoof, C. (2007). Ice sheet grounding line dynamics: Steady states, stability, and hysteresis. *Journal of Geophysical Research: Earth Surface*, 112(3):1–19.

Seguinot, J., Khroulev, C., Rogozhina, I., Stroeven, A. P., and Zhang, Q. (2014). The effect of climate forcing on numerical simulations of the cordilleran ice sheet at the last glacial maximum. *Cryosphere*, 8(3):1087–1103.

Silvano, A., Rintoul, S., and Herraiz-Borreguero, L. (2016). Ocean-ice shelf interaction in East Antarctica. *Oceanography*, 29(4):130–143.

Sun, S., Cornford, S. L., Liu, Y., and Moore, J. C. (2014). Dynamic response of Antarctic ice shelves to bedrock uncertainty. *Cryosphere*, 8(4):1561–1576.

Thomas, R. H. and Bentley, C. R. (1978). A model for Holocene retreat of the West Antarctic Ice Sheet. *Quaternary Research*, 10(2):150–170.

Timmermann, R., Le Brocq, A., Deen, T., Domack, E., Dutrieux, P., Galton-Fenzi, B., Hellmer, H., Humbert, A., Jansen, D., Jenkins, A., Lambrecht, A., Makinson, K., Niederjasper, F., Nitsche, F., Nøst, O. A., Smedsrud, L. H., and Smith, W. H. F. (2010). A consistent dataset of Antarctic ice sheet topography, cavity geometry, and global bathymetry. *Earth System Science Data Discussions*, 3(2):231–257.

Treverrow, A., Warner, R. C., Budd, W. F., and Craven, M. (2010). Meteoric and marine ice crystal orientation fabrics from the amery ice shelf, East Antarctica. *Journal of Glaciology*, 56(199):877–890.

Van Wessem, J. M., Reijmer, C. H., Lenaerts, J. T., Van De Berg, W. J., Van Den Broeke, M. R., and Van Meijgaard, E. (2014). Updated cloud physics in a regional atmospheric climate model improves the modelled surface energy balance of Antarctica. *Cryosphere*, 8(1):125–135.

Walker, C. C., Bassis, J. N., Fricker, H. A., and Czerwinski, R. J. (2013). Structural and environmental controls on Antarctic ice shelf rift propagation inferred from satellite monitoring. *Journal of Geophysical Research: Earth Surface*, 118(4):2354–2364.

Walker, C. C., Bassis, J. N., Fricker, H. A., and Czerwinski, R. J. (2015). Observations of interannual and spatial variability in rift propagation in the Amery Ice Shelf, Antarctica, 2002-14. *Journal of Glaciology*, 61(226):243–252.

Wearing, M. G., Hindmarsh, R. C., and Worster, M. G. (2015). Assessment of ice flow dynamics in the zone close to the calving front of Antarctic ice shelves. *Journal of Glaciology*, 61(230):1194–1206.

Weatherall, P., Marks, K. M., Jakobsson, M., Schmitt, T., Tani, S., Arndt, J. E., Rovere, M., Chayes, D., Ferrini, V., and Wigley, R. (2015). A new digital bathymetric model of the world's oceans. *Earth and Space Science*.

Weertman, J. (1974). Stability of the Junction of an Ice Sheet and an Ice Shelf. *Journal of*

Glaciology, 13(67):3–11.

Wen, J., Wang, Y., Wang, W., Jezek, K., Liu, H., and Allison, I. (2010). Basal melting and freezing under the Amery Ice Shelf, East Antarctica. *Journal of Glaciology*, 56(195):81–90.

White, D. A., Fink, D., and Gore, D. B. (2011). Cosmogenic nuclide evidence for enhanced sensitivity of an East Antarctic ice stream to change during the last deglaciation. *Geology*, 39(1):23–26.

Williams, M. J. M., Grosfeld, K., Warner, R. C., and Gerdes, R. (2001). the Amery Ice Shelf , Antarctica Determann. *October*, 106.

Winkelmann, R., Martin, M. A., Haseloff, M., Albrecht, T., Bueler, E., Khroulev, C., and Levermann, A. (2011). The Potsdam Parallel Ice Sheet Model (PISM-PIK) - Part 1: Model description. *Cryosphere*, 5(3):715–726.

Yu, J., Liu, H., Jezek, K. C., Warner, R. C., and Wen, J. (2010). Analysis of velocity field, mass balance, and basal melt of the Lambert glacier-amery ice shelf system by incorporating Radarsat SAR interferometry and ICESat laser altimetry measurements. *Journal of Geophysical Research: Solid Earth*, 115(11):1–16.

Zhao, C., Cheng, X., Liu, Y., Hui, F., Kang, J., Wang, X., Wang, F., and Cheng, C. (2013). The slow-growing tooth of the Amery Ice Shelf from 2004 to 2012. *Journal of Glaciology*, 59(215):592–596.

Zwally, H., Jay, M. B., Giovinetto, M. A., Beckley, and Jack, L. S. (2012). Antarctic and Greenland Drainage Systems. *GSFC Cryospheric Sciences Laboratory*.

Zwally, H. J. and Giovinetto, M. B. (2011). Overview and Assessment of Antarctic Ice-Sheet Mass Balance Estimates: 1992-2009. *Surveys in Geophysics*, 32(4-5):351–376.